



FALL / WINTER 2019  
VOLUME 11, NUMBER 2

Print ISSN: 2152-4157  
Online ISSN: 2152-4165

WWW.IJERI.ORG

# International Journal of Engineering Research & Innovation

**Editor-in-Chief: Mark Rajai, Ph.D.**  
**California State University Northridge**



Published by the  
**International Association of Journals & Conferences**



[www.ijeri.org](http://www.ijeri.org)

Print ISSN: 2152-4157  
Online ISSN: 2152-4165



[www.iajc.org](http://www.iajc.org)

# INTERNATIONAL JOURNAL OF ENGINEERING RESEARCH AND INNOVATION

## **ABOUT IJERI:**

- IJERI is the second official journal of the International Association of Journals and Conferences (IAJC).
- IJERI is a high-quality, independent journal steered by a distinguished board of directors and supported by an international review board representing many well-known universities, colleges, and corporations in the U.S. and abroad.
- IJERI has an impact factor of **1.58**, placing it among an elite group of most-cited engineering journals worldwide.

## **OTHER IAJC JOURNALS:**

- The International Journal of Modern Engineering (IJME)  
For more information visit [www.ijme.us](http://www.ijme.us)
- The Technology Interface International Journal (TIIJ)  
For more information visit [www.tiij.org](http://www.tiij.org)

## **IJERI SUBMISSIONS:**

- Manuscripts should be sent electronically to the manuscript editor, Dr. Philip Weinsier, at [philipw@bgsu.edu](mailto:philipw@bgsu.edu).

For submission guidelines visit  
[www.ijeri.org/submissions](http://www.ijeri.org/submissions)

## **TO JOIN THE REVIEW BOARD:**

- Contact the chair of the International Review Board, Dr. Philip Weinsier, at [philipw@bgsu.edu](mailto:philipw@bgsu.edu).

For more information visit  
[www.ijeri.org/editorial](http://www.ijeri.org/editorial)

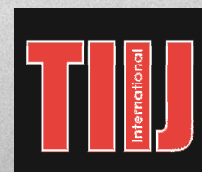
## **INDEXING ORGANIZATIONS:**

- IJERI is indexed by numerous agencies. For a complete listing, please visit us at [www.ijeri.org](http://www.ijeri.org).

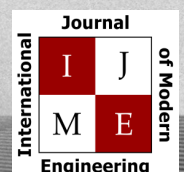
## **Contact us:**

**Mark Rajai, Ph.D.**

Editor-in-Chief  
California State University-Northridge  
College of Engineering and Computer Science  
Room: JD 4510  
Northridge, CA 91330  
Office: (818) 677-5003  
Email: [mrajai@csun.edu](mailto:mrajai@csun.edu)



[www.tiij.org](http://www.tiij.org)



[www.ijme.us](http://www.ijme.us)

---

# INTERNATIONAL JOURNAL OF ENGINEERING RESEARCH AND INNOVATION

The INTERNATIONAL JOURNAL OF ENGINEERING RESEARCH AND INNOVATION (IJERI) is an independent and not-for-profit publication, which aims to provide the engineering community with a resource and forum for scholarly expression and reflection.

IJERI is published twice annually (fall and spring issues) and includes peer-reviewed research articles, editorials, and commentary that contribute to our understanding of the issues, problems, and research associated with engineering and related fields. The journal encourages the submission of manuscripts from private, public, and academic sectors. The views expressed are those of the authors and do not necessarily reflect the opinions of the IJERI editors.

## EDITORIAL OFFICE:

Mark Rajai, Ph.D.  
Editor-in-Chief  
Office: (818) 677-2167  
Email: [ijmeeditor@iajc.org](mailto:ijmeeditor@iajc.org)  
Dept. of Manufacturing Systems  
Engineering & Management  
California State University-  
Northridge  
18111 Nordhoff Street  
Northridge, CA 91330-8332

## THE INTERNATIONAL JOURNAL OF ENGINEERING RESEARCH AND INNOVATION EDITORS

### *Editor-in-Chief:*

**Mark Rajai**

California State University-Northridge

### *Associate Editors:*

**Paul Wilder**

Vincennes University

**Li Tan**

Purdue University Northwest

### *Production Editor:*

**Philip Weinsier**

Bowling Green State University-Firelands

### *Subscription Editor:*

**Morteza Sadat-Hossieny**

Northern Kentucky University

### *Web Administrator:*

**Saeed Namyar**

Advanced Information Systems

### *Manuscript Editor:*

**Philip Weinsier**

Bowling Green State University-Firelands

### *Copy Editors:*

**Li Tan**

Purdue University Northwest

**Ahmad Sarfaraz**

California State University-Northridge

### *Technical Editors:*

**Marilyn Dyrud**

Oregon Institute of Technology

### *Publisher:*

**Bowling Green State University Firelands**

---

# TABLE OF CONTENTS

<i>Editor's Note: IAJC / ATMAE Joint 2020 Conference</i> .....	3
Philip Weinsier, IJERI Manuscript Editor	
<i>A Low-Cost, High-Resolution Fabrication Method for a Microfluidic Device</i> .....	5
Ran Zhou, Purdue University Northwest; Mark Parra, Purdue University Northwest; Athira Nair Surendran, Purdue University Northwest	
<i>Low-Cost Rapid Prototyping of Personalized 3D-Printed Models of Kidney and Artery Anatomy: A Cost and Time Effective Approach</i> .....	12
Ginni Singh, University of Toledo; Matthew Franchetti, University of Toledo	
<i>Computational Analysis of Asymmetrically Applied Hot and Cold Stimuli</i> .....	18
Ahmad Manasrah, Al-Zaytoonah University; Mehdi Hojatmadani, University of South Florida; Rasim Guldiken, University of South Florida; Kyle Reed, University of South Florida	
<i>Correlating Field to Laboratory Compaction for Roller-Compacted Concrete</i> .....	28
Tamer M. Breakah, Ball State University; Mohamed Nagib Abou-Zeid, The American University in Cairo; Mohamed El-Saied, The American University in Cairo; Kamel Elamrousy, The American University in Cairo; Ahmed Hamed, The American University in Cairo; Elmohanad Elsayad, The American University in Cairo; Fadi Abdallah, The American University in Cairo	
<i>An Automated Hydraulic Position Control System: Structure and Performance Analysis</i> .....	36
Yuqiu You, Ohio University; Jesus Pagan, Ohio University	
<i>Analysis of Dust Emission and Life Impact Assessment of Frame-Shear Wall Structure</i> .....	42
Yadong Bian, Zhongyuan University of Technology, China; Yanru Dai, Zhongyuan University of Technology, China; Li, Zhongyuan University of Technology, China; Zhicheng Gao, University of Akron; Jiliang Li, Purdue University Northwest	
<i>A Robot for Weld Quality Inspection</i> .....	50
Vu Duong, Duy Tan University, Vietnam; Ashfaq Ahmed, Purdue University Northwest; Dang Ngoc Sy, Duy Tan University, Vietnam	
<i>Instructions for Authors: Manuscript Submission Guidelines and Requirements</i> .....	56

# IAJC / ATMAE JOINT 2020 CONFERENCE

**ATMAE and IAJC join forces this year to offer their first-ever joint conference. Join us for this momentous event.**

**Louisville, KY  
October 7-9, 2020**



## **CALL FOR CONFERENCE PROPOSALS**

Conference Proposal Submission Deadlines:

- |                                                 |                   |
|-------------------------------------------------|-------------------|
| ● Abstract Proposal Submission Open             | February 3, 2020  |
| ● Abstract Proposal Submission Closed           | March 16, 2020    |
| ● Presenters Informed of Proposal Decision      | April 27, 2020    |
| ● Invited Conference Paper Submission Open      | May 18, 2020      |
| ● Invited Conference Paper Submission Closed    | July 27, 2020     |
| ● Authors Informed of Conference Paper Decision | September 1, 2020 |
| ● Final Conference Paper Due                    | October 12, 2020  |

The Association of Technology, Management and Applied Engineering (ATMAE) and the International Association of Journals and Conferences (IAJC) invite the submission of proposals for their first-ever joint conference. All abstract proposals must be submitted using Catalyst, ATMAE's online abstract submission and peer review system.

Have questions or need help? Contact

ATMAE office [919.635.8335 or [admin@atmae.org](mailto:admin@atmae.org) ]  
IAJC [email Philip Weinsier at [philipw@bgsu.edu](mailto:philipw@bgsu.edu) ]

Get ready to submit your proposals, starting February 3<sup>rd</sup>. Submission guidelines and instructions will be available on both the IAJC and ATMAE websites soon.

## Editorial Review Board Members

Mohammed Abdallah	State University of New York (NY)	Huyu Qu	Broadcom Corporation
Paul Akangah	North Carolina A&T State University (NC)	Desire Rasolomampionona	Warsaw University of Tech (POLAND)
Nasser Alaraje	Michigan Tech (MI)	Michael Reynolds	University of West Florida (FL)
Ali Alavizadeh	Purdue University Northwest (IN)	Nina Robson	California State University-Fullerton (CA)
Lawal Anka	Zamfara AC Development (NIGERIA)	Marla Rogers	Fastboot Mobile, LLC
Jahangir Ansari	Virginia State University (VA)	Dale Rowe	Brigham Young University (UT)
Kevin Berisso	Ohio University (OH)	Karen Ruggles	DeSales University (PA)
Pankaj Bhambri	Guru Nanak Dev Engineering (INDIA)	Anca Sala	Baker College (MI)
Michelle Brodke	Bowling Green State University (OH)	Alex Sergeev	Michigan Technological University (MI)
Shaobiao Cai	Penn State University (PA)	Mehdi Shabaninejad	Zagros Oil and Gas Company (IRAN)
Rajab Challoo	Texas A&M University Kingsville (TX)	Hiral Shah	St. Cloud State University (MN)
Isaac Chang	Illinois State University (IL)	Mojtaba Shivaie	Shahrood University of Technology (IRAN)
Shu-Hui (Susan) Chang	Iowa State University (IA)	Musibau Shofoluwe	North Carolina A&T State University (NC)
Rigoberto Chinchilla	Eastern Illinois University (IL)	Amit Solanki	Government Engineering College (INDIA)
Phil Cochrane	Indiana State University (IN)	Jiahui Song	Wentworth Institute of Technology (MA)
Curtis Cohenour	Ohio University (OH)	Carl Spezia	Southern Illinois University (IL)
Emily Crawford	Claflin University (SC)	Michelle Surerus	Ohio University (OH)
Dongyang (Sunny)Deng	North Carolina A&T State University (NC)	Harold Terano	Camarines Sur Polytechnic (PHILIPPINES)
Z.T. Deng	Alabama A&M University (AL)	Sanjay Tewari	Missouri University of Science & Techn (MO)
Sagar Deshpande	Ferris State University (MI)	Vassilios Tzouanas	University of Houston Downtown (TX)
David Domermuth	Appalachian State University (NC)	Abraham Walton	University of South Florida Polytechnic (FL)
Marilyn Dyrud	Oregon Institute of Technology (OR)	Haoyu Wang	Central Connecticut State University (CT)
Mehran Elahi	Elizabeth City State University (NC)	Jyhwen Wang	Texas A&M University (TX)
Ahmed Elsayy	Tennessee Technological University (TN)	Liangmo Wang	Nanjing University of Science/Tech (CHINA)
Cindy English	Millersville University (PA)	Boonsap Witchayangkoon	Thammasat University (THAILAND)
Ignatius Fomunung	University of Tennessee Chattanooga (TN)	Shuju Wu	Central Connecticut State University (CT)
Ahmed Gawad	Zagazig University EGYPT)	Baijian "Justin" Yang	Purdue University (IN)
Kevin Hall	Western Illinois University (IL)	Eunice Yang	University of Pittsburgh Johnstown (PA)
Mohsen Hamidi	Utah Valley University (UT)	Xiaoli (Lucy) Yang	Purdue University Northwest (IN)
Mamoon Hammad	Abu Dhabi University (UAE)	Hao Yi	Chongqing University (CHINA)
Gene Harding	Purdue Polytechnic (IN)	Faruk Yildiz	Sam Houston State University (TX)
Bernd Haupt	Penn State University (PA)	Yuqiu You	Ohio University (OH)
Youcef Himri	Safety Engineer in Sonelgaz (ALGERIA)	Pao-Chiang Yuan	Jackson State University (MS)
Delowar Hossain	City University of New York (NY)	Junwen Zhu	Missouri Western State University (MO)
Xiaobing Hou	Central Connecticut State University (CT)		
Shelton Houston	University of Louisiana Lafayette (LA)		
Ying Huang	North Dakota State University (ND)		
Charles Hunt	Norfolk State University (VA)		
Dave Hunter	Western Illinois University (IL)		
Christian Bock-Hyeng	North Carolina A&T University (NC)		
Pete Hylton	Indiana University Purdue (IN)		
John Irwin	Michigan Tech (MI)		
Toqeer Israr	Eastern Illinois University (IL)		
Sudershan Jetley	Bowling Green State University (OH)		
Rex Kanu	Purdue Polytechnic (IN)		
Reza Karim	North Dakota State University (ND)		
Manish Kewalramani	Abu Dhabi University (UAE)		
Tae-Hoon Kim	Purdue University Northwest (IN)		
Chris Kluse	Bowling Green State University (OH)		
Doug Koch	Southeast Missouri State University (MO)		
Resmi Krishnankuttyrema	Bowling Green State University (OH)		
Zaki Kuruppallil	Ohio University (OH)		
Shiyoung Lee	Penn State University Berks (PA)		
Soo-Yen (Samson) Lee	Central Michigan University (MI)		
Chao Li	Florida A&M University (FL)		
Dale Litwhiler	Penn State University (PA)		
Mani Manivannan	ARUP Corporation		
G.H. Massiha	University of Louisiana (LA)		
Thomas McDonald	University of Southern Indiana (IN)		
David Melton	Eastern Illinois University (IL)		
Shokoufeh Mirzaei	Cal State Poly Pomona (CA)		
Sam Mryyan	Excelsior College (NY)		
Jessica Murphy	Jackson State University (MS)		
Rungun Nathan	Penn State Berks (PA)		
Arun Nambiar	California State University Fresno (CA)		
Aurenice Oliveira	Michigan Tech (MI)		
Troy Ollison	University of Central Missouri (MO)		
Reynaldo Pablo	Purdue Fort Wayne (IN)		
Basile Panoutsopoulos	Community College of Rhode Island (RI)		
Shahera Patel	Sardar Patel University (INDIA)		
Thongchai Phairoh	Virginia State University (VA)		

# A LOW-COST, HIGH-RESOLUTION FABRICATION METHOD FOR A MICROFLUIDIC DEVICE

Ran Zhou, Purdue University Northwest; Mark Parra, Purdue University Northwest; Athira Nair Surendran, Purdue University Northwest

## Abstract

Microfluidics enables a diverse range of micrometer-sized object manipulations and has played an increasingly important role in applications that involve single-cell biology and the detection and diagnosis of diseases. Currently, expensive clean-room photolithography methods are used to create superior-feature high-resolution microfluidic master molds. However, the fabrication cost of microfluidic devices can be reduced from hundreds of thousands of dollars to mere thousands with resolutions in the tens to hundreds of micrometers by using simple tools and materials through soft-lithography techniques. This current system is composed of a thermal laminator, ultraviolet (UV) light-emitting diode (LED) light source, vacuum pump, oven, and hot plate. Other basic materials that were used include photoresist dry film, copper plate, and polydimethylsiloxane (PDMS) to create the final product. Using a transparency mask, the photoresist dry film was exposed to the UV-LED light, where the distinct micrometer-size pattern was bonded to a copper plate. Then, utilizing a sodium carbonate solution, the un-exposed dry film was removed. Lastly, PDMS was used to create the final microfluidic channel master mold. By using different designs, a variety of microstructures can be created to test the system's fabrication resolution. The advantages of the system include low cost, ease of operation, and short processing time, which allows the creation of microfluidic master molds at high resolutions very quickly and easily without the use of a cleanroom or specially trained personnel.

## Introduction

Microfluidics has received much attention in recent years, due to its wide application in biology, chemistry, and biomedical engineering. Microfluidics allows researchers to manipulate and control fluids in microscale in micron-size channels (Whitesides, 2006; Tian & Finehout, 2009; Nguyen, Wereley, & Shaegh, 2019). This is due to the fact that entire labs can be fitted on a microfluidic chip, making it a "lab on chip" (Jung, Han, Choi, & Ahn, 2015; Temiz, Lovchik, Kaigala, & Delamarche, 2015; Ho, Ng, Li, & Yoon, 2015). This disciplinary topic has been widely applied to focus, separate, and trap micro-size particles, and has played an increasingly important role in applications that involve single-cell biology and the detection and diagnosis of diseases (Gong & Sinton, 2017; Yamada, Shibata, Suzuki, & Citterio, 2017; Fernandes, Gernaey, & Krühne, 2018; Lu, Caen, Vrignon, Zonta, El Harrak, Nizard, & Taly, 2017). Therefore, the fabrication of microfluidic devices

becomes essential. One way to fabricate microfluidic devices is micromachining of silicon and glass, which is mainly used for micro-electromechanical systems (MEMS) (Ho & Tai, 1998). Traditional nanotechnology requires a cleanroom and well-trained personnel, which greatly increases the cost of the microfluidic device fabrication process. The cost of a cleanroom can be about \$1000 per square foot, which does not take into account the time and cost for training the researchers (Whyte, 1999; Walsh III, Kong, Murthy, & Carr, 2017).

Verpoorte (2002) discussed the applications of microfluidics in clinical and forensic analysis, where developments in analyte categories of abuse, therapeutic and biofluid drugs, explosive residues, biofluid ions, enzymes, antibodies, peptides, and clinical DNA were evaluated. An area of interest in this review was the small-molecules category, particularly drugs of abuse and therapeutic drugs. One of the advantages of microfluidics is that, due to the micron-size structures, flow happens rapidly, thus decreasing the sampling and analysis time for drug detection. According to Yuan and Shiea (2001), using microfluidic chips to create a fast mass spectral analysis of sildenafil only took two minutes. One of the downsides of this method is that the cost of analyzing such tiny particles at high speed is expensive, as it requires high-speed cameras, which are still priced highly in the market. Pinto, Sousa, Cardoso, and Minas (2014) used a low-cost process without using a cleanroom, where epoxy-based negative photoresist (SU-8) was evaluated for use as a mold material, due to its photosensitivity and transparency. However, SU-8 is sensitive to surrounding parameters, which means that it needs to be optimized before a stable condition can be found for specific microstructures. The parameters and optimizations criteria need to be changed for different microstructures. This can take time, due to different processing parameters and structural dimensions for microfluidic chips.

This study demonstrates a low-cost and high-resolution method for fabricating microfluidic devices by using a soft-lithography technique. Soft lithography, which was developed in the late 1990s (Abdelgawad et al., 2008; Mammen, Choi, & Whitesides, 1998) is a kind of technique for fabricating or replicating microstructures. "Soft" means that it uses elastomeric materials. Polydimethylsiloxane (PDMS) has been found to have a number of advantages over silicone and glass, which were the initial materials used for the fabrication of microfluidic chips (Sia & Whitesides, 2003; Isiksacan, Guler, Aydogdu, Bilican, & Elbuken, 2016). PDMS provides optical transparency for the observation of the target particles flowing in the microfluidic channel.

---

PDMS is also compatible with biological flows and bio-particles, as it cannot be penetrated by water, yet is permeable to gases. PDMS is also nontoxic to cells and will not jeopardize the quality of the cells used (Mata, Fleischman, & Roy, 2005; Siddique, Meckel, Stark, & Narayan, 2017). The approach used in this study aimed to develop a low-cost fabrication method for microfluidic devices, based on a soft-lithography technique without using a cleanroom environment. Basically, the dry film photoresist was exposed under an LED light source, and a transparent mask was used to pattern microstructures on the dry film. First, a layer of dry film resist was laminated onto a copper plate using a thermal laminator. Next, an ultraviolet (UV) exposure was made through a transparency photo mask, after which the exposed dry film was developed, rinsed, and dried in order to obtain the master mold. The microstructures were then replicated into polydimethylsiloxane (PDMS) to form a microfluidic channel for experimental use. This fabrication method enables microfluidic applications in biology, biomedical, and medical areas without requiring a cleanroom environment.

## Project Rationale

In this paper, the authors describe a fabrication system for manufacturing microscale structures inside microfluidic channels at high resolutions up to 60  $\mu\text{m}$ . This system uses simple materials and tools to achieve the discussed results, ultimately leading to its low-cost nature. Time-efficient attributes are also an inherent advantage that allow microfluidic master models to be created quickly and easily through short processing times. The rationale of this project was to expose photoresist dry film under UV light. This was done by placing a mask over the film during exposure. Specific microfluidic structures were realized by designing the mask in desired patterns and shapes. Final microfluidic devices were fabricated in PDMS using soft lithography techniques. Master molds were manufactured in a dry film photoresist by lithographic patterning, whereby a layer of photoresist dry film was first laminated onto a copper plate using a thermal laminator. Then, after cool-down, the film was exposed to UV light through a transparency photo mask. Afterwards the exposed photoresist dry film was developed in a sodium carbonate solution. PDMS resin and catalysis were thoroughly mixed, degassed, and then cast on the master. After curing, the PDMS replica was peeled off of the master, cut and punched, and then bonded with another thin PDMS layer after corona surface treatment. Using this method, microfluidic and microstructure channels with rectangular cross-sectional shapes were fabricated.

Compared with earlier fabrication methods that require a cleanroom environment, expensive equipment, and complicated processes, this method can be used to fabricate microfluidic channels with various microstructures but without any of the disadvantages of conventional lithography-based techniques. Specifically, achieving resolutions that can be used for different purposes, such as rapid prototyping of

microfluidics for detection of diseases. In this experiment, multiple masks were used that exhibited different patterns, shapes, and sizes for testing the resolution of the system.

## Fabrication System and Materials

### System Overview

The system primarily consisted of photoresist dry film, a thermal laminator, and a UV-LED light source. First, the photoresist dry film was thermally laminated onto a copper plate. Next, a mask of the desired microfluidic channel was used in conjunction with the UV-LED light source to expose the desired sections of the photoresist dry film for a certain amount of time. A sodium carbonate bath was then used to remove the un-exposed film. After cleaning and drying the copper plate with the exposed dry film, PDMS can be poured over the master and then cured using an oven. Once cured, the PDMS mold can be removed and permanently bonded onto a glass slide using the corona treatment.

### Lamination

First, cut a piece of a clear thermal laminating sheet, a piece of photoresist dry film, and remove the protective covering of a copper plate. Clean the top of the copper plate with isopropyl alcohol and dry using instrument air. Once completely dry, place the copper plate in the center of the prepared thermal laminating sheet. Now, use tape to pull back another side of the photoresist dry film protective covering. This film has a protective covering on both sides; the bottom of the film is the side that is closer to the inner diameter of the roll from which it was removed. Once the bottom protective covering starts to peel off, roll back the film some more and stick the exposed film just above the copper plate and onto the piece of clear thermal laminating plastic.

Apply pressure to help the dry film stick to the clear plastic. With the laminator heated, feed the assembly into the laminator with your fingers, while holding the film. Still holding the dry film, the protective layer of the dry film will be removed as the laminator pulls the assembly in. Once the assembly exits the laminator, inspect it. The only requirement is that the dry film on top of the copper plate is smooth with no bubbles or imperfections. Imperfections are allowed only if they are minor and not in an area where a microfluidic structure will be.

After lamination is complete, use a knife and cut the copper plate from the clear plastic. The dry film should be bonded to the clear plastic and the copper plate, though the copper plate is not necessarily bonded to the clear plastic. If you are careful and do not cut through the clear plastic, you can re-use it, utilizing the back side to mount the copper plate for next time. Once the copper plate and film are removed from the clear plastic piece, move the copper plate into complete darkness and let it cool to room temperature.

## UV-LED exposure

While the copper plate is cooling, check to make sure the LED light source (see Figure 1) is operating correctly. Once the bonded copper plate is cool, remove it from the box and place the desired transparency mask over it with a heavy glass slide on top. Place this setup under the UV-LED light source in the center with the recommended orientation. Expose the photoresist dry film to the UV light. Once complete, remove the copper plate and store it in complete darkness.

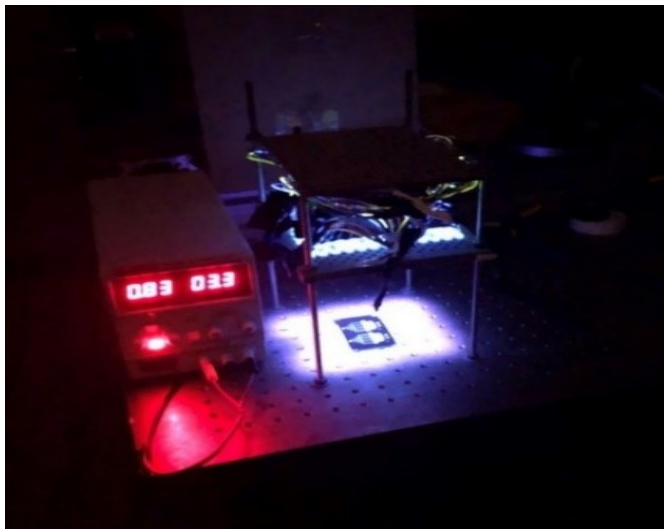


Figure 1. LED light source.

## Development

To prepare the development solution, pour distilled water into a pan, then add sodium carbonate to the pan. With the pan on a hot plate, heat the solution to an appropriate temperature to effectively reduce development time. Once the copper plate is finished being stored, use scotch magic tape to remove the top protective layer of the dry film. Be very careful not to remove the actual dry film from the copper plate. Confirm that the development solution is homogenous then use gloves to dip the bonded copper plate into the solution and slowly pulse the plate up and down. Every so often, pull the plate out of the solution to examine it more clearly and then place it back in the solution and begin slowly pulsing again. You will begin to see the copper plate's true color and then you will see that the transparency mask design is the only thing remaining. Practice and examination will be the determining factor of when development is complete. Once development is complete, slowly dip the copper plate into a pan of pure distilled water, and remove. Proceed very carefully to dry the plate using light instrument air. Figure 2 shows a plate that has completed development and dried. Once completely dry, the plate then can be used to make a PDMS mold.

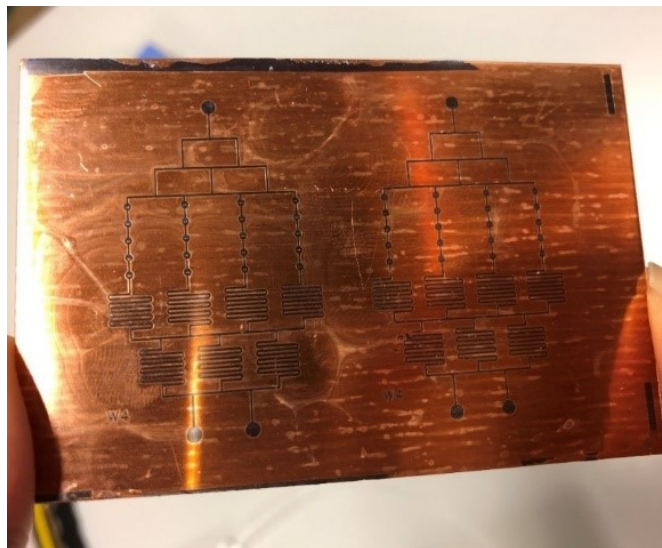


Figure 2. Copper plate with exposed photoresist dry film.

## PDMS

To make the PDMS concoction, using the silicone elastomer kit, measure 10 portions of Part A (resin) into a clear plastic cup and add 1 portion of Part B (catalyst) afterwards (see Figure 3).



Figure 3. Adding part A and part B together of the silicone elastomer.

Mix this concoction thoroughly until a homogenous substance is observed. Once thoroughly mixed, place the cup into the vacuum chamber (see Figure 4). As the air in the chamber is pumped out, all the air from the PDMS concoction

tion will rise and leave the chamber as well. Watch the cup to make sure the bubbles never leave the confines of the cup. If they do, a mess will be created, and the vacuum chamber seal will be degraded. To avoid this, turn off the pump or slightly open the ball valve to the environment.



Figure 4. Removal of air bubbles in the PDMS concoction.

While this is going on, a box can be made using the sides of a small cardboard box. You will want to create a container that the copper plate will fit snugly into, and into which the PDMS concoction will be poured. Wrap the aluminum foil around one side of the small box and remove it. Make sure the corners are secure enough to prevent any liquid from seeping through. Place the completely dry bonded copper plate into the aluminum foil box. Once all of the air is removed from the PDMS concoction and is completely clear, turn off the pump and open only slightly the ball valve to the environment in order to bring the vacuum chamber back to atmospheric conditions. Be careful not to open the ball valve too much, effectively tipping the plastic cup over. Remove the PDMS concoction from the vacuum chamber and pour it over the bonded copper plate that is in the aluminum foil box. Once all of the PDMS concoction is poured into the foil box, examine it for any new bubbles.

After curing the PDMS in an oven (see Figure 5), remove the assembly and examine the PDMS to see if it feels firm. Once cool, remove the aluminum foil from the assembly then cut away the PDMS around the edges of the copper plate. Once you have two parts, take the PDMS and cut it into its desired sections, depending on the transparency mask used. Place the PDMS section on the glass slide. Do this as many times as you have PDMS sections. Make sure the PDMS is flat against the glass and that there is no separation between the two (see Figure 6).



Figure 5. PDMS placed in oven for heating.

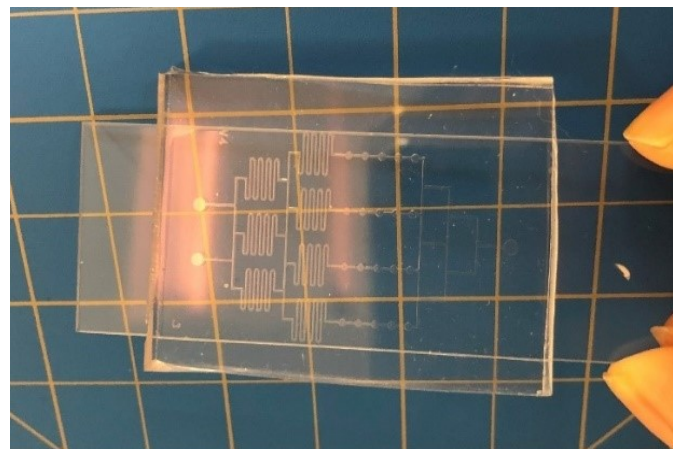


Figure 6. PDMS placed on glass slide.

## Corona Bonding

To permanently bond the PDMS to the glass slide, use the corona high-v equipment tool. This tool uses high voltage and, if not used properly, can cause serious damage to you and others. Place a sheet of clean paper in the laboratory hood, and place the PDMS glass slide on this paper. Turn the corona tool on and slowly move it back and forth over the PDMS glass slide (see Figure 7). Be careful not to create an electrical arc between the tool and the lab hood. It should be noted that during this time, touching the metal lab hood may result in electrocution. Turn off the corona tool and examine the PDMS glass slide. If the PDMS has bonded to the glass slide effectively, it will be ready to be used for various experiments. Figure 8 shows how small drill holes can be made for the inlet and outlet ports, while connecting a syringe using tubing to produce fluid flow through the microfluidic channels.



Figure 7. Bonding PDMS to glass slide.

## Experimental Results

To test the system resolution, an initial channel width of  $100\ \mu\text{m}$  was used (see Figures 8 and 9). Utilizing scanning electron microscope imaging, Figure 8 shows a copper plate after being developed in the sodium carbonate solution. The photopolymer dry film on the copper plate depicts straight lines with minimal defects. Figure 9 shows the results of taking this same channel design and transferring it to a PDMS mold. This image was taken using a compound microscope exhibiting straight lines, indicating vertical channel walls. Similarly, Figure 10(a) shows micro pillars ( $D = 60\ \mu\text{m}$ ) in a copper plate after being developed in the sodium carbonate solution. Figure 10(b) is the corresponding microfluidic channel in PDMS taken by a camera mounted to the microscope. Both groups of testing structures present sharp edges, which reflect a high-resolution fabrication technique.

The UV-LED light structure was used to analyze the optimum height from the copper plate required for development of the photoresist dry film. Figure 11 shows the characteristic light intensity of the LED light source in relation to the distance  $z$  from the copper plate. It can be seen that, as the distance between the copper plate and light source increases, the intensity is weakened. Therefore, the determination of the light intensity and its distance between the master molds is critical to the performance of exposure and also the resolution of the microfluidic device.

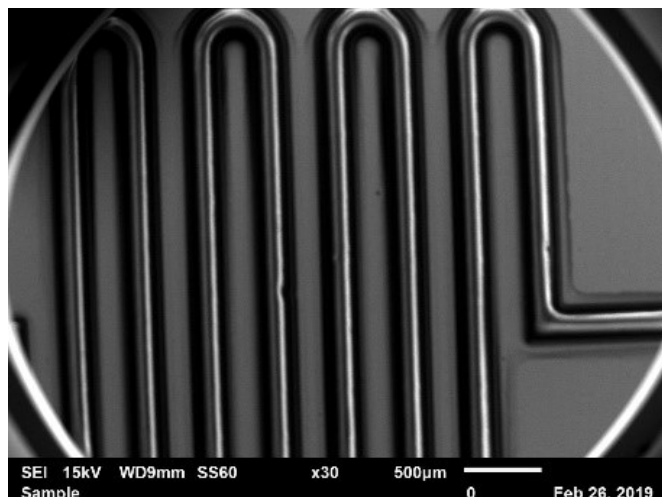


Figure 8. SEM image of the developed copper plate. The width of the rectangular structure is  $100\ \mu\text{m}$ .

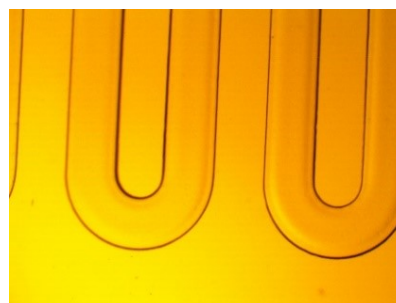
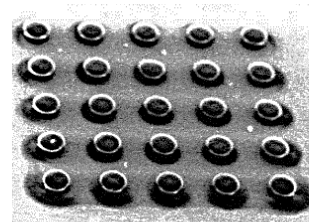
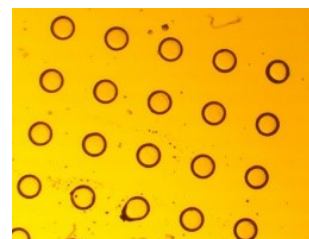


Figure 9. Microfluidic channel in PDMS taken by a camera mounted to the microscope. The width of the rectangular structure is  $100\ \mu\text{m}$ .



(a) SEM images of the developed copper plate with  $D = 60\ \mu\text{m}$  pillars.



(b) The corresponding microstructures fabricated in PDMS.

Figure 10. The developed copper plate.

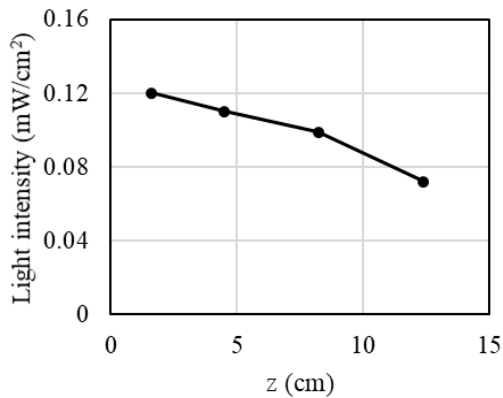


Figure 11. LED light source intensity under the effect of the distance between light source and UV meter.

## Conclusions and Future Work

In this study, the authors developed a low-cost soft-lithograph master mold system that used photoresist dry film exposed to a UV-LED light on a copper plate. Overall, the system showed success at resolutions of 60 $\mu$ m-wide channels. These same types of master molds have been made in the past using conventional lithography techniques that utilize cleanrooms, expensive equipment, and complicated processes. The advantages of the system presented here include its low-cost, simple operation, and short processing times. Using only common materials and components, inexpensive production of microfluidic master molds can be realized quicker and easier. Also, specially trained personal are not needed for operation. This system can be used in many fields in which the researchers are interested in conducting fundamental research in biological and biomedical areas and/or developing practical and low-cost microfluidic applications focusing on bioparticles, separation and sorting, and especially where rapid-prototyping is advantageous. In the future, through calibrating UV-LED light intensity, exposure time, and development time, higher resolutions can be expected. There is a potential for attaining a maximum resolution of 30  $\mu$ m for certain microfluidic structures with this technology.

## Acknowledgements

This work was supported by the start-up grants from the School of Engineering and Undergraduate Research at Purdue University Northwest.

## References

- Abdelgawad, M., Watson, M. W., Young, E. W., Mudrik, J. M., Ungrin, M. D., & Wheeler, A. R. (2008). Soft lithography: masters on demand. *Lab on a Chip*, 8(8), 1379-1385.
- Fernandes, A. C., Gernaey, K. V., & Krühne, U. (2018). Connecting worlds—a view on microfluidics for a wider application. *Biotechnology advances*, 36(4), 1341-1366.
- Gong, M. M., & Sinton, D. (2017). Turning the page: advancing paper-based microfluidics for broad diagnostic application. *Chemical reviews*, 117(12), 8447-8480.
- Ho, C. M., & Tai, Y. C. (1998). Micro-electro-mechanical-systems (MEMS) and fluid flows. *Annual review of fluid mechanics*, 30(1), 579-612.
- Ho, C. M. B., Ng, S. H., Li, K. H. H., & Yoon, Y. J. (2015). 3D printed microfluidics for biological applications. *Lab on a Chip*, 15(18), 3627-3637.
- Isiksacan, Z., Guler, M. T., Aydogdu, B., Bilican, I., & Elbuken, C. (2016). Rapid fabrication of microfluidic PDMS devices from reusable PDMS molds using laser ablation. *Journal of Micromechanics and Microengineering*, 26(3), 035008.
- Jung, W., Han, J., Choi, J. W., & Ahn, C. H. (2015). Point-of-care testing (POCT) diagnostic systems using microfluidic lab-on-a-chip technologies. *Microelectronic Engineering*, 132, 46-57.
- Lu, H., Caen, O., Vrignon, J., Zonta, E., El Harrak, Z., Nizard, P., & Taly, V. (2017). High throughput single cell counting in droplet-based microfluidics. *Scientific reports*, 7(1), 1366.
- Mammen, M., Choi, S. K., & Whitesides, G. M. (1998). Polyvalent interactions in biological systems: implications for design and use of multivalent ligands and inhibitors. *Angewandte Chemie International Edition*, 37(20), 2754-2794.
- Mata, A., Fleischman, A. J., & Roy, S. (2005). Characterization of polydimethylsiloxane (PDMS) properties for biomedical micro/nanosystems. *Biomedical microdevices*, 7(4), 281-293.
- Nguyen, N. T., Wereley, S. T., & Shaegh, S. A. M. (2019). *Fundamentals and applications of microfluidics*. (2<sup>nd</sup> ed.). Artech house.
- Pinto, V., Sousa, P., Cardoso, V., & Minas, G. (2014). Optimized SU-8 processing for low-cost microstructures fabrication without cleanroom facilities. *Micromachines*, 5(3), 738-755.
- Sia, S. K., & Whitesides, G. M. (2003). Microfluidic devices fabricated in poly (dimethylsiloxane) for biological studies. *Electrophoresis*, 24(21), 3563-3576.
- Siddique, A., Meckel, T., Stark, R. W., & Narayan, S. (2017). Improved cell adhesion under shear stress in PDMS microfluidic devices. *Colloids and Surfaces B: Biointerfaces*, 150, 456-464.
- Temiz, Y., Lovchik, R. D., Kaigala, G. V., & Delamarche, E. (2015). Lab-on-a-chip devices: How to close and plug the lab? *Microelectronic Engineering*, 132, 156-175.
- Tian, W. C., & Finehout, E. (2009). *Microfluidics for biological applications* (Vol. 16). Springer Science & Business Media.
- Verpoorte, E. (2002). Microfluidic chips for clinical and forensic analysis. *Electrophoresis*, 23(5), 677-712.

- 
- Walsh III, D. I., Kong, D. S., Murthy, S. K., & Carr, P. A. (2017). Enabling microfluidics: from clean rooms to makerspaces. *Trends in biotechnology*, 35(5), 383-392.
- Whitesides, G. M. (2006). The origins and the future of microfluidics. *Nature*, 442(7101), 368.
- Whyte, W. (1999). *Cleanroom design*. Wiley.
- Yamada, K., Shibata, H., Suzuki, K., & Citterio, D. (2017). Toward practical application of paper-based microfluidics for medical diagnostics: state-of-the-art and challenges. *Lab on a Chip*, 17(7), 1206-1249.
- Yuan, C. H., & Shiea, J. (2001). Sequential electrospray analysis using sharp-tip channels fabricated on a plastic chip. *Analytical chemistry*, 73(6), 1080-1083.

## Biographies

**RAN ZHOU** is an assistant professor in the Department of Mechanical and Civil Engineering at Purdue University Northwest. Since she joined PNW in 2018, her research interests include microfluidic separation and focusing of microparticles and cells, thermofluids, bioMEMS, microfabrication of biological lab-on-chip system, and acoustic bubble dynamics. Dr. Zhou received her PhD in Mechanical Engineering from Missouri University of Science and Technology (MST, formerly University of Missouri - Rolla) in 2017, honored with the College Dean's Scholar award. Dr. Zhou may be reached at [zhou970@pnw.edu](mailto:zhou970@pnw.edu)

**MARK PARRA** is a graduate student in the Department of Mechanical and Civil Engineering at Purdue University Northwest. He graduated in May, 2019. Mr. Parra may be reached at [mwparra@pnw.edu](mailto:mwparra@pnw.edu)

**ATHIRA NAIR SURENDRAN** is an undergraduate student in the Department of Mechanical and Civil Engineering at Purdue University. She graduated in May, 2019, and is continuing her graduate studies at Purdue University Northwest. Ms. Surendran may be reached at [nair23.stw@pnw.edu](mailto:nair23.stw@pnw.edu)

# LOW-COST RAPID PROTOTYPING OF PERSONALIZED 3D-PRINTED MODELS OF KIDNEY AND ARTERY ANATOMY: A COST AND TIME EFFECTIVE APPROACH

Ginni Singh, University of Toledo; Matthew Franchetti, University of Toledo

## Abstract

It is easier to understand a medical problem with visual representation than being described in medical vocabulary. It gives patients an idea about the problem with their respective organ and the possible solutions. In this study, the authors created a prototype of kidney cortex by using a low-cost consumer-level 3D printer. In this paper, they provide an evaluation of its cost effectiveness compared to high-end 3D printers. To this end, a single patient's CT scan and MRI image of a kidney cortex was used to replicate the same using 3D printing. A cortex of a kidney was created using the fused deposition modelling method (FDM) with a flexible filament material. Insight into a cost analysis of the printer and products is provided here, but the biocompatibility and bio-functionality of the material used will be left for future research. The model created for this purpose was solely for surgical education and training. The cost of the kidney model created using the consumer-grade 3D printer was \$120, compared to a unit costing over \$560 produced by a high-quality professional-grade 3D printer. The study provided evidence that the use of low-cost 3D printing techniques for anatomically accurate models of kidneys is feasible using consumer-grade 3D printing techniques. The techniques resulted in lower costs and faster processing times versus professional-grade 3D printing. The prototypes experimented with in this study using low-cost consumer-level 3D printers can be a cost-effective and efficient tool for surgical education and training.

## Introduction

Three-dimensional (3D) printing is a method by which an actual structure is created via a layering technique using the computer-aided design software, which relays the signals to the 3D printer (Ahmad, AlAli, Griffin, & Butler, 2015). The manufacturing process in 3D printing is built up layer by layer rather than being cut from a larger block of material. It is done by subtractive manufacturing techniques like machining (Bak, 2003). The cost of a patient-specific 3D-printed model represents a limitation that merits discussion (Bernhard et al., 2016). This type of experimental study is a first-of-its-kind to create a prototype model of a kidney cortex by using a 3D printer that is easily affordable and leads to reduced production costs. By reducing costs, the technology provides new possibilities for visualizing complex anatomical structures through the generation of physical models to assist with surgical education and improve the under-

standing of complex anatomy (Watson, 2014). After the diagnosis is made, imaging is the only graphical representation to share with the patients so that they can visualize and understand the issues they have with their kidneys (Bernhard et al., 2016). Patients' initial reference level of understanding was low. However, Bernhard et al. (2016) found a 37.6% increase in the correct responses from patients in understanding the 3D-printed patient-specific physical model overall. This was achieved even after every single patient was provided with extensive verbal and written preoperative information as well as a detailed explanation of their CT scan images (Bernhard et al., 2016). Real and inexpensive models can provide easy accessibility of converting physical form to digital information and thereby facilitating the direct manipulation of digital data. This will lead to taking advantage of human abilities to grasp and manipulate physical objects and materials (Watson, 2014).

In this paper, the authors present the initial experimentation in creating such models and testing the feasibility of 3D printing of kidney and artery models using an inexpensive 3D printer at the university level. This is done for the purpose of showing the cost effectiveness of the procedure in order to improve patients' and medical students' education. Initially, 3D printing was done with one material each time for printing a kidney and the two-material capacity of MakerBot (2016) printers was tested for printing arteries, as they need to be thin and hollow. In comparison to the Objet 500 3D printer, the MakerBot also has the feature of two-material print with two extruder nozzles. The difficulty with the professional printer is that it requires the operator to have high-skilled technicians able to operate the equipment, due to high product and maintenance costs. On the other hand, almost anyone can use personal desktop printers like MakerBot. This is due to the ease of handling and low maintenance costs of the printer.

Although desktop printers ranging from home-assembled parts cost anywhere from \$200 to \$3000, the professional 3D printer can be very expensive and cost upwards of \$5,000,000 (Bak, 2003). These replicated organs are printed using two materials on a professional 3D printer for the best quality of product in the medical field. The outer layer is made transparent in most cases so that doctors can see structures, bones, and cancers, which help them to observe and perform surgery. This can reduce surgery time and patient risk. The recent availability of free, open-source software and online internet 3D printing service bureaus makes 3D printing available to ordinary health professionals, hospitals,

clinics, and even laypeople (Itagaki, 2015). Models can typically be manufactured within about 12 hours, which is much faster than can be obtained using online procurement. The major disadvantage is that the 3D printers used for medical applications are very expensive. High-quality 3D printers can cost more than \$30,000 (Itagaki, 2015).

## Methods and Materials

### 3D-Printed Model Fabrication with DICOM Files, CT Scan, and MRI Images

Single Digital Imaging and Communications in Medicine (DICOM) files for kidney cortex and arteries were first obtained from the University of Toledo Medical Center (UTMC) and converted into an STL file using a 3D slicer. There was single image for each one of them. These images were then uploaded into the MakerBot software called MakerWare. The patients belonged to UTMC and their identity was kept confidential.

### MakerBot 3D printer

The Replicator 2X is MakerBot’s experimental dual-extruder 3D printer. It comes with a fully enclosed steel chassis and boasts a heated platform for printing in ABS or PLA. It offers dual-extrusion functionality that adds a new level of creativity to 3D designs, which can be done without swapping or pausing. It weighs 27.8 lbs. and uses stl.obj and Thing file types for printing. Its layer resolution is 100 microns and has an SD card and USB connectivity. MakerBot uses a filament diameter of 1.75 mm (0.069 in), with a nozzle diameter of 0.4 mm (0.015 in). Using the Materialize Interacting Medical Image Control System (Mimics) software, the CT scan and the MRI files were segmented and created as a 3D model. After that, the Geomatics Design X software was used for smoothing, cleaning, and filling the holes. Also, the number of triangular faces was reduced with the use of mesh doctor from 80,000 to 60,000. Different software packages were used for smoothing purposes and also for importing the CT scan files to STL format: 123 designs, Mimics, SolidWorks, MakerWare, and Geomagic Design X.

### Study/Process Methodology

Table 1 presents the materials explored in the process of creating a replica of the human kidney. NinjaFlex and HIPS Dissolvable were used primarily for printing and ABS was used for molding. NinjaFlex is a thermoplastic polyurethane (TPU) (Rembor, n.d.) that offers flexibility, elasticity, and high-strength properties and is good for creating flexible and durable models. NinjaFlex is available in two diameters, 1.75 mm and 2.85 mm. In this study, 1.75 mm material was used for printing kidneys and arteries. Also, high-impact polystyrene (HIPS) (MatterHackers, 2019), which is

a dissolvable filament, was used as a support material. It is easily removed by D-Limonene solution and leaves a clean and high-quality print after dissolving (Rembor, n.d.). It does not require scraping, cutting, and cleaning that can damage the print, as is often the case with other materials. Arteries are much stiffer than the kidney itself. Arteries are isotropic, do not have a high degree of compressibility, or exhibit strain-hardening behavior (Shadwick, 1999). The kidney of a patient is printed, followed by the arterial tree. The angles between the arterial branches in the arterial tree were approximately 30-45 degrees. The combined version of a kidney with an arterial tree was kept for future work. The ideal settings for getting successful prints with the various filaments were achieved by trial and error. There are various factors (i.e., environment, printer model, model complexity, etc.) that should be considered during the printing process, which could make each case of 3D printing different.

Table 1. Printer settings for each filament.

Filament	Ninja Flex	HIPS Dissolvable	Maker Bot Flexible	ABS	PLA
Extruder Temp. (°C)	225	230	220	215	210-215
Platform Temp. (°C)	20	55	20	110	20
Travel Speed (mm/s)	15	50	50	75	150-215

The cost of printing each item on the 3D printer is divided into three categories: investment cost of the printer, material and maintenance cost of the printer, and the cost of labor and electricity (Sculpteo, 2019). Table 2 shows a comparison of these costs with respect to printer and materials.

Table 2. Price comparison of a 3D printer.

Material Name	Type	Cost/KG/Spool	Function
NinjaFlex	TPE (thermoplastic elastomer)	\$39.17	Works great as a diffuser
HIPS (high-impact polystyrene)	Dissolvable material	\$19.95	Support material in 3D printing
ABS (Acrylonitrile Butadiene Styrene)	Strong temperature-resistant material	\$29.00	Flame retardant
PLA (Polylactic acid)	Bioplastic which has a quick transition from liquid to solid	\$29.00	Eco-friendly

The three methods explored in this study for producing the model included:

- Direct Fused Deposition Modeling
- FDM with Dissolvable Filament
- Creation of a Negative Mold

## Direct Fused Deposition Modeling

The first method was a print-only method in which a single type of filament was used to print via FDM, or layer-by-layer, to create the kidney and the arterial tree separately. NinjaFlex, a flexible filament, was chosen to capture the physical characteristics of an actual arterial tree. NinjaFlex, a cutting-edge filament for 3D printers, is a specially formulated thermoplastic elastomer (TPE) that produces flexible prints with elastic properties, which also successfully performs as a diffuser (Rembor, n.d.). With a considerable amount of trial and error, the kidney models were printed through NinjaFlex. However, in printing a horizontal, hollow tube (for arteries), there was no support for the material to print shallow angles less than about 35-40 degrees. Anything below that would require support material to be printed in order to create a successful print. An attempt to create an arterial model failed, as it was realized that the printer would be incapable of such a feat with a flexible filament. The result shown in Figure 1 was achieved by using Polylactic acid (PLA) using a print-only method in which proper support material was used with the PLA being rigid. Polylactic acid (PLA) is biodegradable and ABS is non-biodegradable but recyclable as far as the implications of this materials are concerned with surgical implants (Sculpteo, 2019).



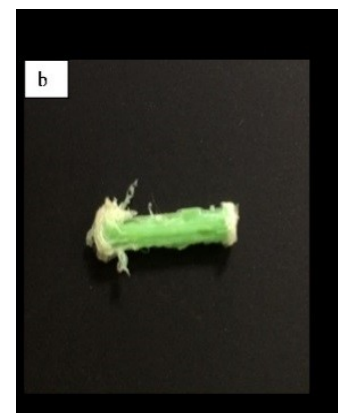
Figure 1. Print-only method using PLA.

## FDM with Dissolvable Filament

The print-and-dissolve method, being the second method for creating arteries, utilizes the MakerBot Replicator 2X special feature of two extruders, which allows for the use of two separate filament materials within the same print. With the advantage of this feature, two prints for one arterial tree were made, the outer being with a flexible material, the object which was needed for the end product. The outer layer was a dissolvable filament – HIPS Dissolvable. High Impact Polystyrene (HIPS) is a dissolvable filament which is very similar to Acrylonitrile Butadiene Styrene (ABS) and is mostly used as a support material in 3D printing. The dissolving process took about 36 hours and about 15 fluid oz. of D-Limonene at 5 oz. per 12 hours. Figure 2(a) shows the artery before being dissolved in D-limonene solution and Figure 2(b) shows the extra material being dissolved in order to get arteries. It has similar strength and stiffness compared to ABS and is effective as an alternative to sanding away regular support material. This was intended such that the inside of the arterial tree would be hollow and also to build the support structures and raft, if necessary.



(a) Before dissolving



(b) After dissolving

Figure 2. Test specimens dissolved in D-limonene solution.

## Creation of a Negative Mold

Since the space was intended to be hollow, the decision to print with HIPS Dissolvable was made, followed by dipping into molten flexible filament. Following cooling, the original print would be dissolved, leaving the end product: a thin, flexible shell in the shape of the arterial tree. This idea was dismissed initially but, after observing the success of printing a solid (not hollow) arterial tree out of a rigid filament, such as PLA, there was a potential for adapting to this method. This adaptation would be a combination of a molding technique and the dip-and-dissolve idea. A negative mold of the kidney body/tissue would be printed using simple 3D printing techniques with a rigid material such as ABS or PLA. Then, the arterial tree would be printed in a dissolvable filament, which could either be HIPS Dissolvable (dissolvable in D-Limonene) or ABS (dissolvable in Acetone) then sprayed with Flex Seal adhesive. The dissolvable would be removed after the Flex Seal was fully cured, leaving only the end product.

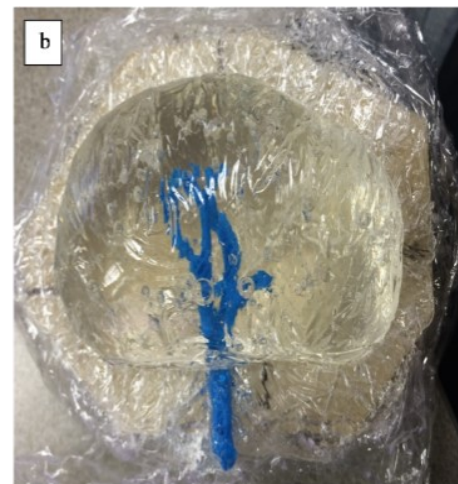
Since the negative mold for the tissue and the arterial structure were created, the arterial tree was placed within the void of the negative mold; the void was then filled with a soft silicone or agarose material. After that, it was left to cure before finally breaking away the mold. The importance of negative casting is that it eliminates the need for extensive work in transforming the STL file to a negative image to produce an FDM mold. This could be beneficial in customizing the kidney on a patient-to-patient basis. Figure 3 shows how Mimics and 123d Design software were used to model a printable STL file of a negative mold of the kidney tissue (or kidney body).

## Results and Discussion

In this study, an application of 3D printing for demonstrating the cost-effectiveness of developing a kidney prototype with an arterial tree was done in order to educate trainees in improved understanding of kidney anatomy. The segmentation, which included smoothing and masking of the CT scan and MRI images, took approximately seven hours using Mimics software. The average size of an adult human kidney is 10-13 cm in length by 5-7.5 cm in width and about 2-2.5 cm in thickness (i.e., 11.25 cm<sup>3</sup> by volume). In this experiment, the dimensions of the kidney cortex achieved by 3D printing was approximately 205 cm<sup>3</sup> by volume. This was because the model was an inflated (scaled up) version of a real human kidney. Figure 4 shows the 3D-printed model of the kidney cortex with 10%, 20%, and 15% infill. The difference in infill density is not best presented in a 2D picture, and the texture of the models differs vastly in its ability to deform and reform when squeezed. The density of this infill adjusts how much material is printed per unit of volume. The printer creates a lattice structure inside the volume, typically a honeycomb shape called shells.



(a) 3D-printed mold



(b) Uncured molded silicone model

Figure 3. Molds for kidney tissue.



Figure 4. Kidney models: 10%, 20%, and 15% infill, left-to-right, respectively.

In this case, three shells were used for printing the arteries. A lesser infill density in this case resulted in an object that is easier to squeeze. Models with different infill density can be typically manufactured within an average of 7-10 hours, depending upon the type of 3D printer used. The time needed to 3D print a kidney with NinjaFlex was 12-13 hours with 20% infill. These printing times depend on the quality of the printer, infill density, and the type of material. The PLA material consumed in the printing of the kidney was 46.29 grams and required a print time of 5 hours and 32 minutes. The resolution considered for the artery was 0.2 mm with 1.3 mm as outer diameter and 0.5 mm as the width of the artery. The nozzle diameter of the MakerBot printer for the FDM process was 0.4 mm. The cost of a 1kg spool of ABS material was \$49.95, and in producing a 3D print of a kidney approximately 0.5 kg material was used. So, the material cost of printing a kidney was \$4.62. The MakerBot 2X printer costs \$2200 and the average lifetime of these printers is 2500 print hours. Since the time consumed in printing was 5 hours and 32 minutes, the cost based on machine utilization was \$4.84. Assuming \$20/hr., the total cost for printing the kidney came to \$110. Therefore, the total cost of printing just the outer cortex of a kidney would be approximately \$119.46. Table 3 summarizes these data.

Table 3. Composition of a kidney model with 20% infill.

Print time	12-13 Hrs.
Infill	20%
Material Used	46.29 gm.
Print Resolution	0.2 mm
Cost of Material	\$4.62
Cost of Machine Time	\$4.84
Labor cost	\$100.00
Total Cost	\$119.46

The cost of printing a kidney cortex with Maker Bot is 21% less than the kidney printed by the Objet printers. Printing time for the arterial tree with NinjaFlex was 3 hours with a retraction speed of 0 mm/sec. Table 4 shows a cost comparison of the materials used for the fabrication of the kidney model.

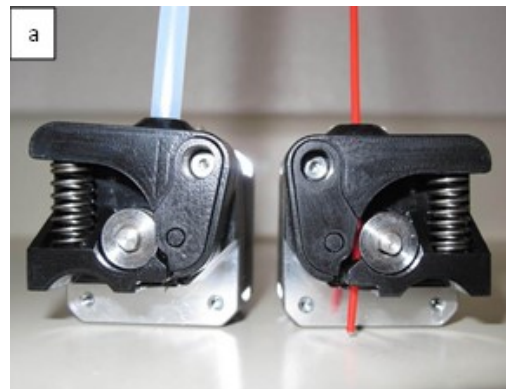
Table 4. Cost comparison of materials.

Printer Name	Replicator 2X	Objet 500 Connex
Material cost	\$20-40/kg	\$300-\$500/kg
Labor cost	\$20/Hr	\$27/Hr
Total fabrication cost	\$119.46/per model	\$560 per model
Maintenance cost	\$93.3/year	\$3047.79/year

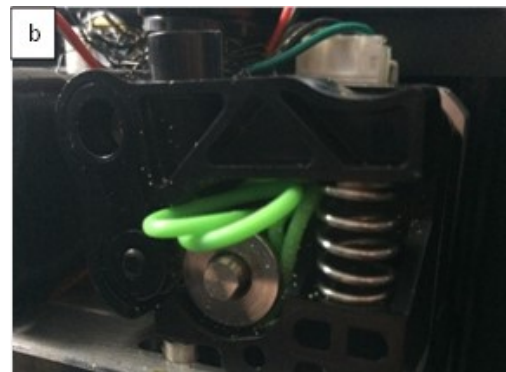
With ease of handling and maintaining the MakerBot 3D printer, creating a replica of a kidney is more cost effective to the model printed by using the Objet 500 printer. There is a large difference in the maintenance cost of the two printers, which can explain the complexity of handling such printers.

## Limitations

Many limitations can be discussed when using a lower-end 3D printer. Some limitations are based on material and others are based on the type of machine used. The MakerBot Replicator 2X was not designed with the intent of pushing a flexible filament through the nozzle along with the other extruder components. The extruder drives the filament between a burred motor attachment and a bearing (see Figure 5).



(a) MakerBot extruder



(b) NinjaFlex entanglement

Figure 5. Extruders

The inefficiency of this was experienced first-hand, as it relates to flexible filaments. The NinjaFlex, as flexible as it is, somehow was able to become tangled within the small confines of the extruder without actually getting fed into the nozzle. If at any point during a print, this filament gives the extruder any resistance, it will stop extruding. In such a

case, the entire printing process would be stopped, the printer would have to be disassembled, and the extruder would have to be cleaned in order to make sure the filament could pass through the nozzle. Only then could the printer be reassembled and reloaded with the filament. This process is very time consuming. When extruding, the NinjaFlex also tends to get baked onto the nozzle, causing restrictions to the filament (MatterHackers, 2016).

The burned material is very sticky and prevents a smooth feed, and cannot easily be cleaned from the nozzle, especially inside the nozzle, as it is not dissolvable by acetone like ABS, and it is not accessible enough to use a tool to scrape away the burned material. A potential solution to this is a nozzle with a tungsten-disulfide coating, shown on the website of MatterHackers (2016). The coating serves a similar purpose to Teflon on non-stick pans, and prevents the material from sticking to and getting baked inside and outside the nozzle. Another limitation is based on the functionality of the different software programs needed in order to convert the DICOM file, CT scan, and MRI files to the STL format. Also, further segmentation, smoothing, and mesh generation are completely dependent on the type of software used. For example, 123d Design would not perform a subtraction of volumes between a rectangular prism and the kidney tissue. The problem is that the STL file being used has a discontinuity somewhere within the mesh used to define the object.

## Conclusions and Future Research

3D printing can play an important and vital role in manufacturing organs for implantation and prosthetics for patients. It also plays an important role in education, training, and planning the surgical procedures from a student point of view in order to minimize errors (Itagaki, 2016). It can be a pivotal element with respect to medical education, if applied properly. This study was a first-of-its-kind in creating kidney and artery models from a low-end desktop 3D printer at the cost of \$120/model, as compared to \$560/model for educating medical students. This concept can further be researched and developed for the more cost-effective production of kidneys. This study provided evidence that low-cost consumer-level 3D printers can be cost-effective and efficient tools for medical professionals in creating kidney models for patient education and training purposes. The low cost and ease of use of the consumer-level 3D printers will allow for the rapid expansion of these kidney models and better patient outcomes based on improved training and education. However, the printed model of the kidney with built-in arteries are kept for future research. More insight is required for testing and understanding the material for sustainability concerns. Also, the materials that were used for developing the model using MakerBot should also be used in Objet printers to see the difference in the quality of the end products for comparison in more detail.

## References

- Ahmad, B., AlAli, A. B., Griffin, M. F., & Butler, P. E. (2015). Three-dimensional printing surgical applications. *Eplasty*, *15*, e37.
- Bak, D. (2003). Rapid prototyping or rapid production? 3D printing processes move industry towards the latter. *Assembly Automation*, *23*(4), 340-345.
- Bernhard, J. C., Isotani, S., Matsugasumi, T., Duddalwar, V., Hung, A. J., Suer, E., Baco, E., . . . Gill, I. S. (2016). Personalized 3D printed model of kidney and tumor anatomy: A useful tool for patient education. *World Journal of Urology*, *34*, 337-345.
- Itagaki, M. W. (2015). Using 3D printed models for planning and guidance during endovascular intervention: A technical advance. *Diagnostic and Interventional Radiology*, *21*(4), 338-341.
- MakerBot. (2016). *MakerBot Replicator 2x*. Retrieved from <https://pages.makerbot.com/ap-replicator-2x.html>
- MatterHackers. (2019). Retrieved from <https://www.matterhackers.com>
- Rembor, K. (n.d.). *Get started with CircuitPython*. Retrieved from <https://learn.adafruit.com>
- Sculpteo. (2019). *Your online 3D printing service*. Retrieved from <https://www.sculpteo.com>
- Shadwick, R. E. (1999). Mechanical design in arteries. *Journal of Experimental Biology*, *202*, 3305-3313.
- Stratasys. (2019). *Introducing the Stratasys F120*. Retrieved from <https://www.stratasys.com>
- Watson, R. A. (2014). A low-cost surgical application of additive fabrication. *Journal of Surgical Education*, *71* (1), 14-17.

## Biographies

**GINNI SINGH** is a PhD student in the Department of Mechanical, Industrial and Manufacturing Engineering at the University of Toledo. Ms. Singh may be reached at [Ginni.Singh@rockets.utoledo.edu](mailto:Ginni.Singh@rockets.utoledo.edu)

**MATTHEW FRANCHETTI** is an Associate Professor of Industrial Engineering and Industrial Technology at the University of Toledo. He also serves as associate dean of undergraduate studies. Dr. Franchetti received his PhD in 2003 and MBA in 2000 from the University of Toledo. He has worked as an industrial engineer and technical manager for the US Postal Service in Washington DC, and has conducted research at Daimler Chrysler, General Motors, and Ford before joining the MIME Department in the fall of 2007. Dr. Franchetti may be reached at [matthew.franchetti@utoledo.edu](mailto:matthew.franchetti@utoledo.edu)

# COMPUTATIONAL ANALYSIS OF ASYMMETRICALLY APPLIED HOT AND COLD STIMULI

Ahmad Manasrah, Al-Zaytoonah University; Mehdi Hojatmadani, University of South Florida;  
Rasim Guldiken, University of South Florida; Kyle Reed, University of South Florida

## Abstract

Temperature perception is known to be highly nonlinear, and previous research has demonstrated that this nonlinear perception could be used to invoke a feeling of constant cooling, even though the average skin temperature does not change. The research presented here employs a computational model of a human forearm to understand how the fluctuations of multiple thermal actuators affect the temperature below the surface of the skin. The simulation was validated using a physical model that consisted of a layer of polyurethane rubber approximating the skin, and a copper tube representing the core of the forearm. The thermal display device was simulated using twelve blocks of aluminum fixed on top of the modeled skin, which matched previous human experimental setups. The simulation results showed that the average surface temperature of the skin model did not change when the stimuli were applied. The results also showed that the effect of continuous cooling was present at depths up to 1.8 mm below the surface of the skin, which is deeper than what a human is able to sense. Several experiments using a continuous cooling effect were successfully conducted using the physical model to verify the simulation developed in this study. The results of the experiments showed that the temperature readings of the skin followed the same trend as the temperatures that were observed in the simulation as well as those expected, based on human experiments.

## Introduction

The aim of this study was to computationally analyze the thermal effects under the skin related to a previous psychophysical study (Manasrah, Crane, Guldiken, & Reed, 2016; Manasrah, Crane, Guldiken, & Reed, 2017) of a unique thermal display method. Perception of temperature is based on thermal flux and is nonlinear, so slower temperature changes are not noticed until the temperature has changed by several degrees (Kenshalo, 1976; Molinari, Greenspan, & Kenshalo, 1977). By taking advantage of the nonlinear nature of the temperature perception threshold, and using a combination of cooling and heating thermal cells, this method generates a continuous sensation of cooling. Despite individual fluctuations, no overall temperature change is applied, because a few thermal actuators are quickly cooled, while others are slowly heated simultaneously on the skin. The slow heating actuators are below the perception threshold so they are not detected, but the quickly cooling actuators are above the threshold; hence, they are detected and perceived. Figure 1 shows the thermal pattern. The results

of this method showed that a cooling sensation can be generated using asymmetrically applied hot and cold stimuli (Manasrah et al. 2016).

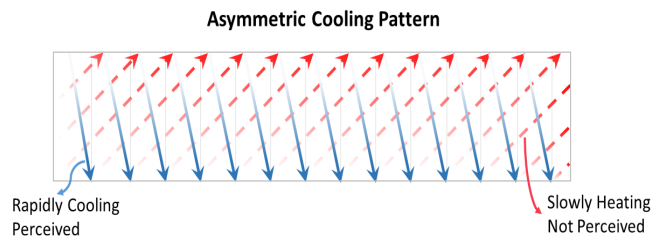


Figure 1. Illustration of asymmetric thermal stimulation pattern.

However, the temperature within human skin cannot be directly measured; thus, more information is needed to understand the temperature distribution within the skin and how the skin reacts to the thermal stimuli. To accomplish this, a simulation was utilized that would mimic the physical and thermal properties of the skin on the human forearm in order to provide information about the skin's temperature distribution and thermal behavior when an asymmetrical hot and cold thermal stimulus is applied. Computer simulations have been widely used in the past few decades by modeling systems and processes to study the characteristics and reactions in the physical world. They provide information and conclusions about the studied system or process that is difficult to measure directly. For instance, Murakami et al. (2000) used a simulation of airflow, moisture transport, and thermal radiation to predict the amount of heat released from the human body. Ho and Jones (2005) conducted a simulation study based on a thermal model to predict the temperature response of the skin.

In order to validate the results of the simulation, a physical structure of the forearm was built using a copper tube covered with a thin layer of polyurethane rubber serving as the skin of the forearm, as illustrated in Figure 2. The copper was heated so that the surface temperature of the polyurethane reached the desired temperature of the human skin. The results of this study can lead to a better understanding of temperature change effects on the skin at different depths. The results will also help us perform more challenging thermal display experiments and predict their outcomes.

## Background

It is widely known that thermal receptors located in the skin can thermally identify and discriminate between different objects by detecting the temperature differences that

occur on the skin. These receptors are crucial for regulating the temperature of the body. The perception of temperature depends on many factors including rate of change, area of stimulation, and temperature. The sensitivity of the skin is measured by the threshold at which the stimulus is first perceptible. For instance, the skin on the palm can detect a temperature increase of 0.2°C (at a rate of 2.1°C/s) when it is initially at 33°C (Stevens & Choo, 1998). However, for smaller rates of temperature change, an observer will not be able to detect a change in temperature up to 5–6°C (Stevens, 1991; Jones & Ho, 2008). A previous study (Kenshalo, 1976) applied a series of quickly cooling and slowly heating stimuli on the skin, using a 3x4 thermal actuator matrix. The rate of temperature change switched between 0.033°C/s and 0.1°C/s for the slow heating and quick cooling, respectively. The results showed that the average temperature on the surface of the skin remained constant, and a continuous cooling sensation was perceived throughout the stimuli. However, increasing the rate of change above 0.1°C/s had little effect on the temperature threshold (Kenshalo, Decker, & Hamilton, 1967; Murakami et al., 2000).

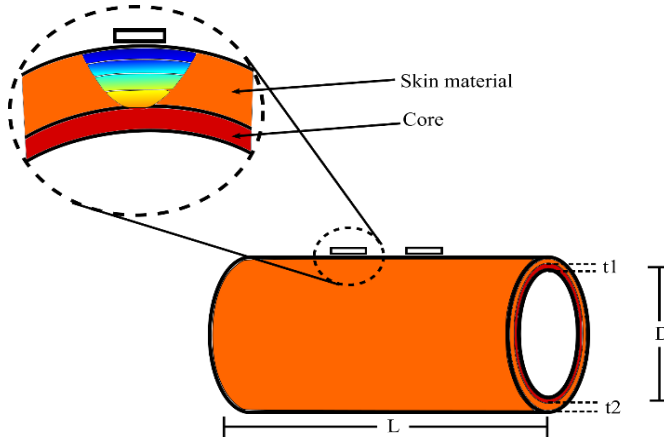


Figure 2. Schematic representation of the model with thermal actuators.

Most of the mathematical and computational thermal models were developed to study the thermoregulation system and the overall thermal comfort of humans (Handbook, 2013). For example, Rugh and Bharathan (2005) and Rugh et al. (2004) simulated a human based on a manikin, where the human physiological response and skin temperatures were studied to investigate the thermal effect of a climate control system of an automobile. Other studies have developed mathematical models to predict the human thermal response in different environments (Fiala, Lomas & Stohrer, 2001; Wang, Li, Kowk, & Yeung, 2002). Computer models were also used to study the performance and characteristics of different devices. Boetcher, Sparrow, and Dugay (2009) performed numerical simulations to test skin-surface temperature measurement devices. Numerical models were also used to investigate the effect of airflow and thermal noise in detecting tumors (Hu, Gupta, Gore, & Xu, 2004). Moreover,

McKnight (2010) studied the effects of thermoelectric devices on thermal receptors inside the skin. The simulation performed in this current study aimed to investigate the thermal perception of the skin when asymmetrical hot and cold stimuli are applied.

## Approach

For this model, a simple cylindrical structure was considered to approximate the shape of the forearm. The structure consisted of a core to represent the forearm, and a thin layer that covers the core to represent the skin. To match the physical verification, a copper tube with an outer diameter of  $D = 7.6$  cm, a length of  $L=30.5$  cm, and a wall thickness of  $t_1 = 0.23$  cm was chosen to represent the forearm. A polyurethane layer with a thickness of  $t_2 = 2$  mm was chosen to approximate the skin of the forearm. The thermal conductivity of polyurethane ranges from 0.2 W/mK to 0.3 W/mK in its rubber form (Material Database, 2019), which is similar to the thermal conductivities of the dermis and epidermis layers combined in the human skin, where the thermoreceptors are located (Cohen, 1977). The air that is in contact with the model was considered to be stagnant with a convective heat transfer coefficient of 10 W/m<sup>2</sup>K at 23°C ambient temperature. Furthermore, warm water was utilized to heat the tubular structure. The water runs through the tube to warm up the structure so that the surface temperature of the skin reaches 31.5°C. This ensured that the temperature of the water remained constant throughout the experiment.

## Analytical Solution

The temperature at the core of the cylindrical structure can be calculated using the concept of thermal resistance. The total resistance of the two-layer cylindrical system, shown in Figure 3, can be calculated using Equations 1 and 2 (Bergman, Incropera, DeWitt, & Lavine, 2011):

$$R_{total} = R_1 + R_2 + R_3 + R_4 \quad (1)$$

$$R_{total} = \frac{1}{2\pi r_1 L h_1} + \frac{\ln \frac{r_2}{r_1}}{2\pi L k_1} + \frac{\ln \frac{r_3}{r_2}}{2\pi L k_2} + \frac{1}{2\pi r_3 L h_2} \quad (2)$$

where,

- $r_1$  = inner radius of the tube
- $r_2$  = outer radius of the tube
- $r_3$  = outer radius of polyurethane
- $h_1$  = convective heat transfer coefficient of water flowing in a pipe
- $h_2$  = convective heat transfer coefficient of stagnant air
- $k_1$  = thermal conductivity of copper
- $k_2$  = thermal conductivity of rubber polyurethane

On the surface of the polyurethane material, the rate of heat flow can be represented by Equation 3 (Bergman et al., 2011):

$$q_{convection} = h_2 A (T_s - T_\infty) \quad (3)$$

where,

$A$  = surface area of the cylinder

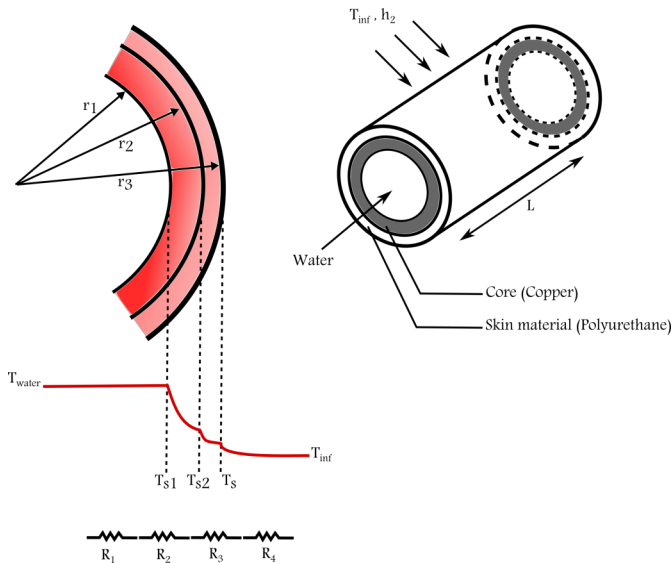


Figure 3. Temperature distribution of a copper cylinder covered with a polyurethane layer at steady state. The electrical resistances represent thermal resistance associated with the conduction and convection of heat.

Equation 3 can also be written as the ratio of the temperature gradient to the corresponding thermal resistance (Bergman et al., 2011). The value of  $R_1$  was calculated based on  $k_{water} = 6000 \text{ W/mk}$ . The result of Equation 4 shows that  $T_{water} = 32.2^\circ\text{C}$ . This result was later used to set the temperature of the water inside the copper pipe in order to obtain the desired skin surface temperature of  $T_{s2} = 31.5^\circ\text{C}$ . The relationships explained above can be seen in Equation 4:

$$q_{convection} = \frac{T_{s2} - T_s}{R_3} = \frac{T_{water} - T_{s2}}{R_1 + R_2} \quad (4)$$

## Finite Element Modeling

Figure 4 shows the modeled forearm and thermal display system, which were created using SolidWorks. The simulation was conducted using ANSYS v15.0. The model was set up using transient thermal analysis and had dimensions of 30.5 cm 7.8 cm, 8.2 cm, a volume of 340.72  $\text{cm}^3$ , and weighed 1.76 kg. The geometry of the model was sliced at four locations along the x- and the y-axes, using ANSYS

Design Modeler in order to better control the mesh size in the stimulation area, which is the area underneath the thermal actuators. This procedure resulted in 24 bodies and 62 bonded contact regions.

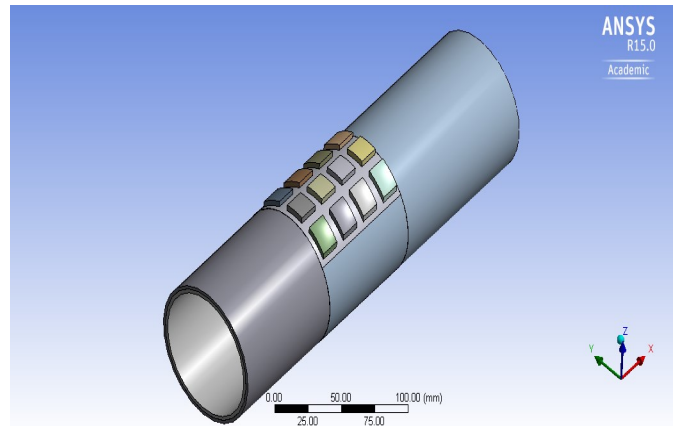


Figure 4. ANSYS model of the copper cylinder with thermal actuators (ANSYS, 2018).

Furthermore, aluminum plates (15 mm x 15 mm x 3.8 mm) were chosen to represent the thermal actuators in the model, instead of using ceramic Peltier devices that were used in the twelve-channel thermal display device (Kenshalo, 1976) illustrated in Figure 5. The reason for this substitution was to simplify the thermal display apparatus in the model. Initially, the primary purpose of using Peltier devices in the experiments was to apply temperature differences on the forearm. Therefore, an aluminum plate that applies the same temperature difference on the modeled arm is equivalent. Moreover, the thermal actuators in the apparatus were also covered with aluminum plates that were directly in contact with the skin.



Figure 5. Apparatus used in the continuous cooling experiments.

For the cylindrical structure, the governing differential equation of the polyurethane layer in the radial direction is represented in Equation 5:

$$\frac{1}{r_2} \left( \frac{\partial}{\partial r} \right) \left( r_2 \frac{\partial T}{\partial r} \right) = \frac{k_2}{\rho_2 c} \left( \frac{\partial T}{\partial t} \right) \quad (5)$$

where,

- $\rho_2$  = density of polyurethane
- $c$  = specific heat of polyurethane

The boundary conditions of the polyurethane layer are:

$$T(r_2) = 31.5^\circ\text{C}$$

$$-k \frac{dT}{dr} \Big|_{r=r_3} = h_2 (T(r_3) - T_\infty)$$

$$T(r)_{r=0} = 32.5^\circ\text{C}$$

The model was meshed using four sizing modules in four primary geometries: the copper tube, the stimulation area, the twelve actuators, and the rest of the polyurethane layer. The copper tube and the polyurethane layer were meshed using an element size of 1 cm, while the actuators were meshed using an element size of 0.3 cm. The main focus in this simulation was to approximate the skin on the area of stimulation. Therefore, the copper tube, the twelve actuators, and the rest of the polyurethane layer were coarsely meshed in order to save processing time. Moreover, finer element sizes were tested on these geometries; however, they did not have a significant impact on the results. On the other hand, several element size trials were attempted on the area of stimulation, ranging from 1 cm to 0.1 cm. The goal was to create fine-enough nodes inside the stimulation area and on its surfaces. An element size of 0.2 cm generated three nodal layers in the stimulation area, as illustrated in Figure 6, and resulted in 56,174 nodes in the model; hence, a 0.2 cm element size was implemented. A 0.1 cm element size was also tested and resulted in 221,360 nodes; however, it did not significantly change the final results. Also, the finer mesh increased the processing time significantly. The generated mesh of the model had a fine relevance in the center, a high smoothing factor, and a slow transition between the nodes.

Five temperature modules, one convection module, and one insulation module were applied to govern the boundary conditions of the simulation. The initial temperature was set at 31.5°C, which represented the surface temperature of the skin. The first temperature module was applied on the copper tube, keeping its operating temperature at 32.2°C, which is the calculated temperature at the core of the cylindrical structure. Because of the excellent thermal conductivity of copper, the temperature differences across the tube wall were neglected. The other four temperature modules were used to apply the continuous cooling sequence on the twelve actuators. The heating/cooling pattern was applied diagonal-

ly in the actuators, as illustrated in Figure 7, using a 30/10-second heating/cooling rate. The convection module was applied on the surface of the skin to simulate the environment around the forearm. The convective heat transfer coefficient was set to 10 W/m<sup>2</sup>K at 23°C ambient temperature. The insulation module was applied on the surfaces of both ends of the model, forcing the heat to be dissipated radially across the copper and the skin. The transient thermal analysis of the model had 24 steps and 240 seconds for the 30/10 heating/cooling rate, which resulted in a step size of 10 seconds. Each step was divided into 20 substeps. Different substep sizes were also tested to investigate the effect of time discretization on the temperature readings. The results did not show a difference in temperature readings when substeps were changed. Four temperature probes (NTC Thermistor bead 10 KΩ 3478K) were added in the stimulation area to record the temperatures under, and between, the actuators. The temperatures were recorded at different depths between 0 cm and 0.2 cm. These temperature recordings were later compared to the actual probe readings from the physical experiment.

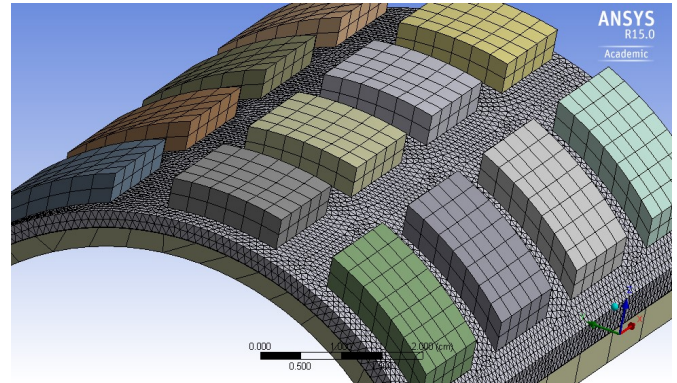


Figure 6. Meshing of the stimulation area (ANSYS, 2018).

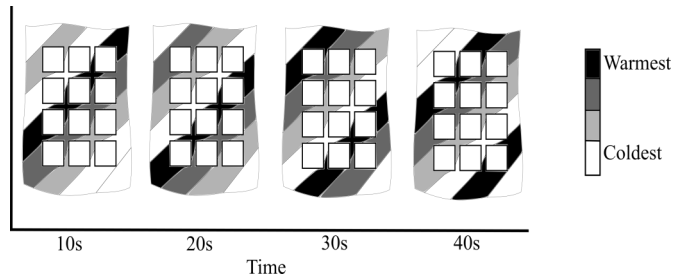


Figure 7. The diagonal pattern used in the simulation. For every actuators that is cooling, three actuators are heating.

## Physical Validation

In order to validate the results of the simulation, where the twelve-channel dynamic thermal display was used on an approximate model of the skin, a physical experimental model of the simulation was built. The physical model of the forearm was constructed using a 30.5 cm-long copper

tube. The skin was approximated using a 30 cm x 48 cm polyurethane sheet. A water bath and a pump were used to run 32.2°C warm water in the copper tube to generate heat in the physical model, based on the results of the analytical solution. The relatively high thermal conductivity of copper decreased the transient time that it took the physical model to warm up to the desired temperature.

## Assembly

The copper tube was connected to the water bath and pump using hoses, rubber couplings, and plastic fittings on both ends. Figure 8 shows that the polyurethane sheet was tightly applied on the tube. The four probes were embedded in the 2 mm thick polyurethane to record the temperature of the material at four different locations. Similar to the temperature probes in the simulation, the probes were placed so that two would read the temperature of the skin directly under two different actuators, while the other two probes were placed between the actuators. Because of the nature of the preparation procedure, the depth of each probe was not known during the experiments. The depths were determined after the experiments by cutting the polyurethane sheet using a stencil knife. The depths of the probes and the temperature readings were later compared against the results of the simulation.

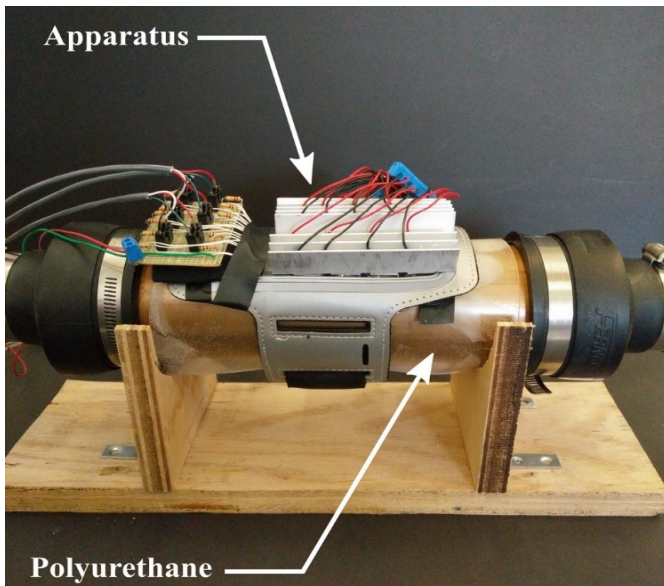


Figure 8. The setup used for the experiments.

The thermal display apparatus was placed on top of the skin and fixed around the copper tube. The apparatus was aligned with the skin's temperature probes to ensure that two probes were placed under two actuators and another two were placed between the actuators. The whole system was then elevated 10 cm and placed horizontally on a wooden structure for ease of access.

## Experimental Procedure

At the beginning of each experiment, the water bath pumped 32.2°C warm water through the copper tube that was covered with a 2 mm-thick sheet of polyurethane. The water bath operating temperature fluctuated between 32°C and 32.2°C; however, the surface temperature of the model was not affected by the fluctuation. Moreover, the surface temperature was tested at the beginning and end of each experiment, using a non-contact laser temperature gun. When the surface temperature settled at 31.5°C, the thermal display apparatus was applied to the physical model. The experimental set was divided into ten phases using a 30/10 diagonal heating/cooling time rate at ten different average temperatures between 25.5°C and 33.5°C. Each phase of the experimental set lasted four minutes. The first minute of each phase was not analyzed, in order to allow the thermal stimulation to settle on consistent heating/cooling cycles. The temperature readings of the four probes in polyurethane were then recorded every 100 ms throughout the last three minutes. The surface temperature of the polyurethane was measured at the end of each experiment to ensure no temperature build-ups occurred in the skin.

## Results

### Finite Element Model

In this model, the simulation predicted the temperature of the polyurethane layer in the area under the thermal stimuli. The results showed that the average surface temperature of the polyurethane layer was 31.5°C, which was the desired skin temperature. Figure 9 shows the temperature readings of the probes under the actuators at a depth of 0.2 mm, 1 mm, and 1.8 mm under the surface of the polyurethane layer using a 30/10 heating/cooling rate. Due to the duplication of the two probe readings, only data from one probe are presented here. The oscillation of the temperature decreased with the depth of the approximated skin layer; however, the average temperature increased as the probes got closer to the surface of the copper tube. Similarly, the temperature readings of the area between the actuators increased with the depth of the skin layer, as illustrated in Figure 10.

### Physical Experiments

As part of this study, an experimental study was conducted to verify the developed simulation models. Four probes were used to validate the results of the simulation. Figure 11 shows the temperature readings of a probe under one of the actuators, using a diagonal 30/10 heating/cooling rate at different average temperatures of thermal stimuli. Arm temperature was also included in Figure 12 and was simulated using hot water. Furthermore, the temperature readings of the probes located between the actuators also increased as the average stimuli temperature increased; however, the

fluctuations in the readings were more subtle, as illustrated in Figure 12. The temperature of the water inside the arm did fluctuate between 32°C and 32.2°C; however, the fluctuation was random and well confined. The temperature reading 1 mm under the actuator changed between 31.8 and 32 and the change had a repeating pattern, unlike the temperature of water.

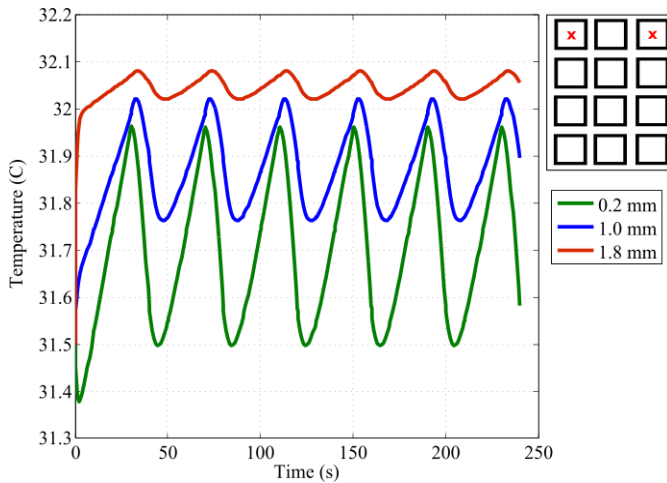


Figure 9. Temperature inside the polyurethane layer under the actuators at three different depths. The schematic representation of the actuators shows the locations of the thermistors (marked by an x).

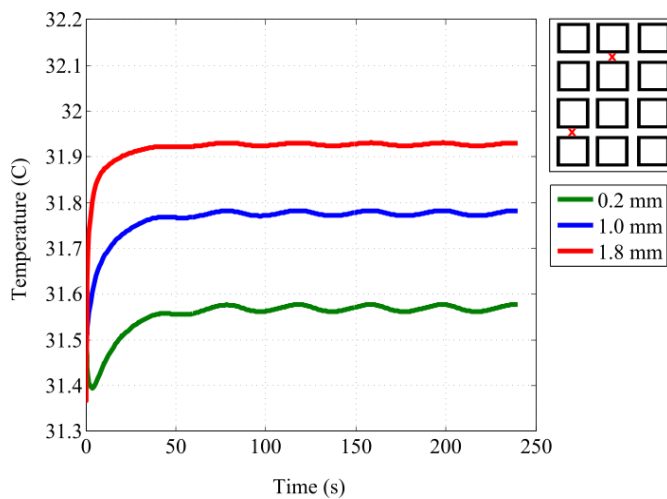


Figure 10. Temperature readings inside the polyurethane layer between the actuators at three different depths. The schematic representation of the actuators shows the locations of the thermistors (marked by an x).

## Comparison

The experimental setup served as a physical validation for the simulation. Therefore, a comparison was conducted between the temperature readings of the experiment and the results of the simulation. A stencil knife was used to cut the

polyurethane layer near the probes to measure their depths in the material. The results showed that all four probes were about 1.6 mm below the surface of the polyurethane layer. Figure 13 shows that the temperatures of the physical experiment and the simulation model at 1.6 mm under an actuator had similar readings. The probes used in the experiments had a 0.5–0.6 mm body length at which the temperature could be read. Hence, in Figure 14, the comparison was conducted against two simulation readings at 1.6 and 1 mm. The figure represents the temperature readings in the physical experiment and the simulation between the actuators. The comparison shows that both temperatures were constant in that area; however, there was a 0.2°C to 0.4°C difference between them. It was hypothesized that the slight deviations from the reference temperature could be attributed to imperfections in the manufacturing of polyurethane, which changes the thermal conductance of the material at different points.

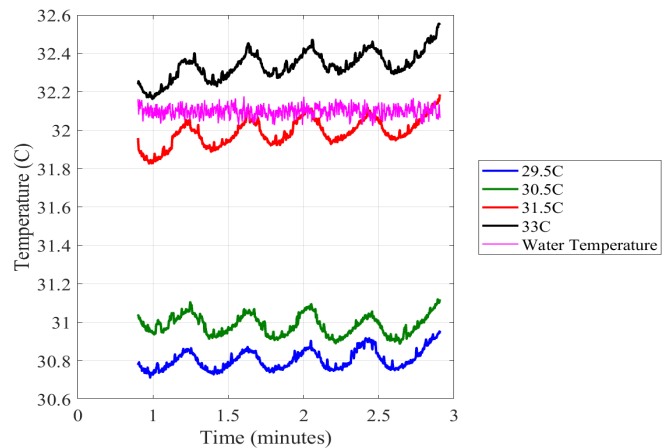


Figure 11. Temperature readings inside the polyurethane layer under one of the actuators at four different average temperatures of thermal stimuli and arm temperature simulated by hot water.

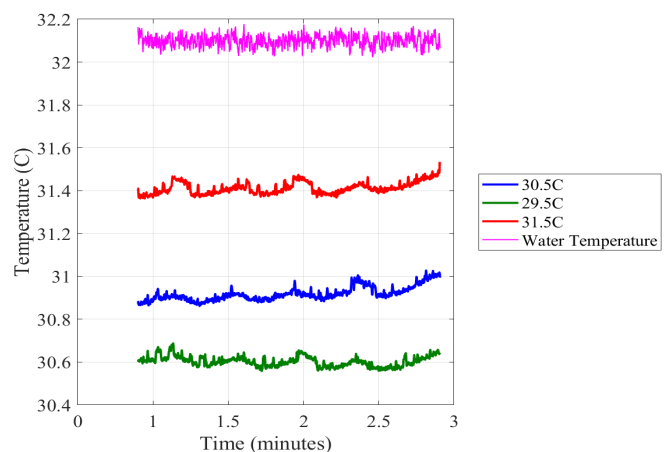


Figure 12. Temperature readings inside the polyurethane layer between the actuators at three different average temperatures of thermal stimuli and the temperature of arm provided by hot water.

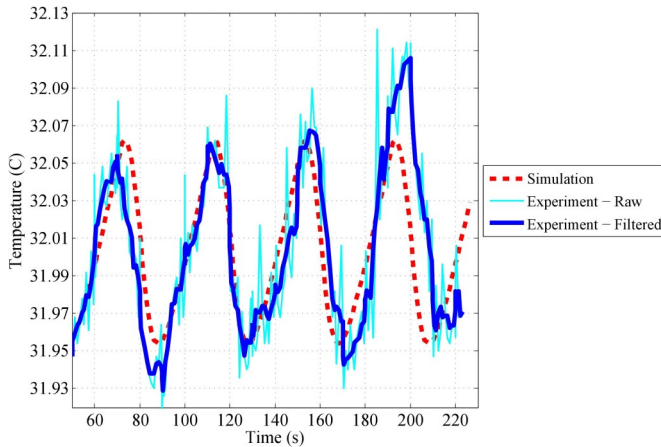


Figure 13. The temperature difference between the experiment and the simulation 1.6mm under an actuator.

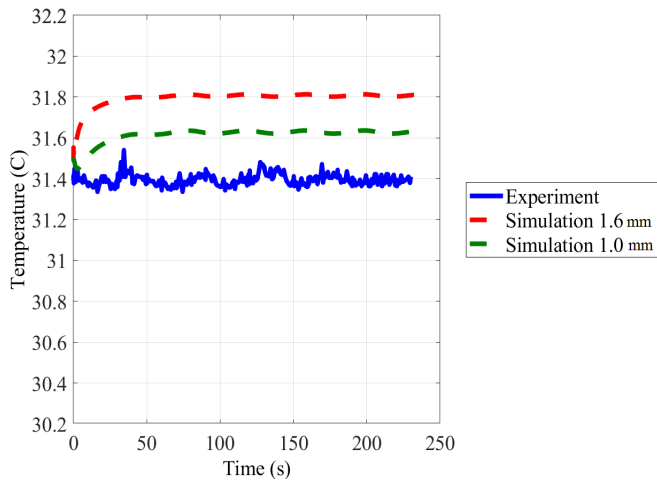


Figure 14. The temperature difference between the experiment and the simulation in the area between the actuators. The green and red dashed lines represent the upper and lower limits of the thermistor.

## Discussion

The simulation results showed that the average temperature on the surface of the skin remained at 31.5°C throughout the simulation, which suggests that there was no actual heating occurring on the skin and that the thermal display did not change the average temperature on the surface of the skin. Similar to the applied pattern, the readings under the actuators showed that the temperature was cooling quickly and warming slowly within 0.2°C (31.8-32°C), which is an indication that the effect of continuous cooling was still present at 1.0 mm under the surface of the polyurethane layer. Even though the effect of continuous cooling lost 80% of its efficiency in terms of temperature change amplitude, from 0.2 mm to 1.8 mm, as illustrated in Figure 9, these results indicate the intensity of this method of stimulation at different depths of the skin. It is worth mentioning

that hot and cold receptors are usually located between 0.2 mm and 0.5 mm under the skin (Adair, 1999; Ring, & de Dear, 1991), which suggests that the effect of the continuous cooling should be much higher.

The simulation results also showed that the temperature readings in the areas under and between the actuators increased as the depths of the temperature probes increased. In fact, the fluctuations of the readings tended to taper off as the probes came closer to the copper tube. Additionally, the temperature variation decreased between the actuators, which indicates that approximately 44.4% of the stimulation area did not perceive the continuous cooling effect that is associated with temperature change. However, the unstimulated area should not affect the overall sensation of continuous cooling. Studies have shown that the thermoreceptors are poor at discriminating between two spatially divided stimuli (Taus, Stevens, & Marks, 1975; Yang, Kwon, & Jones, 2009). Moreover, the previous continuous cooling study showed that participants perceived a steady and consistent sensation of cooling throughout the stimulation area (Kenshalo, 1976).

Furthermore, the model can be modified to study the effect of spatial summation. Studies have shown that the thermal threshold is inversely related to the area of stimulation (Kenshalo et al., 1967). However, this association is less distinct for the perception of cold (Greenspan & Kenshalo, 1985; Berg, 1979). The spatial summation can be further investigated with the model used in this study. The actuators' layout can produce a combination of different sizes and shapes of thermal stimulation to test warm and cold thresholds on areas between 2 cm<sup>2</sup> and 48.53 cm<sup>2</sup>. Moreover, the size of the actuators can be increased or decreased in a way that keeps the total area of stimulation constant in order to investigate the effect of spaces between the actuators and whether the thermal intensity changes. In contrast, the total area of stimulation can be increased by adding more actuators to the system to study the effect of the stimulation area on the temperature distribution and the overall perception of cold. This type of actuator can alternatively be replaced by a hot-and-cold liquid channel system to generate the same effect of continuous cooling. The simulated model will provide the ability to test the efficiency of such a system and whether it can be a possible replacement to the thermoelectric devices currently in use.

On the other hand, the results of the physical model showed differences in the temperature readings between the areas that are located under the actuators and the areas between the actuators, as illustrated in Figures 11 and 12. All of the temperature readings in the experiments were recorded using a 30/10-second heating/cooling rate with a diagonal pattern, as illustrated in Figure 7. The temperature under the actuators showed that the effect of continuous cooling is still present, even at 1.6 mm under the skin, whereas the temperature between the actuators remained constant with different stimuli temperatures.

---

The results of the physical experiments were very similar to the findings of the simulation model. Figure 13 best illustrates this similarity, where both results had the same behavior. Figure 14 shows a comparison between the temperatures of the model and the experiments, which shows that both temperatures were constant in the area between the actuators. However, there was an average difference of 0.3°C between the results. The comparison also showed subtle fluctuations in the temperature recorded from the experiments. These differences and fluctuations may have been caused by the possibility that the thermistor wires were directly exposed to the actuators. Due to the conductive nature of these wires, some temperature variations could have been conveyed to the probes, which led to the difference and fluctuation in the temperature. This problem can be avoided in the future by fully immersing the probes and the wires in the polyurethane sheet horizontally during the preparation process. The polyurethane layer should provide some insulation to the thermistor wires and connectors. Another way for insulation is to apply heat shrink tubing on the wires.

These differences may also have been caused by micro air bubbles formed during the process of making the polyurethane sheet during the curing process. Some of these air bubbles may have interfered with the readings of the probes, which explains why the temperature reading of the experiment in Figure 14 was 31.4°C. To minimize the likelihood of air bubbles forming in a polyurethane layer, the material can be heated before curing to release the excess air. A light vibration can also be applied to the mold before pouring the material to release air from it. Another suggestion to improve the results of the experiment is to add additional temperature sensors in the skin-like layer. The data acquisition device that was used to collect the temperatures had 16 analog inputs, 12 of which were allocated to controlling the thermal display device; hence, due to this limitation, it was not possible to add more than four sensors. This number was sufficient to record the temperature at different stimulation areas. However, more sensors would be needed to monitor more locations in the skin.

The results of the simulation gave some explanation of the efficiency of the proposed application and the intensity as well as the spatial distribution of temperature in the asymmetric cooling pattern. These results were also validated in the physical experiment that showed similar information about the temperature distribution inside the skin layer. These findings suggest that the simulation can be harnessed to analyze more advanced and technically challenging versions of this particular type of thermal display, such as adding more actuators and temperature probes to the system. Additionally, the simulation can be used to observe the thermal behavior of the skin layer when a continuous heating stimulus is applied. The continuous heating effect occurs when some actuators are slowly cooling, while others are quickly warming without causing a change in the average temperature of the skin. Modeling this type of thermal

stimuli will provide insight into temperature distribution inside the skin. Furthermore, knowing the temperature readings at different depths of the skin and the thermal conductivity of the skin will provide useful information about the heat flux that is transferred out of or into the skin. The model can calculate the heat flux that is transferred between the actuators and the skin, which is the driving factor of temperature perception. The calculated amount and direction of heat flux from the model can later be used to control the thermal actuators more accurately via a flux meter, instead of depending on temperature feedback.

## Conclusions

In this paper, the authors presented a simulation of an approximate model of the skin that was developed to investigate the thermal perception of the skin when asymmetrical hot and cold stimuli are applied. The results showed that the average surface temperature of the skin did not change during the thermal stimulation. The simulation also showed that the effect of the continuous cooling method was still present at depths up to 1.8 mm under the surface of the skin. A physical model was built and used to validate the simulation. The results of the physical experiments were similar to the findings of the simulation. It was shown that the simulation model could be utilized to predict the temperature and thermal behavior of the skin in different scenarios of this particular type of thermal stimuli.

## Acknowledgments

The authors would like to thank Nathan Crane for his input. This material is based upon work supported by the National Science Foundation under Grant Number IIS-1526475.

## References

- Adair, R. K. (1999). A model of the detection of warmth and cold by cutaneous sensors through effects on voltage-gated membrane channels. *Proceedings of the National Academy of Sciences*, 96(21), 11825-11829.
- ANSYS, Thermal Transient Analysis (2018), Release 18.1
- Berg, S. L. (1979). Magnitude estimates of spatial summation for conducted cool stimuli along with thermal fractionation and a case of secondary hyperalgesia. *Dissertation Abstracts International*, 39(11-B), 5605.
- Bergman, T. L., Incropera, F. P., DeWitt, D. P., & Lavine, A. S. (2011). *Fundamentals of heat and mass transfer*. John Wiley & Sons.
- Boetcher, S. K. S., Sparrow, E. M., & Dugay, M. V. (2009). Characteristics of direct-contact, skin-surface temperature sensors. *International Journal of Heat and Mass Transfer*, 52(15-16), 3799-3804.

- Cohen, M. L. (1977). Measurement of the thermal properties of human skin. A review. *Journal of investigative dermatology*, 69(3).
- Fiala, D., Lomas, K. J., & Stohrer, M. (2001). Computer prediction of human thermoregulatory and temperature responses to a wide range of environmental conditions. *International journal of biometeorology*, 45(3), 143-159.
- Greenspan, J. D., & Kenshalo, D. R. (1985). The primate as a model for the human temperature-sensing system: 2. Area of skin receiving thermal stimulation (spatial summation). *Somatosensory research*, 2(4), 315-324.
- Handbook, A., 2013. Fundamentals 2013. Atlanta, USA: ASHRAE.
- Ho, H. N., & Jones, L. A. (2005, March). Thermal model for hand-object interactions. In 2006 14th Symposium on Haptic Interfaces for Virtual Environment and Teleoperator Systems (pp. 461-467). IEEE.
- Hu, L., Gupta, A., Gore, J. P., & Xu, L. X. (2004). Effect of forced convection on the skin thermal expression of breast cancer. *Journal of biomechanical engineering*, 126(2), 204-211.
- Jones, L. A., & Ho, H. N. (2008). Warm or cool, large or small? The challenge of thermal displays. *IEEE Transactions on Haptics*, 1(1), 53-70.
- Kenshalo, D. R. (1976). *Correlations of temperature sensitivity in man and monkey, a first approximation*. In Sensory functions of the skin in primates (pp. 305-330). Pergamon.
- Kenshalo, D. R., Decker, T., & Hamilton, A. (1967). Spatial summation on the forehead, forearm, and back produced by radiant and conducted heat. *Journal of comparative and physiological psychology*, 63(3), 510.
- Manasrah, A., Crane, N., Guldiken, R., & Reed, K. B. (2016). Perceived cooling using asymmetrically-applied hot and cold stimuli. *IEEE Transactions on Haptics*, 10(1), 75-83.
- Manasrah, A., Crane, N., Guldiken, R., & Reed, K. B. (2017, June). Asymmetrically-applied hot and cold stimuli gives perception of constant heat. IEEE World Haptics Conference (WHC) (pp. 484-489).
- Materials Database - Thermal Properties. Thermtest Inc. Retrieved from [www.thermtest.com/materials-database#polyurethane](http://www.thermtest.com/materials-database#polyurethane)
- McKnight, P. T. (2010). *Finite element analysis of thermoelectric systems with applications in self assembly and haptics*. (Unpublished master's thesis). University of South Florida, Tampa, FL.
- Molinari, H. H., Greenspan, J. D., & Kenshalo, D. R. (1977). The effects of rate of temperature change and adapting temperature on thermal sensitivity. *Sensory processes*, 1(4), 354-362.
- Murakami, S., Kato, S., & Zeng, J. (2000). Combined simulation of airflow, radiation and moisture transport for heat release from a human body. *Building and environment*, 35(6), 489-500.
- Ring, J. W., & de Dear, R. (1991). Temperature transients: a model for heat diffusion through the skin, thermoreceptor response and thermal sensation. *Indoor Air*, 1(4), 448-456.
- Rugh, J. P., & Bharathan, D. (2005). Predicting human thermal comfort in automobiles. *SAE transactions*, 2508-2516.
- Rugh, J. P., Farrington, R. B., Bharathan, D., Vlahinos, A., Burke, R., Huizenga, C., & Zhang, H. (2004). Predicting human thermal comfort in a transient nonuniform thermal environment. *European journal of applied physiology*, 92(6), 721-727.
- Stevens, J. C. (1991). *Thermal Sensibility. The Psychology of Touch*. MA Heller and W. Schiff.
- Stevens, J. S. & Choo, K. K. (1998). Temperature sensitivity of the body surface over the life span. *Somatosensory & motor research*, 15(1), 13-28.
- Taus, R. H., Stevens, J. C., & Marks, L. E. (1975). Spatial localization of warmth. *Perception & Psychophysics*, 17(2), 194-196.
- Wang, Z., Li, Y., Kowk, Y. L., & Yeung, C. Y. (2002). Mathematical simulation of the perception of fabric thermal and moisture sensations. *Textile Research Journal*, 72(4), 327-334.
- Yang, G. H., Kwon, D. S., & Jones, L. A. (2009). Spatial acuity and summation on the hand: The role of thermal cues in material discrimination. *Perception & Psychophysics*, 71(1), 156-163.

## Biographies

**AHMAD A. MANASRAH** is an assistant professor of mechanical engineering at the Al Zaytoonah University of Jordan. He received his BS degree from Al Balqaa University, Amman, Jordan, and MS and PhD degrees from The University of South Florida, all in mechanical engineering. He was a research assistant and a member of the Rehabilitation Engineering and Electromechanical Design Lab at USF. He is also a member of the ASHRAE west coast program. His interests include thermal comfort, haptics, mechanical control, and education. Dr. Manasrah may be reached at [ahmad.mansrah@zuji.edu.jo](mailto:ahmad.mansrah@zuji.edu.jo)

**MEHDI HOJATMADANI** is a PhD student at the University of South Florida. He received his BS degree from Central-Tehran Azad University, Tehran, Iran, and his MS degree from Bogazici University, Istanbul, Turkey, all in mechanical engineering. He is currently a researcher at the REED Lab. His research interests include thermal haptics and how thermal stimulation is perceived, haptic memory (i.e., how sensory information from the haptic channel is retained and how it is different from other modalities), human-computer interaction, temperature-emotion relationships, and investigations into how temperature can influence affective measures. Mr. Hojatmadani may be reached at [mhojatmadani@mail.usf.edu](mailto:mhojatmadani@mail.usf.edu)

**RASIM GULDIKEN** was received his BS from the Middle East Technical University, Ankara, Turkey, in 2002,

---

MS degree from Northeastern University in 2004, and PhD from the Georgia Institute of Technology in 2008, all in mechanical engineering. He has been with the Mechanical Engineering Department at the University of South Florida first as an assistant professor (2008-2014) and currently as an associate professor. He also serves as the graduate program coordinator of the Mechanical Engineering Department at USF. His research interests include micro and nano acoustic and thermal sensors and microfluidics. He is the 2018-2019 Chair of the ASME Microelectromechanical Systems (MEMS) Division, member of National Academy of Inventors, and has four U.S. issued patents as an inventor. Dr. Guldiken was a recipient of the Society of Automotive Engineers (SAE) Ralph Teetor Educational Award, American Society of Mechanical Engineers (ASME) Florida West Coast Engineer of the Year, and USF University Wide Outstanding Undergraduate Teaching Award. Dr. Guldiken may be reached at [guldiken@usf.edu](mailto:guldiken@usf.edu)

**KYLE B. REED** is an associate professor in the Department of Mechanical Engineering at USF. Dr. Reed's research interests include rehabilitation and haptics. His research on haptics focuses on thermal responses of the skin, coordinated motions, and human-robot interaction. His rehabilitation research focuses on restoring abilities in individuals with asymmetric impairments, such as from a stroke or unilateral amputations. He has received funding from the National Science Foundation, the National Institutes of Health, the Florida High Tech Corridor, the Orthotic and Prosthetic Education and Research Foundation, the American Orthotic & Prosthetic Association, and industry. He is an Associate Editor for IEEE Transactions on Haptics. Prior to USF, he was a post-doctoral scholar at Johns Hopkins University. He received his PhD and Masters from Northwestern University and his BS from the University of Tennessee, all in mechanical engineering. He is a Senior Member of the Institute of Electrical and Electronics Engineers (IEEE) and a Senior Member of the National Academy of Inventors (NAI). Dr. Reed may be reached at [kylereed@usf.edu](mailto:kylereed@usf.edu)

# CORRELATING FIELD TO LABORATORY COMPACTION FOR ROLLER-COMPACTED CONCRETE

Tamer M. Breakah, Ball State University; Mohamed Nagib Abou-Zeid, The American University in Cairo; Mohamed El-Saied, The American University in Cairo; Kamel Elamrousy, The American University in Cairo; Ahmed Hamed, The American University in Cairo; Elmohanad Elsayad, The American University in Cairo; Fadi Abdallah, The American University in Cairo

## Abstract

Since there is a new shift in the Egyptian construction industry towards roller-compacted concrete (RCC) for the construction of Egyptian roads, it has become essential to investigate RCC's engineering properties. The economic studies in Egypt favour RCC construction more than asphalt cement concrete in terms of abundance and price. Thus, RCC has been newly introduced in the Egyptian market for excessive use in road and highway construction. In light of this trend, the authors looked for a correlation between the field and laboratory compressive strengths of RCC. This research focused mainly on selecting the laboratory compaction method in addition to the compaction effort needed to achieve a compressive strength in the laboratory equal to that achieved in the field. A small RCC strip was constructed to extract cores from and compare the results to those achieved by laboratory compaction using Proctor, Modified Proctor and vibrating-table compaction methods. For each method, five compaction analyses were made.

The results showed that the vibrating table tends to overestimate the compressive strength. On the other hand, in the case of Proctor compaction, 12 blows and 16 blows are needed to resemble 8 and 10 roller passes on site, respectively. In the case of the Modified Proctor compaction method, the samples need to be compacted by applying 13 blows to resemble 10 roller passes on site. This method does not provide similar results to the 8 roller passes. Further research is needed with different mixtures and field compaction efforts to be able to find a correlation.

## Introduction

In Egypt, most roads are constructed using asphalt cement concrete. Recently, with the increase in demand for asphalt cement, due to the ongoing construction of thousands of kilometers of roads in Egypt, there is a shift towards the use of rigid pavements. Another reason that made Egypt shift towards the use of rigid pavement is that asphalt modification is not yet included within the Egyptian code of practice, and Superpave methodology has not yet been implemented, and several research studies indicate that asphalt cement produced in Egypt does not meet the performance grade required for the Egyptian climate. The combination of economic and technical reasons led to the shift in Egypt towards the use of rigid pavements. With the shift towards

the use of rigid pavements and the availability of asphalt concrete paving equipment, roller-compacted concrete (RCC) appears to be a good alternative for use in Egypt. RCC is stiff concrete with a very low water-to-cement ratio that has the same constituents as conventional concrete and is constructed by using a deadweight or vibrating-roller compactor. RCC is constructed using the same equipment used in asphalt concrete, and has very high productivity compared to typical rigid pavements.

Today, RCC remains one of the leading alternatives in the construction industry, due to its diverse applicability, ease of installation, and unique qualities, the most important being economy, strength, durability, and convenience. The RCC compaction effort can be decided upon by choosing target density for field compaction, as in soil cement and asphalt cement concrete. A major difference between RCC and asphalt cement concrete is that the latter continues to consolidate after construction (White, 1986). A major issue in the design of RCC is the relationship between field compaction and laboratory compaction. The main objectives of this current research were to investigate different laboratory compaction techniques, compare them to field results, and to recommend a compaction effort that can be applied in the laboratory.

## Background

Roller-compacted concrete is made using a zero-slump mix and is compacted using a vibrating compactor (Bilý, Fládr, & Haase, 2015). It can be considered as a transitional material that inherits technologies from Portland cement concrete, soil cement, and asphalt cement concrete (White, 1986). RCC has advantages in durability and cost as an alternative to be used in heavy-duty pavements subjected to low traffic speeds (Amer, Delatte, & Storey, 2003). RCC was used successfully in many heavy-duty projects such as ports, weigh stations, and warehouses. The use of roller-compacted concrete has been around since the late 1970s. The use of RCC has steadily increased in recent years in public and private uses and especially in the cases of low-volume parking areas (Pittman & Anderton, 2009). More than 100 roller-compacted concrete pavements were constructed in North America during a period of 24 years (Amer et al., 2003). It also managed to attract the US Army Corps of Engineers (USACE), who started making use of RCC pavements throughout various military facilities in the US in 1980. USACE used RCC in heavy-duty applications such as equipment hardstands and tank test roads (Amer et

---

al., 2003). Pittman and Anderton (2009) tested sections of RCC that were constructed at the Army Corp of Engineers Waterways Experiment Station in Vicksburg, Mississippi in 1975. In 1984, a tank hardstand military application was constructed at Fort Hood, Texas, which is considered the first large-scale project. Around 1988, there was a significant increase in the areas constructed using RCC in the US, which exceeded 2.5 million square yards. These projects were mainly in the military and private/industrial sectors. There was no significant increase in the use of RCC until around 2000. After this, there was a significant increase in the use of RCC in the US. The area constructed using RCC reached more than 9.5 million square yards in 2008, and most of it was in the private/industrial sector (Pittman & Anderton, 2009).

RCC mixes are dry concrete mixes that have the same constituents of concrete but with different proportions. Compaction of concrete, in addition to cement hydration, is a major factor in the strength of RCC, due to RCC's dependency on aggregate interlock (Chhorn & Lee, 2017). RCC can achieve strengths that are equal to or higher than those achieved in conventional concrete. This depends on several factors such as using well-graded aggregates, properly selecting the cement and water contents, and good compaction of the concrete mixture. The amount of water needs to be properly selected, as these mixes should be stiff enough to withstand the vibratory rollers, and wet enough to allow distribution of paste, while mixing without segregation (Chhorn & Lee, 2017).

RCC has several advantages and this makes it more feasible for some pavement structures (Bilý et al., 2015). The advantages of RCC include being fast and economical in construction. This makes it a good alternative for many applications. It has been typically used for pavements subjected to heavy loads and low speeds, because of its coarse surface. Recently, there had been an increase in its use in highways, local streets, and commercial areas. Due to the nature of pavement, occasional light traffic is allowed in the first few days (Harrington, Abdo, Adaska, Hazaree, Ceylan, & Bektas, 2010). RCC's compressive strength ranges typically between 28 and 41 MPa, which is within the same range of conventional concrete. A strength of 48 MPa was achieved in some projects (Harrington et al., 2010). RCC has lower paste content compared to conventional concrete, which makes it more attractive from an environmental point of view because of the reduced cement content. Ease of construction and the elimination of the need for formwork and finishing are other advantages that make RCC attractive for use in projects (Chhorn & Lee, 2017). RCC pavements have a major limitation due to surface smoothness, which makes them less preferred for high-speed roads (Bilý et al., 2015).

The mixture design inherits its procedure from soil mechanics (Chhorn & Lee, 2017; Harrington et al., 2010). In the design process, trials are made at different cementitious

contents and for each one of them, samples are compacted at different water contents using the modified Proctor method. When using a weak aggregate, the Proctor method is recommended instead. The different water contents are used to find the optimum water content that will yield the highest density (Harrington et al., 2010; Tayabji et al., 1995). The moisture content is a function of the aggregate and cement used. An increase or decrease in the water content from the optimum value will affect the strength of RCC (Tayabji et al., 1995). In general, the percentage of aggregate in the mix is higher than conventional concrete (Harrington et al., 2010). Production of laboratory specimens that give an indication of field properties is one of the drawbacks of RCC (Amer et al., 2003; Trtík, Chylík, Bilý, & Fládr, 2017). Sample preparation is different from that of conventional concrete. Compaction is the governing factor that affects RCC properties. According to ASTM Standard C1435 "Molding Roller-Compacted Concrete in Cylinder Molds Using a Vibrating Hammer" and ASTM standard C1176 "Standard Practice for Making Roller Compacted Concrete in Cylinder Molds using a Vibrating Table", RCC specimens are prepared for compressive strength testing using a vibrating hammer or vibrating table. The samples prepared in the laboratory might have significantly different properties than the field-compacted concrete, due to the difference in compaction; thus, samples cored from the field are preferred (Khayat & Libre, 2014).

Amer et al. (2003) investigated the use of the gyratory compactor, which is commonly used with asphalt cement concrete under the Superpave method, as a compaction technique. The asphalt industry started using the gyratory compactor, as it mimics the effect of roller compaction in the field. The use of the gyratory compactor to prepare RCC samples yielded consistent results, when it came to strength and density, and the results were in agreement with field-procured samples. The authors concluded that the number of gyrations depends on the field compaction level; but for their studied samples, 60 gyrations replicated accurately the field conditions (Amer et al., 2003). In another study, LaHucik and Roesler (2017) studied the variability in field density with depth. They found that the pavement that achieved the specified density of 98% of Modified Proctor optimum density from the design was the 12.7-cm-thick pavement. To achieve 98% of the Modified Proctor density in the laboratory, a gyratory compactor was used and the samples required 50 to 70 gyrations to achieve 98% of the Modified Proctor (LaHucik, & Roesler, 2017). There was a statistical difference between laboratory-prepared samples and those cored from the field. They attributed the difference to the 4% reduction in density, which led to 45% reduction in compressive strength. The laboratory-prepared samples achieved the designated 28-day compressive strength at 7-day testing. On the other hand, field samples from two of the four projects studied did not achieve the desired 28-day strength (LaHucik, & Roesler, 2017). Bilý et al. (2015) studied properties of RCC and found high variability in the results, as they used manual compaction.

Trtík et al. (2017) compacted samples using a pneumatic hammer and by static compaction. These samples were compared to cores taken from RCC pavement based on bulk density and compressive strength. The results from the pneumatic hammer with a compaction period of 10s resembled the field conditions. The results of static loading were significantly different from those compacted using the pneumatic hammer. This indicates that production of RCC pavements by static compaction is not appropriate (Trtík et al., 2017).

## Objective

The main objective of this current study was to perform a pilot study in order to correlate field compressive strength to that of laboratory-prepared samples. This was done by compacting a test strip on a construction site and using the same concrete mix; the samples were compacted in the laboratory using different equipment and different compaction efforts in order to find the combination that resembled the field results.

## Methodology

In order to evaluate the laboratory compaction method and compare it to field compaction, a small field-compact strip was constructed in order to be able to extract cores from it and compare them to laboratory-compact samples using different compaction techniques.

## Mix Design

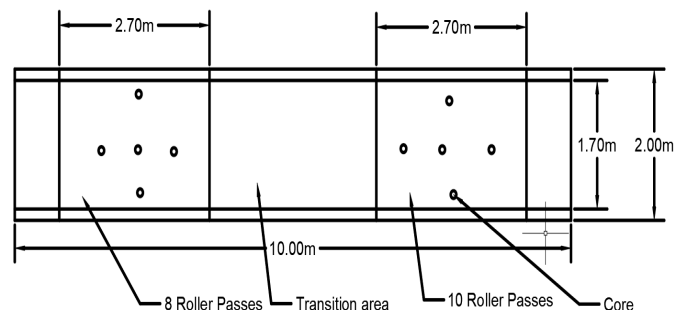
The mixture design used in this study contained 472.5 kg/m<sup>3</sup> cement, 170 kg/m<sup>3</sup> water, 666.5 kg/m<sup>3</sup> fine aggregate, and 1087 kg/m<sup>3</sup> coarse aggregate with a water-to-cement ratio of 0.32. This mix design was used for both the laboratory and field work.

## Field-Compacted Strip

A site was selected to construct a 2m-wide and 10m-long strip. The main purpose of this strip was to get cores that were field-compact for testing. The thickness of the pavement section was 15 cm. The results from the cores were used to compare to results from the laboratory-prepared samples using the same mix. The strip was divided into two segments with a different number of passes by the roller compactor as follows:

- (a) Segment 1 (2.7m x 2m) was subjected to 8 passes by the compactor.
- (b) Segment 2 (2.7m x 2m) was subjected to 10 passes by the compactor.
- (c) The rest of the strip was used for compactor manoeuvres.

The strip was paved over the natural subgrade after properly compacting the subgrade using an eight-ton roller compactor. The width of the strip was limited to 2m, which was the width of the compactor used. The strip was cured for seven days and then the samples were cored from the strip and taken to the laboratory for further curing and testing. For each segment, five cores were taken; two near the pavement edge (one near each edge) and three close to the pavement centerline. Figure 1 shows coring of field samples and a schematic of their location. It is worth noting that for a concrete mixing crew that has never worked with RCC, the mix was considered a very dry mix and they wanted the researchers to change the mix design. This implies that with the introduction of RCC in areas in which it was never previously implemented, awareness sessions would be necessary. On the other hand, for the placement and compaction team, who worked mainly with flexible pavements, the experience was simple and familiar.



(a) Schematic of the strip and core locations.



(b) Core Extraction.

Figure 1. Sample locations and core extraction.

## Laboratory Sample Preparation

To achieve the research objective of finding a suitable compaction method that replicates field results, three compaction methods were used in the laboratory. Two of these methods were soil-compaction methods, while the third one was the standard method used in RCC compaction. The three selected compaction methods were Proctor compaction (ASTM D698), Modified Proctor compaction (ASTM D1557), and Vibrating-table compaction (ASTM C1176). For each method, five compaction efforts were used in order to find out which compaction effort best resembled field compaction. For the Proctor and Modified Proctor compaction methods, the number of blows was varied. On the other hand, for the vibrating-table compaction method, the vibration time was varied. This was done because, in the vibrating table, level of compaction is a function of time. Figure 2 shows the details of the compaction methods and the different compaction efforts. Nine replicates were compacted at each compaction level.

The samples at each compaction effort were randomly divided into three groups to be tested at 7, 14, and 28 days, with three replicates in each group. The densities of the samples were calculated and the samples were then tested for compressive strength. In order to eliminate the effect of sample size as a difference between the laboratory-produced samples and the field-produced samples, the samples were made to be 10 cm in diameters and 13 cm high, to replicate the size of the samples cored from the field section.

The compaction procedure followed ASTM standards as follows:

- Proctor Compaction method followed ASTM D698: Standard Test Methods for Laboratory Compaction Characteristics of Soil Using Standard Effort (12,400 ft-lbf/ft<sup>3</sup> (600 kN-m/m<sup>3</sup>))
- Modified Proctor compaction method followed ASTM D1557: Standard Test Methods for Laboratory Compaction Characteristics of Soil Using Modified Effort (56,000 ft-lbf/ft<sup>3</sup> (2,700 kN-m/m<sup>3</sup>))

- Vibrating Table Compaction Method followed ASTM C1176: Standard Practice for Making Roller-Compacted Concrete in Cylinder Molds Using a Vibrating Table

## Results and Analysis

Figure 3 and Table 1 show the results of the field-compacted laboratory-tested cores. It can be determined from the results that there was a reduction in the strength of the samples extracted near the edge of the pavement, as compared to those extracted near the centerline. The reduction in strength was about 3% in the case of applying 8 passes by the compactor, and 6% in the case of applying 10 passes by the compactor. It can be also concluded from the results that the RCC samples gained more than 70% of their strength after 14 days. Table 2 presents a summary of the laboratory results.

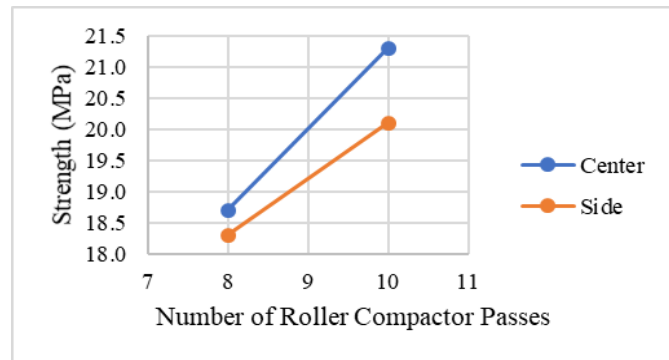


Figure 3. Compressive strength results for field cores.

The results of the Proctor and Modified Proctor tests at 7, 14, and 28 days show a trend of increasing strength until a peak strength is achieved, at which point the strength starts to decline. This indicates that over compaction of RCC might have an adverse effect. As expected, due to the increased compaction effort, the strength achieved by the Modified Proctor test was higher than that achieved by the Proctor test. Figures 4-6 shows the results of the Proctor and Modified Proctor tests.

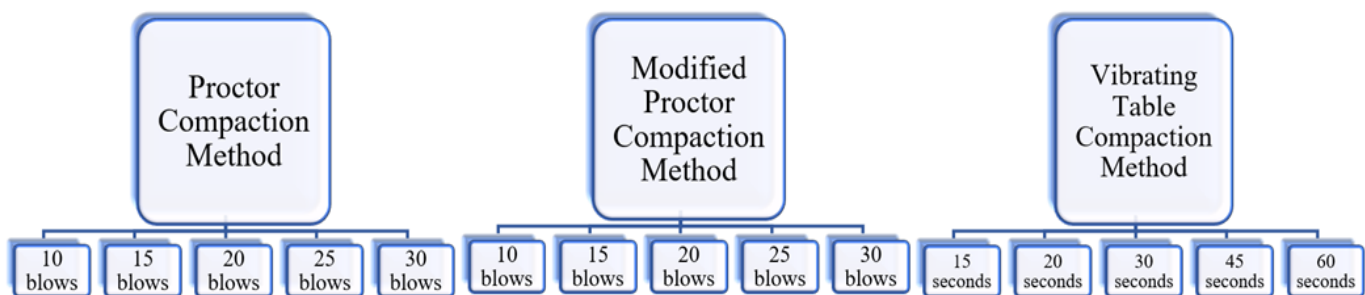


Figure 2. Laboratory experimental program.

Table 1. Results of samples cored from the pavement strip.

Number of Roller Passes	Sample Location	Sample Age (Days)	Strength (MPa)	Mean Strength (MPa)	Strength Standard Deviation (MPa)	Density (kg/m <sup>3</sup> )	Mean Density (kg/m <sup>3</sup> )	Density Standard Deviation (kg/m <sup>3</sup> )
8	Center	14	13.1	13.1	N/A	2278	2278	N/A
8	Center	28	18.4	18.7	0.4	2300	2236	91.2
8	Center	28	19.0	2171				
8	Side	28	18.1	18.3	0.3	2274	2249	353.6
8	Side	28	18.5	2224				
10	Center	14	17.6	17.6	N/A	2245	2245	N/A
10	Center	28	21.1	21.3	0.2	2296	2313	24.0
10	Center	28	21.4	2330				
10	Side	28	20.4	20.1	0.4	2321	2306	21.2
10	Side	28	19.8	2291				

Table 2. Properties of Laboratory Prepared Samples.

Sample ID	Strength (MPa)			Density (kg/m <sup>3</sup> )		
	7 Days	14 Days	28 Days	7 Days	14 Days	28 Days
Proctor 10	15.3	18.3	20.2	2463	2452	2484
Proctor 15	16.4	19.7	21.7	2580	2613	2648
Proctor 20	18.5	22.2	23.8	2503	2628	2617
Proctor 25	24.7	29.6	32.5	2548	2572	2502
Proctor 30	22.9	27.2	28.3	2598	2576	2662
Modified Proctor 10	12.9	15.6	17.2	2447	2397	2405
Modified proctor 15	22.4	20	22	2404	2398	2464
Modified Proctor 20	25.1	24	26.4	2513	2468	2425
Modified Proctor 25	28.1	33.7	37	2295	2230	2267
Modified Proctor 30	23.9	27.7	31.2	2477	2477	2432
Vibrating Table 15	20.6	24.8	27.2	2356	2294	2304
Vibrating Table 20	22.7	27.2	29.9	2366	2336	2265
Vibrating Table 30	29	34.8	38.3	2367	2322	2464
Vibrating Table 45	29.4	35.3	38.8	2323	2421	2360
Vibrating Table 60	30.8	37	40.7	2350	2333	2312

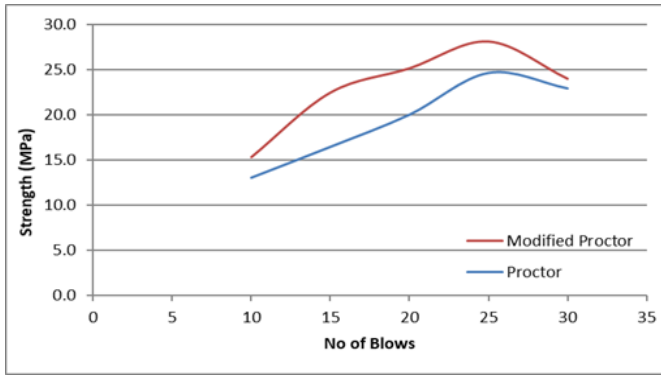


Figure 4. 7-day compressive strength for samples compacted using Proctor and Modified Proctor.

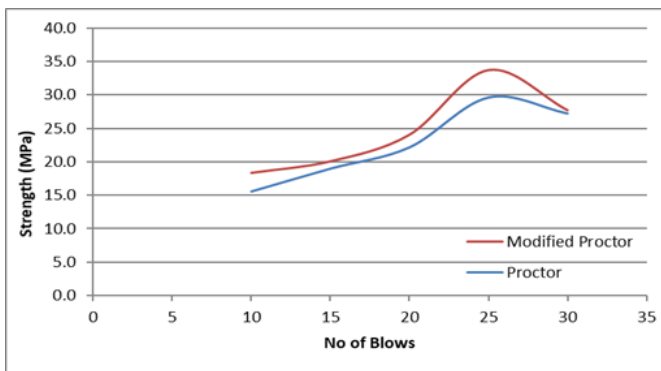


Figure 5. 14-day compressive strength for samples compacted using Proctor and Modified Proctor.

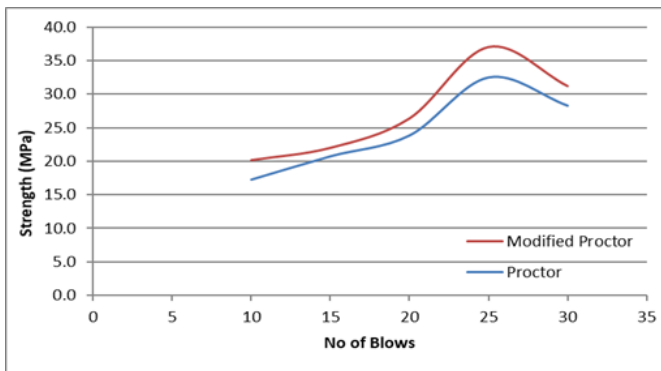


Figure 6. 28-day compressive strength for samples compacted using Proctor and Modified Proctor.

## Vibrating Table

Figure 7 shows the results of the vibrating-table test at different ages. It can be concluded from the results that compaction above 30 seconds had a negligible effect on the compressive strength of the samples.

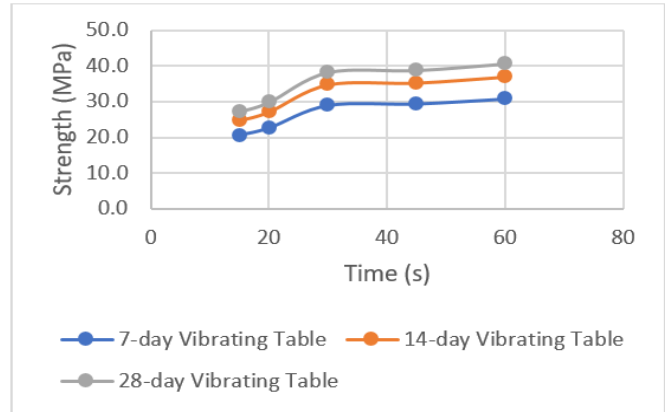


Figure 7. Compressive strength for samples compacted using Vibrating Table.

## Selection of the Representative Compaction Method

The main purpose of this study was to find the compaction method that resembles field compaction and to determine the appropriate compaction effort that will yield the same results in the field and the laboratory. Figure 8 summarizes the results achieved from field and laboratory samples at an age of 28 days. The intersection between the resulting field and laboratory curves was taken as the recommended compaction effort. It can be concluded from Figure 8 that the vibrating table overestimates the strength of RCC and is not capable of predicting the field results. On the other hand, Proctor and Modified Proctor compaction methods showed promising results. The Modified Proctor test was not able to capture the compressive strength of the 8 roller passes field compaction. To be able to simulate the 8 roller passes field compaction, it is recommended to compact the samples in the lab using the Proctor compaction method and apply 12 blows. In order to simulate the 10 roller passes field compaction, it is recommended to compact the samples in the lab using the Proctor compaction method and apply 16 blows, or use the Modified Proctor compaction method and apply 13 blows. Density was not included in this analysis, as the results did not follow any specific trend.

## Conclusions

In this paper, the authors present a pilot study that investigated the correlation between different laboratory compaction methods and field compaction in roller-compacted concrete. The main point of the investigation was to determine the compressive strength and find out which method would achieve the same compressive strength as the field-compacted strip. This study should be repeated under different conditions, mixes, and compaction efforts. Based on the field-compacted strip, laboratory conditions, and the range of materials used, the following can be concluded:

- The Proctor and Modified Proctor curves reached a peak strength at 25 blows. This indicates that over compaction might lead to loss of RCC compressive strength.
- Vibrating table reached a plateau after 30 seconds for all the sample ages tested. This indicates that compaction for more than 30 seconds using the vibrating table is not beneficial.
- Compared to the field results obtained, the vibrating table tends to overestimate the compressive strength of roller-compacted concrete.
- The core extracted from the sides yielded less strength than the those extracted from the center of the constructed lane.
- Awareness is needed about RCC properties and mixes when it is implemented in new locations, due to its unique nature.
- The placement and compaction process was familiar to a crew that is used to working with flexible pavements.
- The correlation between laboratory and field results indicates that Proctor and Modified Proctor methods better resemble the field compressive strength.

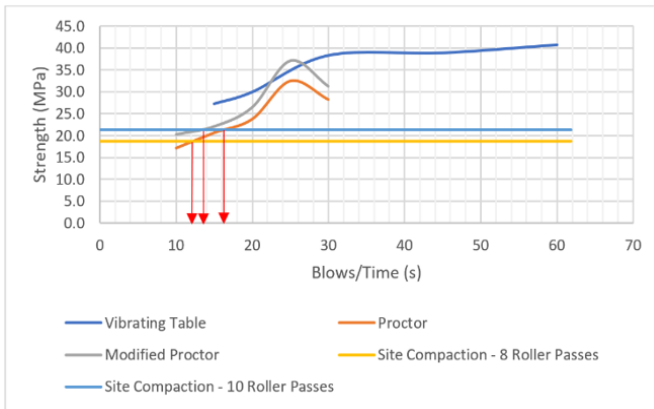


Figure 8. Combined 28-day strength results.

## Recommendations

1. To achieve laboratory compressive strength, it is recommended to use Proctor or Modified Proctor compaction methods.
2. Samples compacted using the Proctor compaction method need to be compacted by applying 12 blows and 16 blows to resemble 8 and 10 roller passes on site, respectively.
3. Samples compacted using the Modified Proctor compaction method need to be compacted by applying 13 blows to resemble 10 roller passes on site. This method does not resemble 8 roller passes.
4. The use of the vibrating table in compacting laboratory samples is not recommended, as it yields signifi-

cantly higher compressive strength compared to field-compacted samples.

5. This study only investigated the presence of the correlation. Further studies are needed to get more details that relate to the changes in mix designs and different field-compaction levels. This study had also limited data points; thus, it is recommended to have more samples in order to be able to verify the recommended laboratory-compaction levels and perform a statistical analysis.
6. Properties other than compressive strength need to be studied.

## References

- Amer, N., Delatte, N., & Storey, C. (2003). Using Gyrotory Compaction to Investigate Density and Mechanical Properties of RCC. *Journal of the Transportation Research Board*, 1834, 1-7.
- Bilý, P., Fládr, J., & Haase, M. (2015). Experimental verification of properties of roller-compacted concrete for pavements. *Advanced Materials Research*, 1124, 307-312.
- Chhorn, C., & Lee, S. W. (2017). Consistency control of roller-compacted concrete for pavement. *KSCE Journal of Civil Engineering*, 21(5), 1757-1763.
- Harrington, D., Abdo, F., Adaska, W., Hazaree, C. V., Ceylan, H., & Bektas, F. (2010). *Guide for roller-compacted concrete pavements*. (No. INTRANS102). Iowa State University. Institute for Transportation.
- Khayat, K. H., & Libre, P. N. A. (2014). *Roller-compacted concrete: field evaluation and mixture optimization* (No. NUTC R363). Missouri University of Science and Technology. Center for Transportation Infrastructure and Safety.
- LaHucik, J., & Roesler, J. (2017). Field and Laboratory Properties of Roller-Compacted Concrete Pavements. *Transportation Research Record: Journal of the Transportation Research Board*, 2630, 33-40.
- Pittman, D. W., & Anderton, G. L. (2009). *The use of roller-compacted concrete (RCC) pavements in the United States*. Paper presented at the Sixth International Conference on Maintenance and Rehabilitation of Pavements and Technological Control (MAIREPAV6), Turin, Italy, July 8-10.
- Tayabji, S. D., Sherman, T. W., Keifer, O., Nanni, A., Piggott, R. W., Pittman, D.,...Scott, J. A. (1995). *State-of-the-Art Report on Roller-compacted Concrete Pavements* (No. ACI325. 10R-95).
- Trtík, T., Chylík, R., Bilý, P., & Fládr, J. (2017), September. Analysis of laboratory compaction methods of roller-compacted concrete. In *IOP Conference Series: Materials Science and Engineering*, 236(1). IOP Publishing.
- White, T. D. (1986). Mix Design, Thickness Design, and Construction of Roller-Compacted Concrete Pavement. *Transportation Research Record*, 1062, 1-6.

---

## Biographies

**TAMER BREAKAH** is an assistant professor of construction management at Ball State University. He earned his BS and MS degrees in construction engineering in 2001 and 2006, respectively, from the American University in Cairo, Egypt. He earned his PhD in civil engineering in 2009 from Iowa State University. Dr. Breakah is currently teaching at Ball State University. His research interests include construction materials, sustainable materials, and lifecycle costing. Dr. Breakah may be reached at [tmbreakah@bsu.edu](mailto:tmbreakah@bsu.edu)

**MOHAMED NAGIB ABOU-ZEID** is a professor and former chair of the Construction Engineering Department and former Dean of Sciences and Engineering at the American University in Cairo. He has more than 200 peer-reviewed publications. His research interests include sustainability, construction materials, and repair of structures. Dr. Abou-Zeid may be reached at [mnagiba@aucegypt.edu](mailto:mnagiba@aucegypt.edu)

**MOHAMED EL-SAIED** is a civil engineer at Vinci Construction Grands Projects, currently working in the construction of “Cairo Metro Line 3 Phase 3”. He earned his BS in Construction Engineering in 2016 from the American University in Cairo. His research interests include underground construction and mega water projects. Mr. El-Saied may be reached at [mohamed\\_92@aucegypt.edu](mailto:mohamed_92@aucegypt.edu)

**KAMEL ELAMROUSY** is an assistant project manager at GHD Abu Dhabi, Australian Design and Project Management Consultant. He earned his BS in Construction Engineering in 2016 from the American University in Cairo, and MSc in Construction Management in 2017 from the University of Reading, UK. Besides working in the construction industry, Kamel is currently working on several joint research papers related to project management. Kamel may be reached at [elamrousy@aucegypt.edu](mailto:elamrousy@aucegypt.edu)

**AHMED HAMED** is a technical sales engineer at CEMEX Egypt, a global leader in the building materials industry. He earned his BS in Construction Engineering in 2016 from the American University in Cairo. His research interests include construction materials, alternative fuels, and green cement technology. Ahmed may be reached at [reda999@aucegypt.edu](mailto:reda999@aucegypt.edu)

**ELMOHANAD ELSAYAD** is a project manager at Permasteelisa North America. He earned his BSc in Construction Engineering from the American University in Cairo and a Master’s degree in Development Practice from the University of Minnesota. Elmohanad’s research interests include sustainable materials, architectural envelopes, and façade construction/curtain-walls. Mr. Elsayad may be reached at [elsay021@umn.edu](mailto:elsay021@umn.edu)

**FADI ABDALLAH** is a construction engineer. He earned his BSc in Construction Engineering from the American University in Cairo. Mr. Abdallah may be reached at [fadiabdalla@aucegypt.edu](mailto:fadiabdalla@aucegypt.edu)

# AN AUTOMATED HYDRAULIC POSITION CONTROL SYSTEM: STRUCTURE AND PERFORMANCE ANALYSIS

Yuqiu You, Ohio University; Jesus Pagan, Ohio University

## Abstract

Hydraulic systems are widely used in industry, since they can produce large torques, high-speed responses with rapid motions and speed reversals. Automatic control of hydraulic systems has evolved into an increasingly superior alternative for many industrial applications. Advances in hydraulic hardware and electronics have combined to make the design and implementation of these systems more intuitive, reliable, cost effective, repeatable, and user friendly. Controlling the position of a cylinder is one of the most demanding hydraulic motion control applications. The project illustrated in this paper is a study of automated position control of a hydraulic cylinder through a Parker Compax3F fluid controller (Parker Hannifin Corporation, 2007). The authors introduce the hardware components, structure, programming, configuration, and performance analysis of the automated hydraulic position control system.

## Introduction

Automatic control of hydraulic systems has evolved into an increasingly superior alternative for many industrial applications. Controlling the position of a hydraulic cylinder is one of the most demanding motion control applications. The project presented here demonstrates the design, structure, development, and performance analysis of an automated hydraulic position control system. This automated hydraulic position control system was designed to control the linear-motion position of a hydraulic cylinder through a touch screen HMI (Human-Machine Interface). The major components of the system include a Parker 3L hydraulic cylinder, a position sensor, a DF Plus electrohydraulic servo valve, a PID controller, a Compax3F fluid controller, a touch screen HMI display, and an H-Pack hydraulic power supply. The control method applied was a traditional PID (proportional, integral, and derivative) control. As most classical approaches for positioning of hydraulic cylinders, the system did not give satisfactory performance, due to the major dead-zone problem. In this study, the system performance was compensated for through hardware configuration and CODESYS programming of the controller. The resulting performance improvement was verified through performance analysis.

## System Overview

The hydraulic position control system consists of a hydraulic cylinder, a proportional valve, a position sensor, a fluid controller, and an HMI touch screen. Table 1 list the

specifications of these major hardware components. Figure 1 illustrates the layout of the system. Figures 2 and 3 show the cylinder with position motion and proportional valve.

Table 1. List of hardware components.

Part Name	Component Type	Part Number
Compax3F	Hydraulics controller	C3F001D2F12 I11 T30 M00
DF Plus valve	Proportional directional control valve	D1FPE50FB9NB00 20
Parker 3L cylinder	Hydraulic cylinder	01.50 F3LLUS23A 12.000
Parker H-Pak	Hydraulic power supply	H1B2 7T10P0X13909/13
Parker HMI	HMI display	XPR06VT-2P3

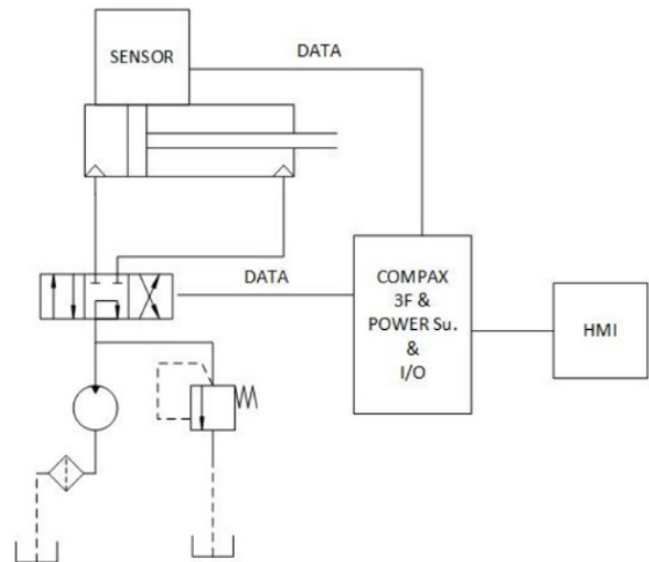


Figure 1. System layout and major components.

The system uses Parker's Compax3F fluid controller as the main controller. Compax3F is a servo drive for position, velocity, and force/pressure control of electrohydraulic systems. This controller is a programmable motion control device based on IEC61131. IEC61131 is an international electro-technical commission standard for programmable controllers. Compax3F is programmed by CODESYS, an IEC61131-based program development platform. The DF Plus valve from Parker is used as the proportional directional

control valve for this system. The proportional directional control valve controls the position of the cylinder, based on DC signals ranging from -10v to +10v. A linear variable differential transformer (LVDT) provides position feedback to validate the cylinder position for improved accuracy and repeatability. The LVDT generates a feedback voltage proportional to the position change of the cylinder. The feedback voltage is then used by the controller to determine the control variable of the system.

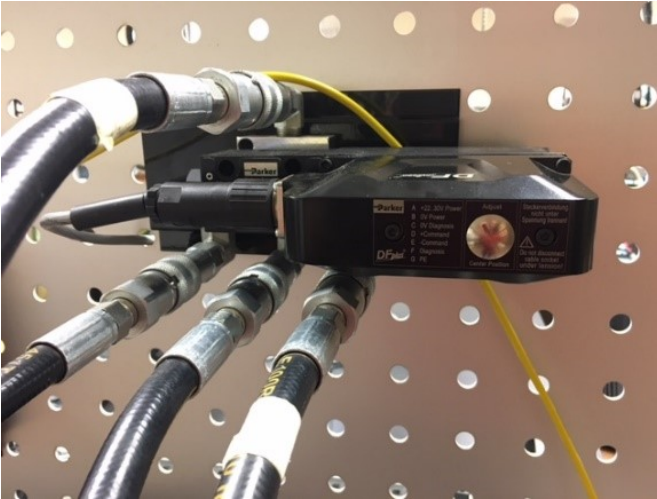


Figure 2. The DF Plus proportional valve.

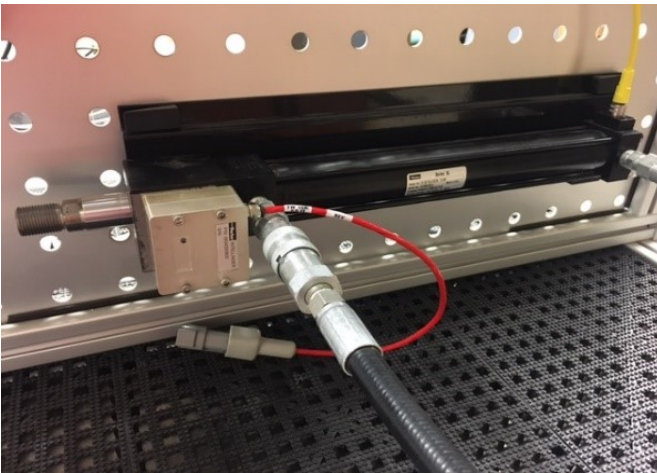
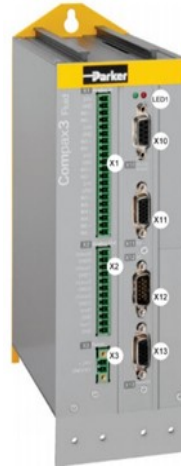


Figure 3. The linear cylinder with the position sensor.

## Compax3F Controller Configuration and Programming

Compax3F is a programmable hydraulics controller that interfaces with various input and output devices and implements control functions. Figure 4 shows that the controller has modules that can connect to six analog input devices, four analog output devices, and twelve digital input/output signals.



X1	Analog Inputs
X2	Analog Outputs
X3	24 VDC power supply
X10	RS232/RS485
X11	2. Feedback Type
X12	Inputs/Outputs
X13	1. Feedback Type

Figure 4. The Compax3F controller. Reprinted with permission.

The controller is configured through Parker Servo Manager software. The controller configuration includes the configuration of all devices in the system, as well as parameter setup of the control profile. Setup of the major configurations include:

1. Axis selection and configuration
2. Sensor configuration
3. Valve configuration
4. Machine zero/homing mode setup
5. Travel limit setting
6. IEC61131-3 variable list for programming

The configuration is saved in a configuration file and downloaded to the controller for system function. Once the configuration file is completed and downloaded correctly, the controller establishes communication channels with all of the input/output devices, and recognizes the type and parameter settings of these devices. This system includes the proportional direction control valve and the cylinder.

The controlling method is programmed in CODESYS, a programming environment for control systems that can be used to develop IEC61131-3 programs. Control programs can be programmed in various formats, including Instruction List (IL), Structured Text (ST), Sequential Function Chart (SFC), Function Block Diagram (FBD), Continuous Function Chart (CFC), and Ladder Diagram (LD). CODESYS has default functions that include bit manipulation, numeric function, type conversion, selection function, trigger, numerator, timer, and PID control functions (Hanssen, 2017). It provides a convenient program developing environment for controller programming. Figure 5 shows a function block program that was developed for position control. Major functions used in the program are jog function, power enable function, data conversion, motion reset function, absolute movement function, and set home function. The function block program illustrates the data flow and logic in executing the position control.

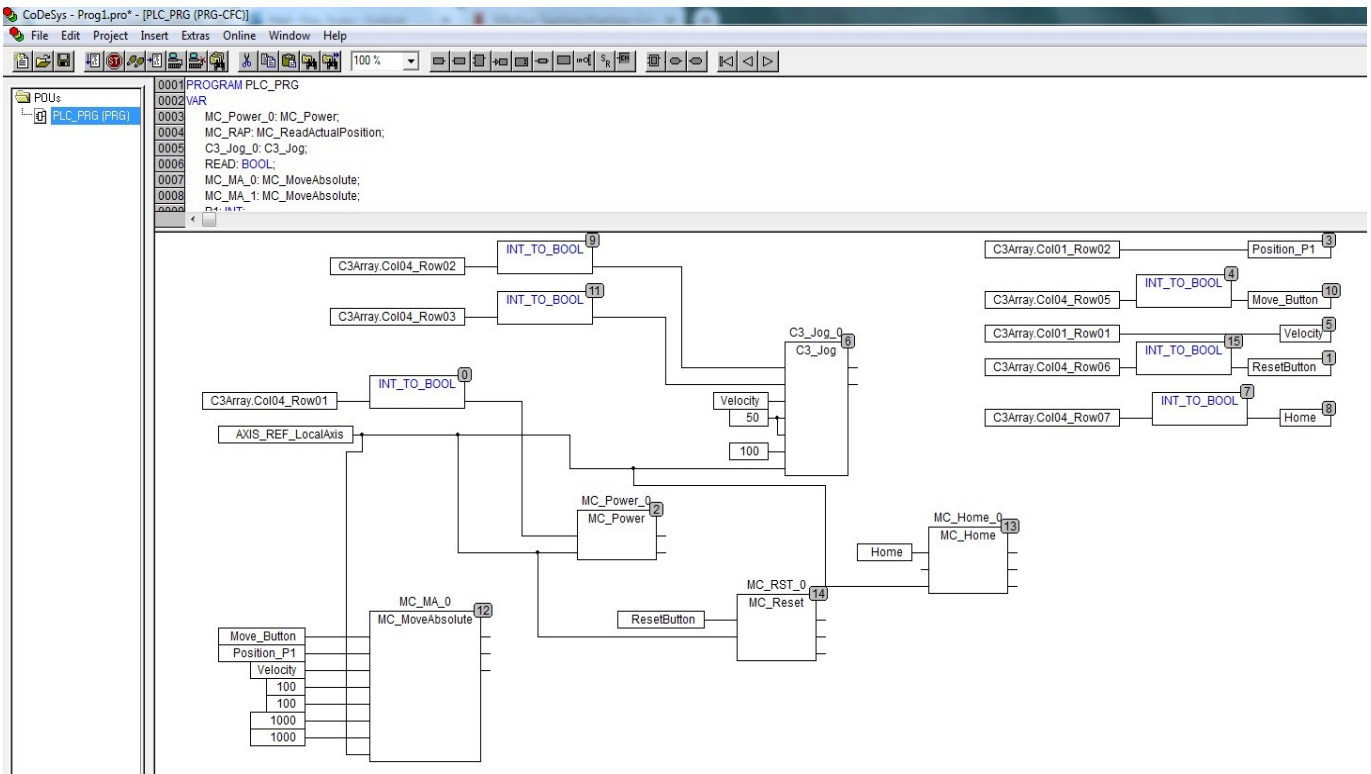


Figure 5. CODESYS programming.

The MC\_Power function was designed to control the on/off status of the drive/cylinder. Figure 6 shows the major inputs of this function—axis reference number of the cylinder and the Enable button from the HMI interface.

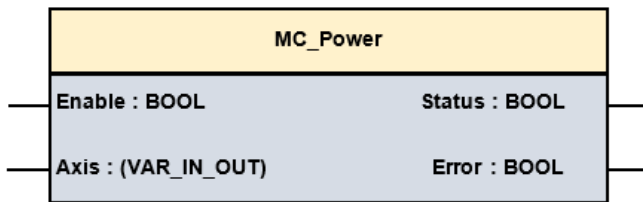


Figure 6. MC\_Power function.

The MC\_Home function was designed to execute a sequence for searching the home position and causing the axis to move to that position. Figure 7 shows the major inputs of this function—the axis reference number of the cylinder, Execute input to provide a valve starting the execution, and Position input to provide an absolute position value. The MC\_Reset function was designed to reset all internal axis-related errors, and does not affect the output of the functional block instances. Figure 8 shows the major inputs—the axis reference number and the Boolean signal that activates this function. The MC\_MoveAbsolute function was designed to move the axis to an absolute position and use the input values.

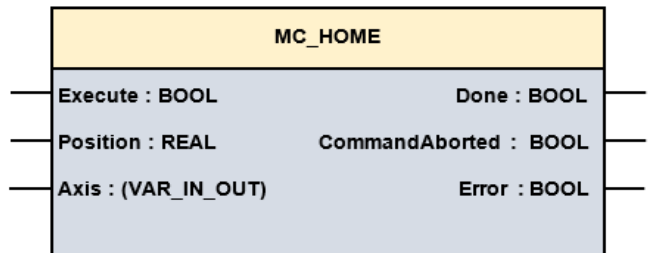


Figure 7. MC\_Home function.

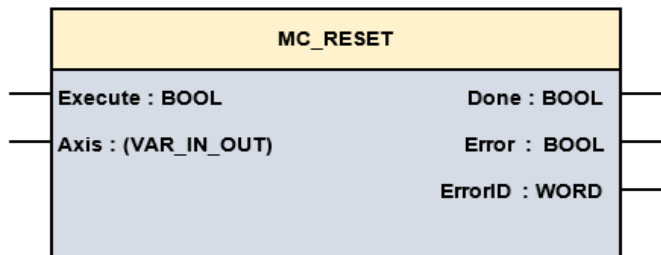


Figure 8. MC\_Reset function.

Figure 9 shows the inputs—the axis reference number, a Boolean signal to activate the function, and values to set target position, velocity, acceleration, deceleration, and jerk. The completed CODESYS program in CFC format is then

linked to the Compax 3F configuration file in the Parker Servo Manager environment. This combined project configuration and program file are then downloaded to the Compax 3F controller to implement the control function.

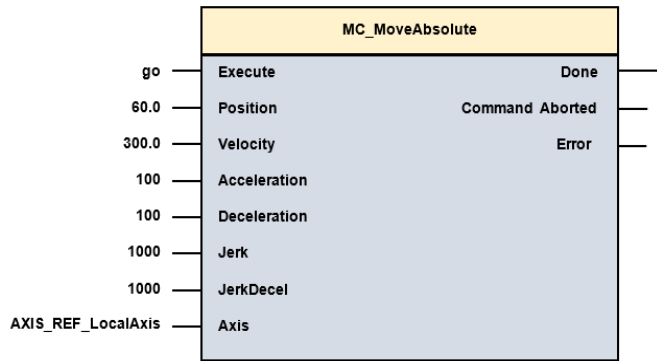


Figure 9. MC\_MoveAbsolute function.

## System HMI Interface

An HMI interface was developed to provide a control panel to the position control system. Figure 10 shows the layout of the control and that the interface is programmed in Interact Xpress software.

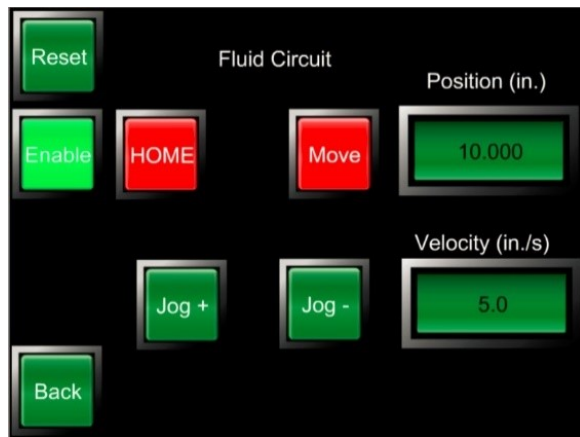


Figure 10. Position control panel.

The control panel contains seven buttons and two variable input boxes. The Enable and Reset buttons are Boolean buttons to enable the valve drive and reset the input variables for position and velocity controls, respectively. The Home button brings the cylinder piston to the pre-configured home position, and the Move button enables motion control, according to the input variables. Two Jog buttons (Jog+, Jog-) are used to allow manual jogging of the cylinder piston in both directions. There are variable input boxes to set position and velocity values for motion control. A Back button was included in order to navigate back to the previous window. Figures 11-13 show this position control system, and a

few more windows designed for instructions. Figure 11 shows the starting window of the motion control application. Users can select one of the control applications in order to proceed from fluid cylinder position control to motor position control.



Figure 11. Starting window.

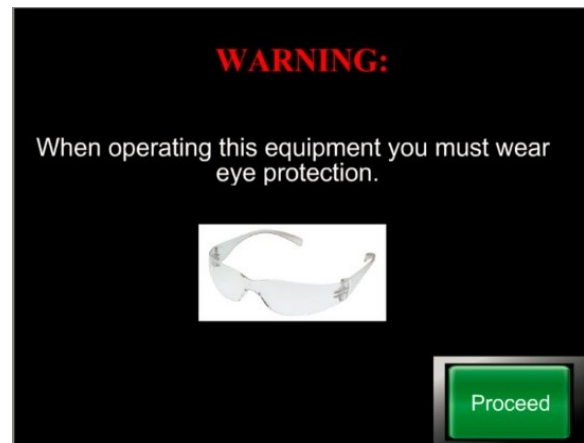


Figure 12. Instruction window (1).



Figure 13. Instruction window (2).

The interaction between this HMI interface and the application in the Parker Servo Manager software is based on data tags created in Interact Xpress and the connection between the data tags and variables used in the CODESYS program. Table 2 lists the data tags and their corresponding CODESYS variables.

Table 2. Data tags.

Function	Interact Express Tags	CODESYS Variables
Enable	C3.C.1904.1	C3Array.Col04_Row01
Home Button	C3.C.1904.7	C3Array.Col04_Row07
Jog Positive (+)	C3.C.1904.2	C3Array.Col04_Row02
Jog Negative (-)	C3.C.1904.3	C3Array.Col04_Row03
Velocity Input	C3.C.1901.1	C3Array.Col01_Row01
Position Input	C3.C.1901.2	C3Array.Col01_Row02
Move Button	C3.C.1904.5	C3Array.Col04_Row05
Reset Button	C3.C.1904.6	C3Array.Col04_Row06

## Performance Analysis

In a closed-loop position control system, system performance normally can be analyzed based on the step response time (rise time), the steady-state error, and the peak overshoot (Fundamentals of Motion Control, 2014). Due to limitations of time and equipment, the step response time was selected as the parameter to be collected and analyzed in this project. The step response time was defined as the time the system takes to respond to a step input signal from 10% to 90% of the steady state response. In this project, step response times were measured and analyzed in order to compare system performance at different P gain levels of the PID controller.

P gain is the proportional gain of the PID controller. Increasing the proportional gain increases the amount of current to the valve proportional to the amount of error the system produces. Therefore, the response time to the step signals should decrease. However, increasing the P gain further will cause the valve current to quadruple, which may result in oscillatory performance, and the valve could be damaged. In this project, the controller P gain was set to five different levels between 100 and 1000, and the step response times were measured and collected through an oscilloscope connected the valve, as shown in Figure 14. Table 3 shows the response time data collected at various P gain levels.

Figure 15 shows that the response times, measured at P = 1000, tended to be at the lowest levels. However, one measurement indicated an unusually high response time. This could have been caused by factors such as oscillatory performance, due to high P gains. Figure 16 shows a plot of the calculated averages of all measurements at the same P

gain levels. This figure also indicates that the system has the shortest response time when P gain is set to 800.

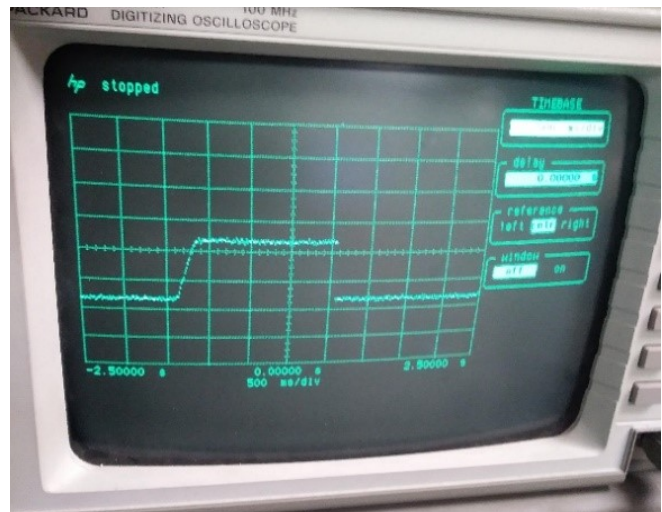


Figure 14. Data measurement.

Table 3. Data collected.

Response Time (ms)	P-100	P-200	P-500	P-800	P-1000
#1	275	250	250	225	350
#2	275	350	275	275	300
#3	275	375	300	225	225
#4	250	375	275	225	250
#5	275	400	325	225	250
Avg.	270	350	285	235	275

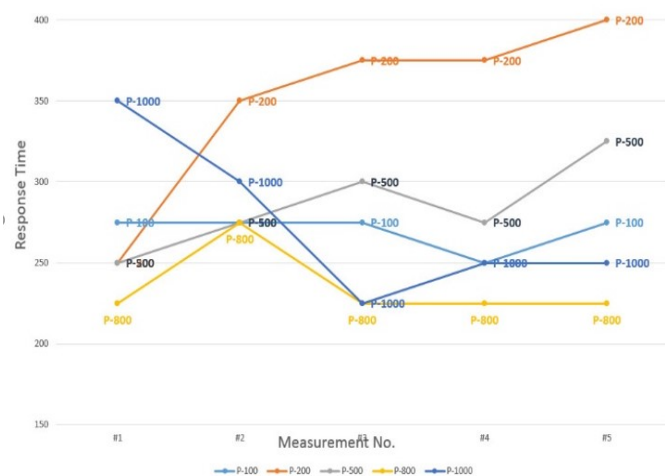


Figure 15. Line chart of the response times at different P gain levels.

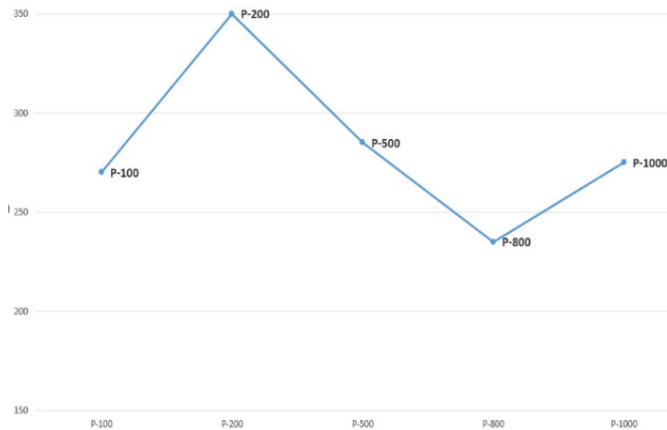


Figure 16. The average response times at different P gain levels.

## Conclusions

This automated electrohydraulic position control system was developed in order to introduce electro-hydraulics and control theory to students in the Manufacturing Engineering and Technology Program. This system provides students with experience in hardware configuration, programming, interfacing, and system integration. Due to time constraints, the step response times for position control at different P gain levels were measured and analyzed in this project. From the analysis, it was concluded that the optimized P gain value for the best system response time was P 800. Further studies will be conducted on I and D gains of the controller, as well as other performance characteristics, based on this established electro-hydraulic position control system.

## References

- Fundamentals of Motion Control. (2014). Retrieved from <http://www.ni.com/white-paper/3367/en/>
- Hanssen, D. (2017). Programmable logic controllers: a practical approach to IEC 61131-3 using CODESYS. Wiley.
- Parker Hannifin Corporation (2007). Electrohydraulic system engineering.

## Biographies

**YUQIU YOU** is an associate professor in the Engineering Technology and Management program at Ohio University. She earned her BE degree from HuaZhong University of Science and Technology in China, MS from Morehead State University of Morehead, and PhD in Technology Management (2006) from Indiana State University. Dr. You's interests include computer-integrated manufacturing, automation control, and remote control systems. Dr. You may be reached at [youy@ohio.edu](mailto:youy@ohio.edu)

**JESÚS PAGÁN** worked as a welding engineer for Newport News Shipbuilding, a robotic welding applications engineer for OTC Daihen-USA in Dayton, Ohio, and started his own company, Zeus Robotics, at the Innovation Center. He later joined the faculty at Ohio University, where he has worked for the Institute for Sustainable Energy and the Environment, the Center for Algal Engineering Research and Commercialization, and the Innovation Center as a field engineer for the NIST Hollings Manufacturing Extension Partnership (MEP). He is currently pursuing his doctorate in mechanical engineering. His research interests include robotics, energy, additive manufacturing, and welding automation. Mr. Pagan earned his MS and BS degrees in welding engineering from Ohio State University. Mr. Pagan may be reached at [paganj@ohio.edu](mailto:paganj@ohio.edu)

# ANALYSIS OF DUST EMISSION AND LIFE IMPACT ASSESSMENT OF FRAME-SHEAR WALL STRUCTURE

Yadong Bian, Zhongyuan University of Technology, China; Yanru Dai, Zhongyuan University of Technology, China; Li, Zhongyuan University of Technology, China; Zhicheng Gao, University of Akron; Jiliang Li, Purdue University Northwest

## Abstract

In this study, the authors performed dust-emission and life-impact assessments of frame-shear wall structure in Zhengzhou, China, by applying the Eco-indicator 99+ method and using SimaPro software. The results indicate that the dust emission of 1m<sup>2</sup> frame-shear wall structure is 35.22 kg, and dust emission in the dismantling phase accounts for 38.7% of the dust emission of the lifecycle of the building. The phase of operation and maintenance has obvious contributions to the environmental impacts of the lifecycle of the building. To reduce the construction dust emission and the environmental burden, some effective measures are proposed in this paper.

## Introduction

With the rapid development of urbanization, construction dust is continuously increasing, and the harm of haze has become increasingly severe. Although many factors can cause the haze, the influence of construction dust cannot be ignored, and has attracted wide attention. By establishing a dust emission mode, Li and Zheng (2020) analyzed dust emission in the construction phase, while Anand and Amor (2017) proposed a dust-emission coefficient in the preparation phase of construction. To achieve sustainable development, a lifecycle assessment (LCA) has been widely used to evaluate the environmental impacts of buildings (Hafliger et al., 2017; Hoxha, Habert, Lasvaux, Chevalier, & Le Roy, 2017; Vilches, Garcia-Martinez, & Sanchez-Montanes, 2017). However, study of building dust emissions is still in the primary stage of LCA application (Hossain, Poon, Lo, & Cheng, 2017; Najjar, Figueiredo, Palumbo, & Haddad, 2017). Cellura, Cusenza, and Longo (2018) applied the improved method to assess the environmental impacts on the Chinese city of Dalian and validated the effectiveness of the improved method. Araujo, Salvador, Piekarski, Sokulski, De Francisco, and Camarga (2019) analyzed the relative importance of lifecycle phases, especially focusing on the construction and production phases of materials, which made significant contributions to the buildings' environmental impacts. A conceptual framework was developed, which facilitated the assessment of carbon emissions over the lifecycle of the buildings' demolition (Hossain & Poon, 2018; Hussain, Malik, & Taylor, 2018; Kouchaki-Penchah, Sharifi, Mousazadeh, & Zarea-Hosseinabadi, 2016). Rosado, Vitale, Penteadó, and Arena (2017) provided an effective approach to collect data, and applied LCA to model building information.

Based on LCA, Hossain, Poon, Lo, and Cheng (2016) developed a quantitative lifecycle model for accounting for carbon emissions. A residential building in Sino-Singapore Tianjin Eco-city (Tianjin, China) was selected as a test case. Based on LCA, Vitale, Arena, Di Gregorio, and Arena (2017) quantitatively analyzed the dust emission and environmental impacts of all phases of the residential building; Hossain, Xuan, and Poon (2017) further proposed some effective measures for reducing dust emissions and environmental burden.

## Project Case

Frame-shear wall structure is a structural system formed by combining frame and shear wall together. The vertical load of the building is shared by the frame and the shear wall, while the horizontal load is mainly borne by the shear wall with high lateral stiffness. Frame-shear wall structure has not only the frame-structure characteristics of obtaining larger spaces and flexible arrangement, but also shear wall structural characteristics of higher stiffness and bearing capacity; thus, it is widely used in high-rise buildings. A frame-shear wall structure was chosen as a test case in the Chinese city of Zhengzhou. The height of the building was 20.75m. The total construction area was 2039.62m<sup>2</sup> and the design working life was 50 years. The building was constructed in 2015. Table 1 shows all of the building materials. SimaPro software (Hossain, Leu, & Poon, 2016) was used to quantify the dust emissions and environmental impact of frame-shear wall structure, and the lifecycle of the building was divided into four phases: materials production phase, construction phase, operation phase, and demolition phase. From this current study, the authors determined that the phase and the main factors have an obvious influence on maximum dust emissions and the environment. The functional unit studied was 1m<sup>2</sup> of net area over the 50 years reference study period of the building.

## Analysis of Lifecycle Inventory

*List of building materials for the production phase:* The list of materials consumed was selected from the construction company. Based on the 2008 quota of Henan Province, the depletion of building materials was considered. Table 1 shows the consumption of building materials. The input-output data of the functional unit was obtained from the relevant research results (Li & Zheng, 2020; Najjar et al., 2017; Rosado et al., 2017), while the unobtainable data refer to the database of SimaPro.

Table 1. Frame-shear wall structure residential building materials.

			Loss rate of transportation and other processes (%)	Actual consumption quantity
Commodity concrete	m <sup>3</sup>	1145.710	1.0	1156.623
Cement	t	119.930	1.5	121.729
Sand	m <sup>3</sup>	335.040	2.5	343.416
Steel	t	145.046	/	145.046
Aerated concrete block	m <sup>3</sup>	362.376	3.0	373.247

*List of materials for the construction, operation, and demolition phases:* Construction energy consumption includes energy consumption for transporting building materials and energy consumption for construction projects. According to the research of Zhu and Chen (2010), during the construction of the frame-shear wall structure, the transportation of material consumed about 1024.31 kg of diesel fuel. According to the list of engineering materials provided by the construction company, 1589.96 kg of diesel fuel, 983.28 kg of gasoline, and 22,739.47 kWh of electricity were used during the construction phase.

According to the facts related to energy consumption given by Tsinghua University's Building Energy Efficiency Research Center, a total of 970,815.415 kg of natural gas, 1,539,913.1 kWh of electricity, and 344,345.975 kg of coal were consumed during the design working life of the building. The National Statistical Yearbook proposed that the consumption of energy in the demolition phase was 90% of the energy consumption in the construction phase. It can be calculated that the demolition phase consumed 10,653.54 kg of diesel, 884.95 kg of gasoline, and 20,465.52 kW·h of electricity. According to the scope of evaluation limited in this study, the total dust emission was from the production stage of the building materials, construction stage, stage of operation and maintenance, and demolition stage. The total dust emission in the lifecycle of frame-shear wall structure can be determined using Equation 1:

$$W_d = \sum_{i=1}^4 W_i \quad (1)$$

where,  $W_d$  is the total dust emission during the lifecycle;  $W_i$  is the dust emission of the  $i$  phase for frame-shear wall structure; and,  $i$  is equal to 1, 2, 3, or 4, referring to the corresponding stages of production of building materials, construction, operation and maintenance, and demolition, respectively.

The dust emission from the production stage of building materials mainly comes from the process of exploiting raw materials, transportation of raw materials, and processing of the building materials. Production of building materials, including exploiting raw materials and processing building materials, causes not only dust emissions but also energy

consumption. Transportation of raw materials results in dust emissions caused by energy consumption. The dust emissions in this stage can be determined by Equation 2:

$$W_1 = \sum_{j=1}^n Q_j \times P_{d,j} + E_1 \times E_d \quad (2)$$

where,  $W_1$  is the total dust emission of frame-shear wall structure in this phase;  $Q_j$  is the quantity of building materials used,  $j$ ;  $P_{d,j}$  is the dust emission factor for the production process of the building materials,  $j$ ;  $E_1$  is the total energy consumption of frame-shear wall structure in this stage; and,  $E_d$  is the dust emission per unit of energy consumption.

In this construction stage, the dust mainly comes from the process of excavating the foundation, assembling the building materials, and the working process. As the excavating foundation lasts for only a short time, and this stage will take measures to decrease dust emission, so the dust emission is mainly from the energy consumption of the transportation process of the building materials. The calculation model of this phase is given by Equation 3:

$$W_2 = E_2 \times E_d \quad (3)$$

where,  $W_2$  is the dust emission in the production phase of the building materials, and  $E_2$  is the total energy consumption in this stage.

When calculating the dust emission in operation and maintenance stage, the dust emission in the process of maintenance is ignored, and the dust emission of the operation stage is taken into account. The total energy consumption of the operation process increases with the extension of the service life, and should be combined with the life span. The dust emission in the maintenance stage can be determined using Equation 4:

$$W_3 = U_d \times S \times Y \quad (4)$$

where,  $W_3$  is the dust emission in the stage of operation and maintenance;  $U_d$  is the dust emission factor in the construction process; and,  $Y$  is the operating life of the frame-shear wall structure.

The dust from this demolition and waste disposal stage is mainly caused by the energy consumption of the mechanical equipment, the energy consumption of transportation, the demolition of the building, and the transportation of the construction rubbish. Given the government's efforts to control the dust, the theoretical model ignores the construction dust caused by the scattering of transported construction waste. Therefore, the calculation model of dust emission in the demolition stage can be determined using Equation 5:

$$W_4 = D_d \times S + E_4 \times E_d \quad (5)$$

where,  $D_d$  is the dust emission factor when a frame-shear wall is dismantled and broken, and  $E_4$  is the energy consumption in the demolition phase.

SimaPro software was used to simulate dust emissions over the lifecycle of frame-shear wall construction and analyze the engineering cases. The basic data of SimaPro software is mainly based on the data of Holland and Europe, including the ecological indexes of hundreds of industrial raw materials, and has data from most industrial production processes. By simplifying the process of lifecycle environmental impact assessment, the SimaPro software presents quantitative data in the form of a network diagram and a tree diagram, and briefly introduces the tree diagram generated by the SimaPro software.

The tree diagram consists of boxes, lines with arrows, histograms, text, and values. The box indicates the process or product, the value above the box indicates the amount of the product, the value in the lower left corner of the box indicates the contribution of the process or product, and the dark-filled portion in the histogram on the right side of the box indicates the contribution. Lines with arrows connect a process with its immediate process, where the arrows point to the immediate process, the thickness of the lines indicates the contribution to the immediate process, and the thicker the lines, the greater the contribution to the immediate process, and vice versa. The working principle of SimaPro can be summarized as follows: the input-output material flow corresponding to each unit process can be established, the output result of the previous process can be used as the input flow of the subsequent process, and all related processes are connected to each other to form a complete process of material flow, energy consumption flow, and emission flow of a product.

By using SimaPro software, the construction dust emission of the frame-shear wall structure in the building materials production stage was calculated (see Figure 1). It can be seen that the emission of construction dust in this stage was about 24,849.391 kg, and that the dust emission in a 1m<sup>2</sup> building was about 12.183 kg. Construction dust in the building materials production phase mainly comes from commercial concrete, aerated concrete blocks, cement, and

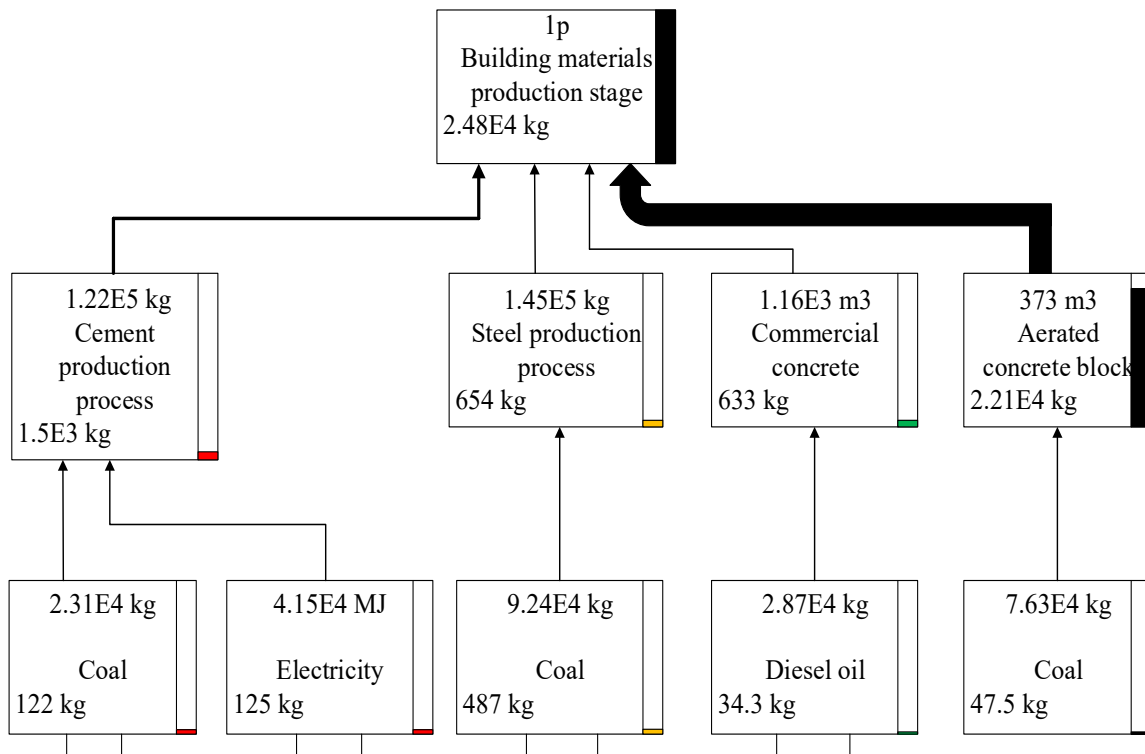


Figure 1. Analysis of dust emissions from building materials during the production stage.

steel. Among them, the production of aerated concrete blocks emitted the most construction dust—about 22,060 kg. The second is the construction dust emission of cement production, about 1501.19 kg; the construction dust emissions from the production of steel and commercial concrete were 654 kg and 633 kg, respectively.

The construction phase included the transportation and assembly processes of building materials. The material flow in the construction stage is mainly energy input and waste discharge. Correspondingly, the construction dust emission in this stage was mainly caused by energy consumption. According to Figure 2, the total construction dust emission of frame-shear wall structure simulated by SimaPro software was 263 kg during the construction phase, and, correspondingly, the construction dust emission of 1m<sup>2</sup> during the construction phase was about 0.129 kg. The transportation of building materials offered only a small contribution to the construction dust emission at the construction stage—only 12.3 kg. The building materials assembly process contributed greatly to construction dust emission at the construction stage, reaching 251 kg and accounting for 95.4% of the total. The building materials assembly process mainly consumed three kinds of energy sources: diesel, gasoline, and electricity. The construction dust emission in this process was mainly generated by electricity used in the building materials assembly process, with the dust emissions reaching 247 kg and accounting for 95.4% of the construction dust emission in the entire construction stage.

The period of operation and maintenance is the longest of all the stages in the lifecycle of the frame-shear wall structure. The total amount of construction dust emission at this stage changed with the change of operation and maintenance time, and there was a positive proportional relationship between them. From Figure 3, it can be concluded that the building dust emission analog quantity in the operation and maintenance phase was 18,948.447 kg, and, correspondingly, the building dust emission of 1m<sup>2</sup> in the operation and maintenance phase was about 9.29 kg. From the thickness of the arrowhead line in the tree diagram, it can be seen that the dust emission of each process in the operation and maintenance stage was: home appliances > lighting > air conditioning refrigeration > central heating > cooking, and its specific emission was about 7770 kg, 6770 kg, 2220 kg, 2150 kg, and 42.6 kg, respectively. Among them, electrical energy consumption was the main reason for the large dust emission in the three processes of household appliances, lighting, and air conditioning and refrigeration. Dust emission during central heating was mainly caused by coal consumption.

According to the analysis of the list of demolition and waste disposal stages, dust emission at this stage came from three processes: demolition and crushing, construction waste recycling, and waste landfill. At present, there are many ways to deal with construction waste: assuming that all steel is recycled, this involves the transportation of steel and final waste. Figure 4 shows construction dust emissions

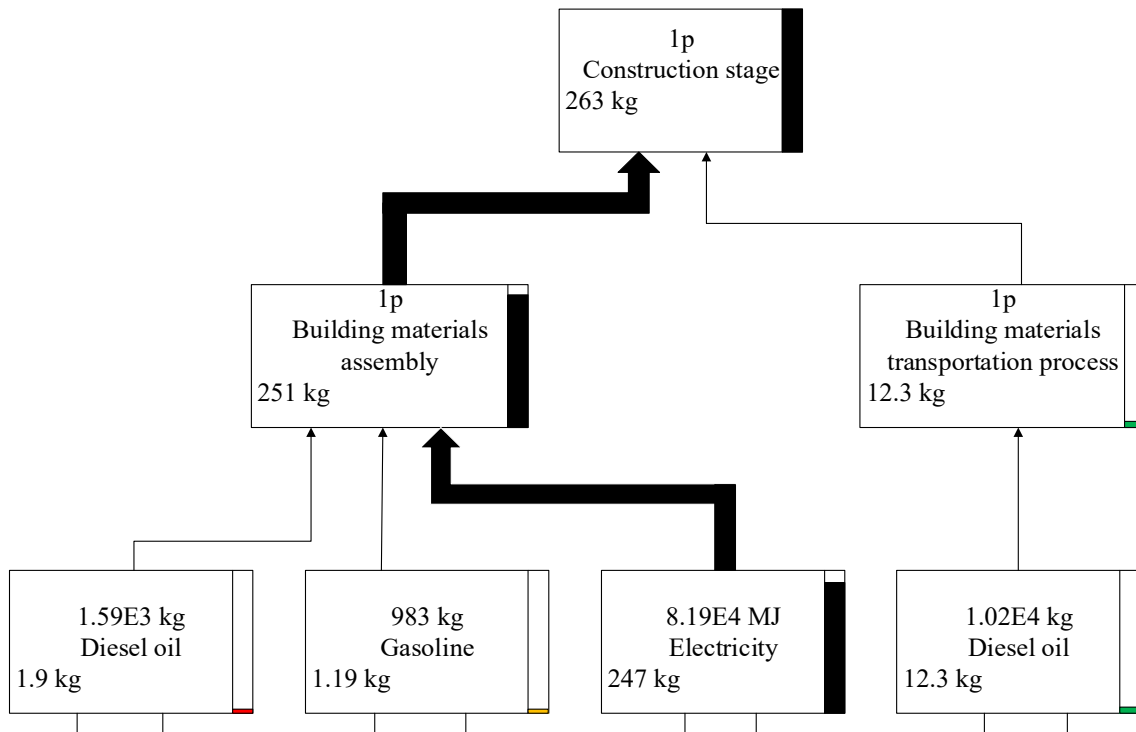


Figure 2. Analysis of dust emissions during the construction phase.

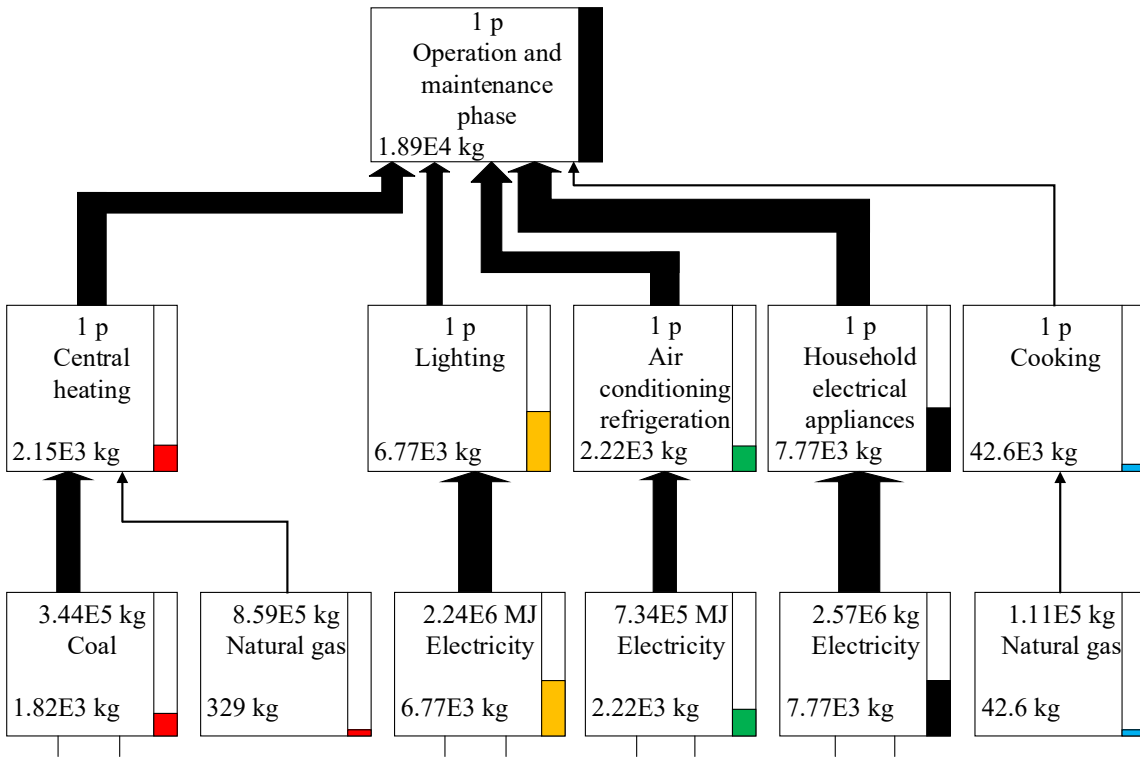


Figure 3. Analysis of dust emissions during the operation and maintenance stage.

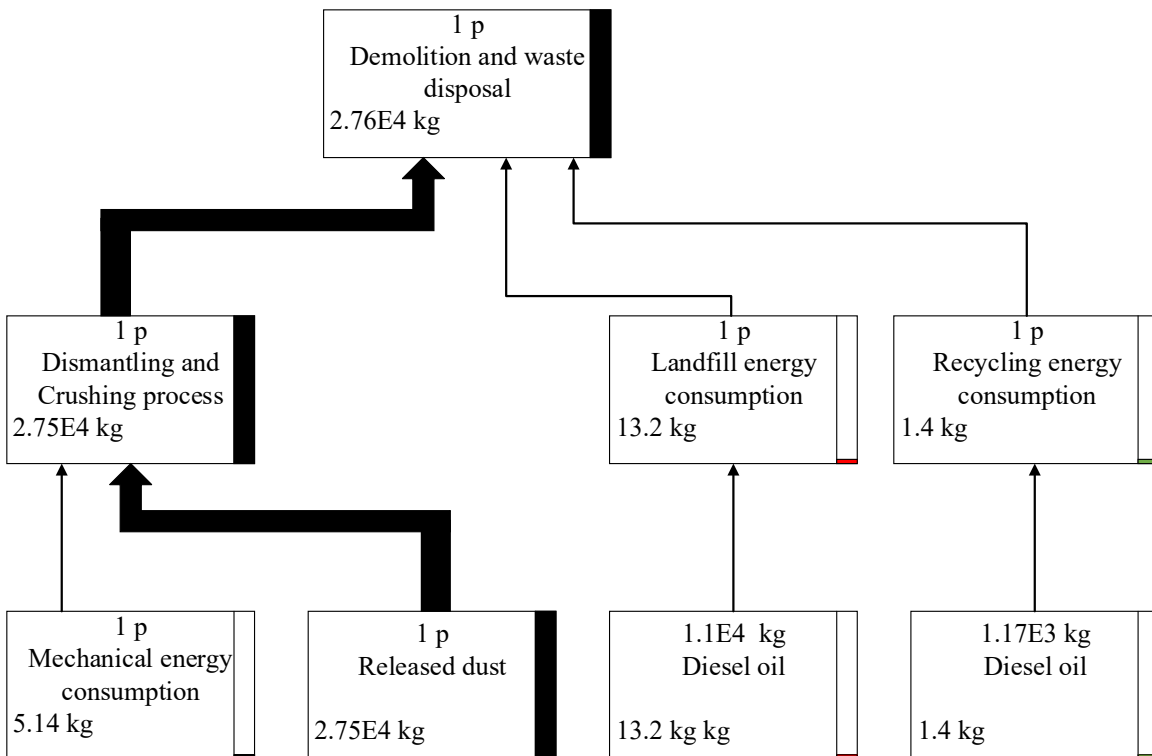


Figure 4. Analysis of dust emissions during the demolition and waste disposal stage.

of 27,553.605 kg in the demolition and waste disposal phase, and, correspondingly, the construction dust emission of 1m<sup>2</sup> in the demolition and waste disposal phase was about 13.51 kg. The emission of construction dust from demolition and crushing, landfill and recycling of building materials was 27,538.994 kg, 13.21 kg, and 1.397 kg, in order from highest to lowest. In the demolition and crushing process, the emission of construction dust from frame-shear wall structure was the highest, reaching 99.94%.

The construction dust emission of frame-shear wall structure was 71,614.289 kg (see Figure 5) over the entire lifecycle, and that of 1m<sup>2</sup> in the lifecycle was about 35.11 kg. Because there are many processes involved in the lifecycle and the graphics and text cannot be displayed clearly, the important nodes are displayed in SimaPro by decreasing the number of truncated nodes. From the figure, it can be seen that the construction dust emission during the entire lifecycle was from largest to smallest in the following order: demolition and waste disposal stage, building material production stage, operation and maintenance stage, and construction stage.

*Contribution of frame-shear wall structure to environmental categories:* The method of Eco-indicator99+ was used to obtain the characteristic values, or 1m<sup>2</sup> of net area of the building as the functional unit. Table 2 shows the six envi-

ronmental categories: inorganics, ecotoxicity, acidification, land use, mineral, and fossil fuels, and different phases of the characterization values. The contribution of inorganics, ecotoxicity, air acidification, and depletion of fossil fuel in the operation and maintenance phase reached 37.8%, 88.6%, 78.2%, and 87.4%, respectively. The production of material exhausts a lot of land and minerals.

*The environmental impact of frame-shear wall structure on the lifecycle assessment:* Three kinds of assessment values on human health, ecosystemic quality, and resources were simulated using SimaPro in the lifecycle of the building. Table 3 shows the results for the environmental impact sequences for the operation and maintenance phase, the building material production phase, the demolition and waste treatment phase, and the construction phase.

### Interpretation of Results

1. The dust emission of 1m<sup>2</sup> of net area of the building was 35.22 kg. The largest phase of dust emission was the dismantling phase in the lifecycle of buildings, which mainly comes from the dismantling and crushing process. Some effective measures should be carried out to reduce dust emissions, such as closing the construction site, covering the dust-screening cloth in time, and continuously sprinkling water.

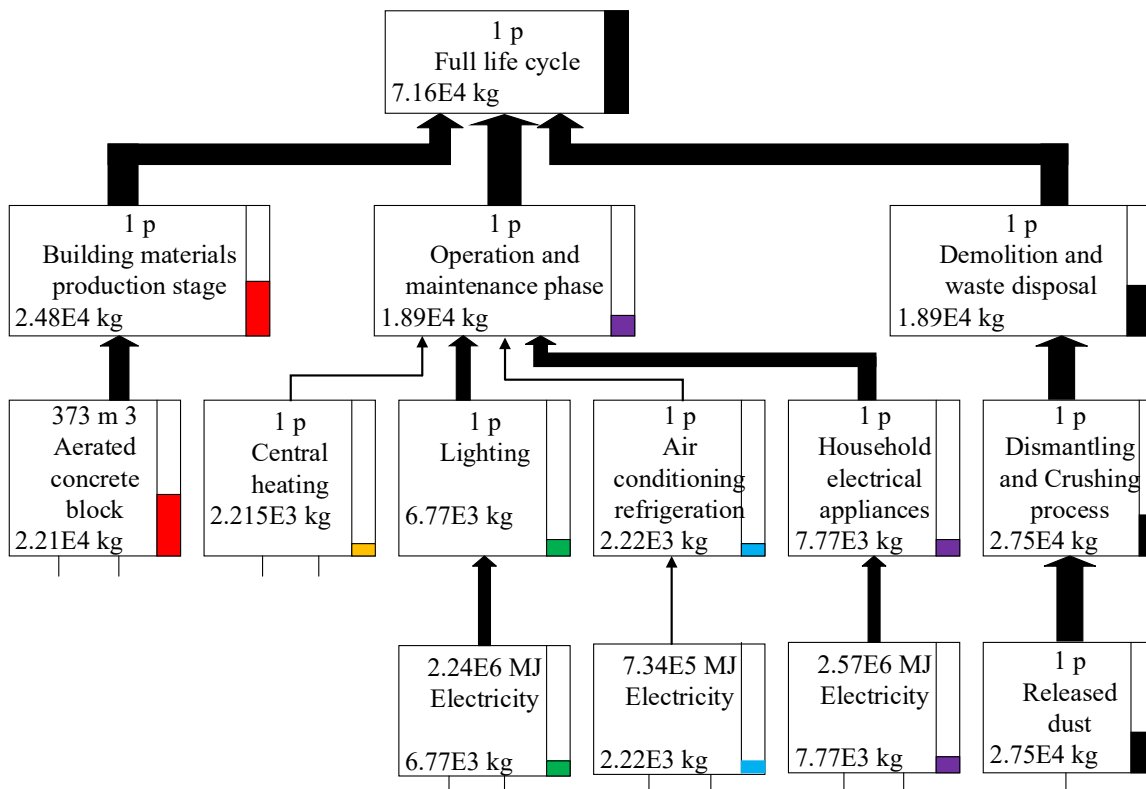


Figure 5. Analysis of dust emissions during the entire lifecycle.

Table 2. Environmental impact categories and characterization values.

Environmental categories	Lifecycle	Building material production phase	Construction phase	Operation and maintenance phase	Demolition phase
Respiratory inorganics (DALY)	4.87E-3	1.49E-3	2.64E-5	1.84E-3	1.51E-3
Ecotoxicity (PAF*m <sup>2</sup> yr)	1.14E+1	8.38E-1	2.19E-1	1.01E+1	1.97E-1
Acidification/Eutrophication (PDF*m <sup>2</sup> yr)	4.08E+1	7.99	4.75E-1	3.19E+1	4.27E-1
Land use (PDF*m <sup>2</sup> yr)	2.95E-3	1.97E-3	5.15E-4	0	4.62E-4
Minerals (MJ surplus)	1.29E+1	1.29E+1	1.71E-3	0	1.54E-3
Fossil fuels (MJ surplus)	3.41E+3	3.25E+2	5.74E+1	2.98E+3	5.20E+1

Table 3. Endpoint environmental impact category value.

Environmental categories	Lifecycle	Building material production phase	Construction phase	Operation and maintenance phase	Demolition phase
Human health (DALY)	5.25E-3	1.58E-3	3.03E-5	2.11E-3	1.51E-3
Ecosystem quality (PDF*m <sup>2</sup> yr)	4.20E+1	8.09	4.95E-1	3.29E+1	4.47E-1
Resources (MJ surplus)	3.42E+3	3.38E+2	5.74E+1	2.98E+3	5.20E+1

- The environmental impact follows the order in the lifecycle: the operation and maintenance phase, the building material production phase, the phase of demolition and waste disposal, and the construction phase. In addition, the phase of operation and maintenance has obvious influence on inorganics, ecotoxicity, acidification, and depletion of fossil fuel, given that natural gas, coal, and electricity are consumed during the two phases, thereby increasing the demand for fossil fuels. The use of fuel will emit gaseous pollutants, which aggravate environmental pollution. Land and mineral resources are seriously exhausted in the material production phase, which is caused by the consumption of raw materials (mineral resources) in this phase.

## Conclusions

In this study, the authors determined dust emissions for a 1m<sup>2</sup> building, which reached 35.22 kg during the lifecycle of the building, with the largest dust emission came during the dismantling phase and which accounted for 38.7% of the building's lifecycle. The environmental impact was largest during the phase of operation and maintenance. The research results can be used in the study of dust emissions of similar structures, but they do not apply to other structural forms. In the future, additional engineering cases and different building structures should be used and analyzed in order to improve the accuracy of the research results during the lifecycle of the given building.

## References

- Anand, C. K., & Amor, B. (2017). Recent developments, future challenges and new research directions in LCA of buildings: A critical review. *Renewable & Sustainable Energy Reviews*, 67, 408-416. doi: 10.1016/j.rser.2016.09.058
- Araujo, C. K. D., Salvador, R., Piekarski, C. M., Sokulski, C. C., de Francisco, A. C., & Camargo, S. (2019). Circular Economy Practices on Wood Panels: A Bibliographic Analysis. *Sustainability*, 11(4), 21. doi: 10.3390/su11041057
- Cellura, M., Cusenza, M. A., & Longo, S. (2018). Energy-related GHG emissions balances: IPCC versus LCA. *Science of the Total Environment*, 628-629, 1328-1339. doi: 10.1016/j.scitotenv.2018.02.145
- Hafliger, I. F., John, V., Passer, A., Lasvaux, S., Hoxha, E., Saade, M. R. M., & Habert, G. (2017). Buildings environmental impacts' sensitivity related to LCA modeling choices of construction materials. *Journal of Cleaner Production*, 156, 805-816. doi: 10.1016/j.jclepro.2017.04.052
- Hossain, M. U., Leu, S. Y., & Poon, C. S. (2016). Sustainability analysis of pelletized bio-fuel derived from recycled wood product wastes in Hong Kong. *Journal of Cleaner Production*, 113, 400-410. doi: 10.1016/j.jclepro.2015.11.069
- Hossain, M. U., & Poon, C. S. (2018). Comparative LCA of wood waste management strategies generated from

- building construction activities. *Journal of Cleaner Production*, 177, 387-397. doi: 10.1016/j.jclepro.2017.12.233
- Hossain, M. U., Poon, C. S., Lo, I. M. C., & Cheng, J. C. P. (2016). Comparative environmental evaluation of aggregate production from recycled waste materials and virgin sources by LCA. *Resources Conservation and Recycling*, 109, 67-77. doi: 10.1016/j.resconrec.2016.02.009
- Hossain, M. U., Poon, C. S., Lo, I. M. C., & Cheng, J. C. P. (2017). Comparative LCA on using waste materials in the cement industry: A Hong Kong case study. *Resources Conservation and Recycling*, 120, 199-208. doi: 10.1016/j.resconrec.2016.12.012
- Hossain, M. U., Xuan, D. X., & Poon, C. S. (2017). Sustainable management and utilisation of concrete slurry waste: A case study in Hong Kong. *Waste Management*, 61, 397-404. doi: 10.1016/j.wasman.2017.01.038
- Hoxha, E., Habert, G., Lasvaux, S., Chevalier, J., & Le Roy, R. (2017). Influence of construction material uncertainties on residential building LCA reliability. *Journal of Cleaner Production*, 144, 33-47. doi: 10.1016/j.jclepro.2016.12.068
- Hussain, M., Malik, R. N., & Taylor, A. (2018). Environmental profile analysis of particleboard production: a study in a Pakistani technological condition. *International Journal of Lifecycle Assessment*, 23(8), 1542-1561. doi: 10.1007/s11367-017-1385-9
- Kouchaki-Penchah, H., Sharifi, M., Mousazadeh, H., & Zarea-Hosseini, H. (2016). Lifecycle assessment of medium-density fiberboard manufacturing process in Islamic Republic of Iran. *Journal of Cleaner Production*, 112, 351-358. doi: 10.1016/j.jclepro.2015.07.049
- Li, X. J., & Zheng, Y. D. (2020). Using LCA to research carbon footprint for precast concrete piles during the building construction stage: A China study. *Journal of Cleaner Production*, 245, 15. doi: 10.1016/j.jclepro.2019.118754
- Najjar, M., Figueiredo, K., Palumbo, M., & Haddad, A. (2017). Integration of BIM and LCA: Evaluating the environmental impacts of building materials at an early stage of designing a typical office building. *Journal of Building Engineering*, 14, 115-126. doi: 10.1016/j.jobe.2017.10.005
- Rosado, L. P., Vitale, P., Pentead, C. S. G., & Arena, U. (2017). Lifecycle assessment of natural and mixed recycled aggregate production in Brazil. *Journal of Cleaner Production*, 151, 634-642. doi: 10.1016/j.jclepro.2017.03.068
- Vilches, A., Garcia-Martinez, A., & Sanchez-Montanes, B. (2017). Lifecycle assessment (LCA) of building refurbishment: A literature review. *Energy and Buildings*, 135, 286-301. doi: 10.1016/j.enbuild.2016.11.042
- Vitale, P., Arena, N., Di Gregorio, F., & Arena, U. (2017). Lifecycle assessment of the end-of-life phase of a residential building. *Waste Management*, 60, 311-321. doi: 10.1016/j.wasman.2016.10.002
- Zhu, Y., & Chen, Y. (2010). Study on Lifecycle Energy Consumption and Environmental Emissions of Residential Buildings. *Journal of Tsinghua University (Science and Technology)* (3), 330-334.

## Biographies

**YADONG BIAN** is a professor at Zhongyuan University of Technology. He earned his doctoral and master's degrees in geotechnical engineering from the China University of Mining and Technology in 2005 and 2002, respectively. Dr. Bian's research interests include lifecycle assessment of buildings, slope engineering and retaining structure, and rock blasting technology. Dr. Bian may be reached at [mob-coco@sina.com](mailto:mob-coco@sina.com)

**YANRU DAI** earned her master's and bachelor's degrees in structural engineering and civil engineering from Zhongyuan University of Technology in 2017 and 2014, respectively. Her research interests include lifecycle assessment of buildings. Ms. Dai may be reached at [1162073194@qq.com](mailto:1162073194@qq.com)

**LI LI** is a student in the master's degree program at Zhongyuan University of Technology, majoring in geotechnical engineering. Mr. Li may be reached at [lili1993abc@163.com](mailto:lili1993abc@163.com)

**ZHICHENG GAO** is working at the University of Akron at the Auburn Science and Engineering Center. Mr. Gao may be reached at [gzcmark@gmail.com](mailto:gzcmark@gmail.com) or [zg8@zips.uakron.edu](mailto:zg8@zips.uakron.edu)

**JILIANG LI** is an Assistant Professor of Civil/Geotechnical Engineering in the Department of Mechanical and Civil Engineering, School of Engineering, College of Engineering and Sciences, at Purdue University Northwest. Dr. Li may be reached at [Lil919@purdue.edu](mailto:Lil919@purdue.edu) or [Lil919@pnw.edu](mailto:Lil919@pnw.edu)

# A ROBOT FOR WELD QUALITY INSPECTION

Vu Duong, Duy Tan University, Vietnam; Ashfaq Ahmed, Purdue University Northwest; Dang Ngoc Sy, Duy Tan University, Vietnam

## Abstract

Currently, detection of defects by non-destructive testing (NDT) is commonly applied throughout the shipyard, marine construction, refinery, and petroleum storage industries. However, also at present, quality inspection is mainly implemented manually. This is an expensive, wasteful, and dangerous operation, especially in a hostile industrial environment. In this paper, the authors propose an efficient, low-cost ultrasonic system utilizing a robot. The robot can climb alongside the metal surface, freely and automatically moving against welding seams and identifying weld defects, in interaction with the operator. The robot can also climb up, down, and along a ship's hull by means of a special tracking mechanism. The robot can also "see" its surroundings using a seam-tracking algorithm. The use of a robot reduces the risk of accidents and makes the system more reliable. Additionally, the interface between the ultrasonic transducer and robot monitoring system is flexible and easier to implement in a maritime setting. Results of engineering studies and practical implementation met desirable expectations. The system was expected to exceed the existing human threshold of weld quality inspection, resulting in savings of both labor and material costs.

## Introduction

Welding is one of the most widely used hot-work processes in the manufacturing and construction industries. In the shipbuilding industry, welding is commonly used to fabricate metal structures up to several meters in length and weighing up to several thousand tons. The complexity of construction projects is increasing rapidly, including offshore platforms, floating production storage, fuel storage tanks, boilers in thermal power plants, and nuclear power plants. Current inspection methodologies require a great deal of human effort along with expensive and specialized equipment (ISO 17640, 2017; Sirois, Crepeau, & Eddyfi, 2016; Tariq, 2015). Besides, most field-weld inspections are done manually by human inspectors with visual inspection for defect detection. Manual inspection is error-prone, due to the human factor, and time consuming. Human inspection exposes the inspector to unsafe and dangerous environmental conditions such as underwater and radioactive conditions. The robotic system proposed here is desirable for guaranteeing inspection consistency with a high degree of confidence (Jaise, Dinakaran, Ramya, & Harris Samuel, 2018; Hung, Tran, Nhan, Quang, & Anh, 2016; Nhan, Hung, Quang, Sy, Anh, & Quang, 2016).

The robotic-based NDT service as proposed is a niche growth area that is applicable to many sectors of industry. The gas and oil industry, refineries, and the petroleum dis-

tribution network are viable markets for adopting the automatic inspection of welding connections using the robot. The engineering design of the robot for automatic inspection of welding connections makes not only scientific but practical sense. Recent publications in the area of weld quality inspection and seam tracking only deal with climbing robots utilizing a single-axis encoder, moving alongside the specific trajectory, namely tube-welding seams where the inspector cannot mark the location of defects (in real time). A robot with a 3D encoder carrying an advanced ultrasonic detector can climb alongside a welding seam, for example a ship hull, to collect data for assessment, which would significantly improve inspection reliability as well as enhance inspector safety, as they would be protected from unsafe working conditions. With the 3D mapping of welding lines, this unique robot facilitates the storage of inspection data and document tracking in the lifecycle of the ship. Moreover, the robot can transmit data wirelessly to remote PC stations.

In this paper, the authors briefly describe the design and fabrication process, followed by development of the prototype robot. The robot was enabled and integrated with an NDT transducer for welding inspection of a ship's hull. The robot moved alongside the welding line and placed a mark to locate the defect, with a speed of about 0.3 km/h. The system was fed by battery power lasting at least four hours. The robot transmitted acquired data to the base station via Ethernet connectivity. Total system weight (including NDT sensor) was no more than 8.0 kg.

## Design Methodology

The robot had four wheels with magnetic pieces adhered to the metal surface and was free to move during inspection. The body of the robot contained the sensors for tracking and guiding the robot along the welding line (real trajectory). The transducer for NDT inspection was installed along the base of the robot. The robotic arm could be freely adjusted according to the contour of the surface (flat or curved). The distance between the two arms was also adjustable to fit the size (width) of the welding line. Figure 1 shows a conceptual design of the robot. The main body of the robot was made up of aluminum alloy to decrease its weight and extend the durability for harsh coastal environments. Figure 2 shows how the adhesion of magnets depends on the gap between magnet pieces and metallic surface (Magnets vs. Steel - K&J Magnetics) and the nature of magnet material (permanent magnets made of rare earth elements).

Figure 3 shows that the adhesion force is maximum when the gap is zero. One important parameter to consider is the optimal adhesion force. If this force is too high, it affects the

maneuverability of the robot. On the other hand, if this force is too low, the robot would not firmly adhere to the surface. Therefore, the dynamic and static forces need to be calculated so that designers can reach the optimal choice for the magnet pieces and motor drive.

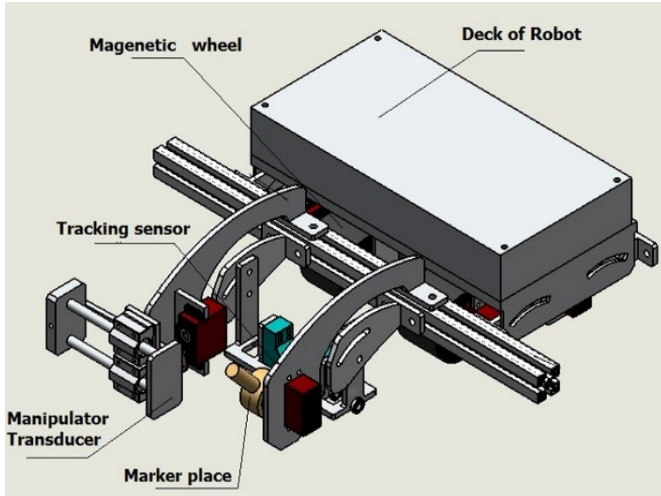


Figure 1. Conceptual design of the robot.



Figure 2. Magnet piece.

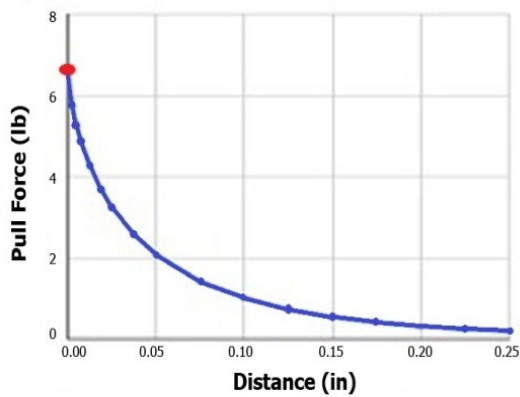
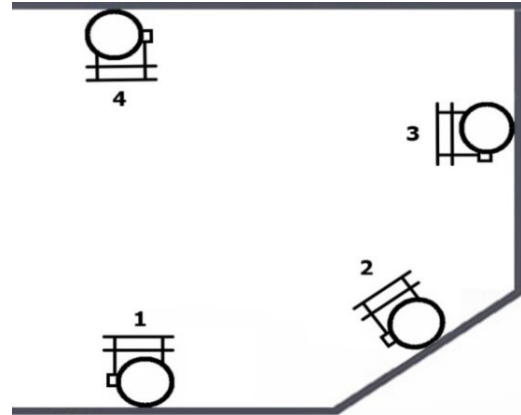


Figure 3. Adhesion force of magnet piece.

In field conditions (namely in a shipyard), when the robot is climbing on a metallic surface, it must firmly adhere to the surface in all welding positions, including the one on the ceiling, as shown by position 4 in Figure 4.

Figure 4. All positions of the robot in space.



## Dynamic Calculations

Figure 5 depicts a schematic of the system for a robot with weight  $W$  located on an inclined surface with an angle of inclination  $\theta$  (Ronney, 2016).

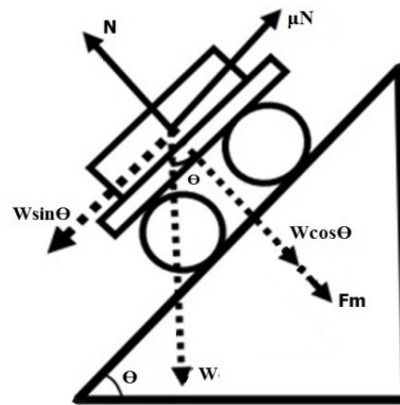


Figure 5. Free body diagram of the robot moving on an inclined surface.

Equations 1-3, from static equilibrium are:

$$\sum f_y = W \cos \theta + F_m - N = 0; \quad N = W \cos \theta + F_m \quad (1)$$

$$\sum f_x = W \sin \theta - \mu N \quad \text{or} \quad N = \frac{W \sin \theta}{\mu} \quad (2)$$

$$W \cos \theta + F_m = \frac{W \sin \theta}{\mu} \quad (3)$$

where,

- W = weight of the robot
- $\Theta$  = angle of inclination
- $F_m$  = magnetic adhesion force
- d = distance of center of gravity from the climbing surface
- L = distance between the front and rear wheels
- R/4 = reaction from surface on each wheel
- $\mu$  = coefficient of friction of wheels
- N = total reaction from surface on the robot

From Equation 3,  $F_m$  is the magnetic adhesion force for the robot to avoid slipping and is given by Equation 4:

$$F_m > \frac{W \sin \theta}{\mu} - W \cos \theta \quad (4)$$

Figure 6 illustrates the system for the special case when the robot is moving on a vertical surface ( $\theta = 90^\circ$ ). To avoid sliding or slipping, the magnetic adhesion force, as given by Equation 5, should be greater than  $W/\mu$ .

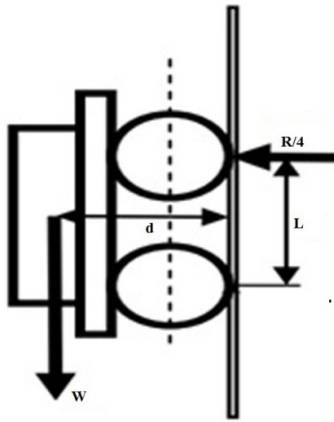


Figure 6. Schematic of the robot moving on a vertical surface.

$$F_m \geq \frac{W}{\mu} \quad (5)$$

To avoid turnover, the adhesion force should be satisfied according to Equation 6:

$$F_m \geq \frac{(W \cdot d)}{2 \cdot L} \quad (6)$$

This means that the center of gravity of the robot should be as close to the surface as possible, and the distance between the wheels should be large. Equation 7 defines the overall stability for the robot to avoid sliding and turnover.

$$F_m \geq \left( \frac{W}{\mu} \right) + \left( W \cdot \frac{d}{2L} \right) \quad (7)$$

From the dynamic calculation using the Equations 1-7, the minimum adhesion force should be 59 Newton (N) on each wheel, with a total force on four wheels to be 236 N. For a loading capacity of 8 kg, including NDT device, the motor drive (Motor guide – REV Robotics, 2017) must at least provide a torque moment of 2.28 Nm. Airtronics DS8911HV ultra torque motor with a torque moment of 3.32 Nm was chosen.

## Control Scheme of Robot

Microchip/Atmel's ATmega328, 8-bit AVR microcontroller was selected for controlling all aspects of the robot. The ATmega328 is a popular microcontroller with a processing speed up to 20 MHz. The robot was operated using 12 VDC power supply. This power was distributed directly to the NDT device as well as the controller module driving the robot. The isolation block helped to separate the power supply and the controlling circuit in order to avoid interference. The microcontroller received input signals from the NDT device, tracking sensor, driving motor, marking device, and zigzag manipulation device. Figure 7 shows the control scheme for the microcontroller and how it receives a signal from the line sensor in order to regulate the wheel on tracking the welding line exactly.

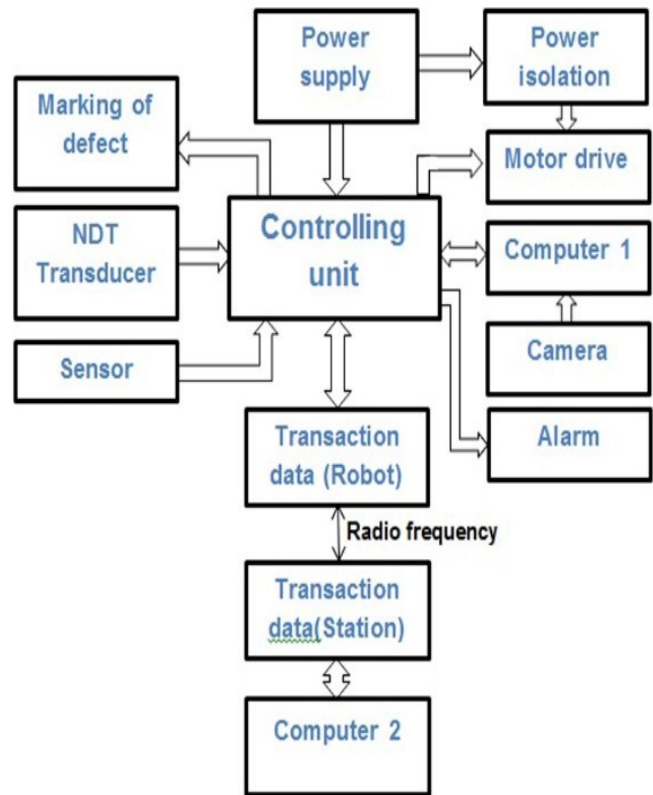


Figure 7. Monitoring and control scheme block diagram.

Figure 8 shows how the ATmega328 also receives the signals and processes all the signals from peripheral devices. Monitor (Inspector) interacts with the robot via the controller, using an RF mode for interaction. The servo motor connections were standard, power (Vcc lead), ground (GND lead), and the signal lead (SIGNAL). The servo could run with an input voltage in the range of 3.5-8.4V. The signal lead was connected to one of the PWM outputs of the ATmega328 in order to control the angle of the driver. Figure 9 shows the robot control system block diagram. The micro-controller was used as the control center of the robot and received control signals from the central station and sensors and, along with intelligent algorithms, would control the wheels and pin point the location of the defect.

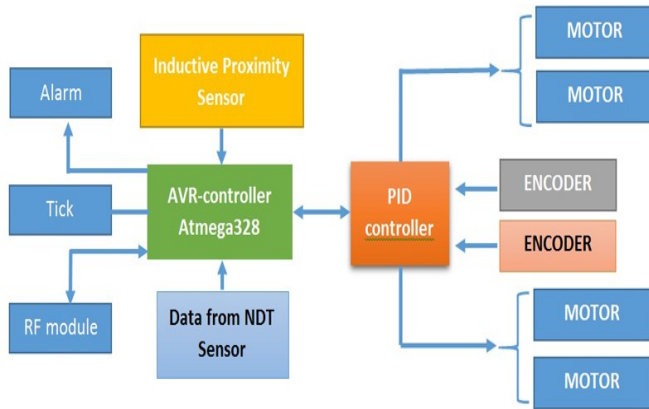


Figure 9. The robot control system block diagram.

The algorithm allowing the robot to follow the welding line is summarized as follows:

$V_R$  and  $V_L$  are the speed that is set for the right and left wheel motors;  $V$  is the initial speed of the robot; and,  $V_{change}$  is the speed of change when the robot goes off the welding line. The quantities  $SS\_right$  and  $SS\_left$  are the values returned from two inductive proximity sensors. An analytical formula used to calculate the velocities for the right and left wheels is given by Equations 8 and 9, respectively.

$$V_R = V - V_{change} \cdot SS\_right \quad (8)$$

$$V_L = V - V_{change} \cdot SS\_left \quad (9)$$

In order for the robot to follow the welding line, it had to identify the weld lines. Using the protruding characteristics of the welding line compared to the basic metal surface as shown in Figure 10, two inductive proximity sensors located on both sides of the welding line were used to identify the moving path of the robot compared to the welding line.

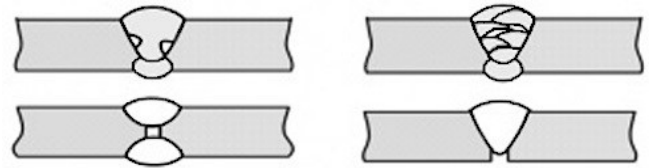


Figure 10. Cross section of some weld lines.

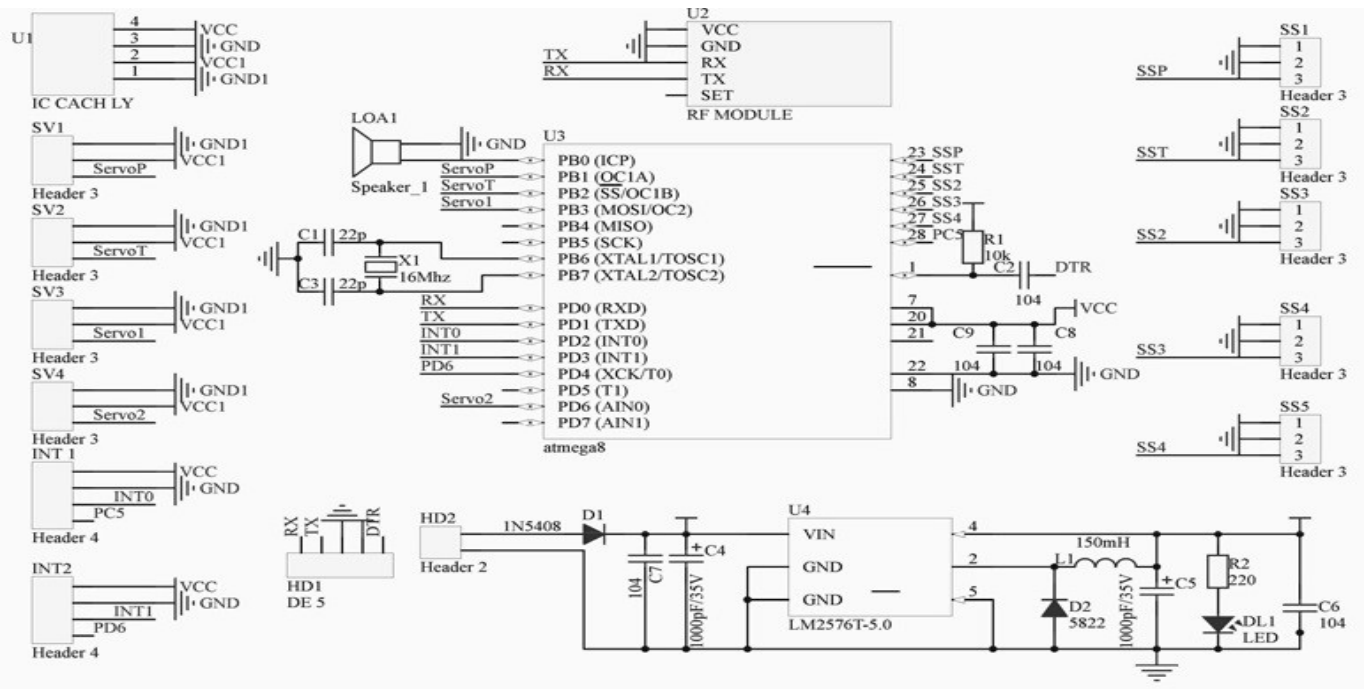


Figure 8. Circuit for controlling all blocks of the robot.

## Results

Figure 11 shows how the prototype robot could move on steel surfaces with a decline from 0° to 180°. The robot was regulated by tracking along the welding line automatically. The manipulation (zigzag) simulates the manual movement of the inspector on site. The robot can mark (mechanically) the place of the defect (using paint). Interaction with the NDT device was incorporated into the design, but needs further improvement.



Figure 11. Prototype robot.

The performance and capability of the robot were thoroughly investigated in a test environment at the shipyard in Da Nang, Vietnam. Table 1 lists the various tests conducted on the prototype by the research team.

Table 1. Results of test in the Song Thu shipyard.

Inclination (°)	Quantity of test	Adhesive (%)	Tracking (%)
0	50	100	100
30	50	100	100
<b>60</b>	50	90	100
<b>90</b>	50	90	100
<b>120</b>	50	90	100
150	50	100	100
180	50	100	100

As indicated in Table 1, for an inclination angle in the range of 60°-120°, a small amount of sliding occurred. In general, as a first step of this project, the robot operated according to targeted specifications. The prototype satisfied all general requirements for automatic NDT inspection but, again, in some cases there was a small amount of sliding, due to friction and wear characteristics of the material. Another reason may be attributed to the inadequate capacity of the motor.

## Future Research

The system represents an important contribution to the reliable inspection of weld quality. Work on improvement in terms of stability, 3D mapping, and onsite testing for industrial applications is the aim of continuing research. Based on successful implementation of this project, it is expected to extend the development and application to other industries, such as petroleum distribution network, power plants, and aerospace. Another application under consideration is the custom development of new systems and utilizing drone technology with the specific aim of monitoring and mapping of robots. For example, simultaneous operation of multiple robots, each being assigned a specific task, namely separating traffic or system for plane Geodesy.

## Acknowledgments

The authors very strongly would like to express their indebtedness to the dedication and commitment of the faculty, staff, and students of the Center of Electrical and Electronic Engineering (CEE) at Duy Tan University for their collaboration and contribution to the ultimate success of the project.

## References

- Hung, M. L., Tran, H. D., Nhan, H. P., Quang, P. H., & Anh, Q. P. (2016). Automated robotic Monitoring and Inspection of Steel Structure and Bridges. *Robotica*, 37 (5), 947-967.
- International Organization for Standardization (ISO). (2017). *Non-destructive testing of welds- Ultrasonic testing- Techniques, testing levels, and assessment* ISO 17640: 2017. Retrieved from <http://www.iso.org/standard/69611.html>
- Jaise, J., Dinakaran, D., Ramya, M. M., & Harris Samuel, D. G. (2018). A Survey on Magnetic Wall-Climbing Robots for Inspection. *International Journal of Mechanical and Production Engineering Research and Development*, 8(6), 59-68. DOI: 10.24247/ijmperdec20186
- Magnets vs. Steel - K&J Magnetics. (n.d.). Retrieved from <http://www.kjmagnetics.com/blog.asp?p=magnets-vs-steel>
- Motor guide – REV Robotics. (2017). Retrieved from [www.revrobotics.com/content/docs/MotorGuide.pdf](http://www.revrobotics.com/content/docs/MotorGuide.pdf)
- Nhan, H. P., Hung, M. L., Quang, P. H., Sy, N. D., Anh, H. V., & Quang, H. D. (2016). Visual and 3D Mapping for Steel Bridge Inspection using a Climbing Robot. *33<sup>rd</sup> International Symposium on Automation and Robotics in Construction (ISARC)*. DOI:10.22260/ISARC2016/0018. University of North Carolina at Chapel Hill.
- Ronney, P. D. (2016). *Basics of mechanical engineering*. University of Southern California. Retrieved from [PFD.Drive-pdfd.com/basics-of-mechanical-engineering-prof-paul-d-ronney-e16452684.html](http://PFD.Drive-pdfd.com/basics-of-mechanical-engineering-prof-paul-d-ronney-e16452684.html)

- 
- Sirois, M., Crepeau, J., & Eddyfi, R. A. (2016). Detection and depth sizing of stress corrosion cracking in pipelines using tangential eddy current array. *55th Annual Conference of The British Institute of Non-Destructive Testing (NDT 2016)*, Nottingham, UK. Curran Associates, Inc. ISBN: 978-1-5108-3094-3.
- Tariq, S. (2015). Automation of Non-Destructive Testing. *School of Engineering, Cambridge CB21 6AL, LSBU Research Open*. Retrieved from <http://researchopen.lsbu.ac.uk/1596/1/SATTAR%20BUE%20keynote.pdf>

## Biographies

**VU DUONG** received his PhD in Mechanics from Saint Petersburg University, Russia, in 1993. He is currently the Director for the Center of Electrical Engineering (CEE) at Duy Tan University and a Professor of Electronics and Telecommunication. He was formerly the dean of the vocational school at Duy Tan University. His research interests include welding technology, mechatronics and entrepreneurship, and professional starter education. Dr. Duong may be reached at [duongvuaustralia@gmail.com](mailto:duongvuaustralia@gmail.com)

**ASHFAQ AHMED** is a Professor of Electrical and Computer Engineering Technology at Purdue University Northwest. Ahmed received his bachelor's of science degree in electrical engineering from the University of Karachi in 1973 and master's of applied science degree in 1978 from the University of Waterloo. He is the author of a textbook on power electronics, published by Prentice-Hall. He is a registered professional engineer in the state of Indiana. He is a senior member of IEEE. Ahmed's research interests include embedded system design, electric vehicles, and VHDL design. Professor Ahmed may be reached at [aahmed@pnw.edu](mailto:aahmed@pnw.edu)

**DANG NGOC SY** received his BS degree in electronics and telecommunication from Duy Tan University, Vietnam, in 2009 and MS degree in computer science from Duy Tan University in 2012. He is the Vice Director for the Center of Electrical Engineering (CEE) at Duy Tan University. His research interests include robotics, design automation of embedded systems, and mechatronics design. He joined the CDIO program as a lecturer in 2013. Mr. Sy may be reached at [sydn.mcs@gmail.com](mailto:sydn.mcs@gmail.com)

# INSTRUCTIONS FOR AUTHORS: MANUSCRIPT FORMATTING REQUIREMENTS

The INTERNATIONAL JOURNAL OF ENGINEERING RESEARCH AND INNOVATION is an online/print publication designed for Engineering, Engineering Technology, and Industrial Technology professionals. All submissions to this journal, submission of manuscripts, peer-reviews of submitted documents, requested editing changes, notification of acceptance or rejection, and final publication of accepted manuscripts will be handled electronically. The only exception is the submission of separate high-quality image files that are too large to send electronically.

All manuscript submissions must be prepared in Microsoft Word (.doc or .docx) and contain all figures, images and/or pictures embedded where you want them and appropriately captioned. Also included here is a summary of the formatting instructions. You should, however, review the [sample Word document](http://ijeri.org/formatting-guidelines) on our website (<http://ijeri.org/formatting-guidelines>) for details on how to correctly format your manuscript. The editorial staff reserves the right to edit and reformat any submitted document in order to meet publication standards of the journal.

The references included in the References section of your manuscript must follow APA-formatting guidelines. In order to help you, the sample Word document also includes numerous examples of how to format a variety of scenarios. Keep in mind that an incorrectly formatted manuscript will be returned to you, a delay that may cause it (if accepted) to be moved to a subsequent issue of the journal.

1. **Word Document Page Setup:** Two columns with ¼" spacing between columns; top of page = ¾"; bottom of page = 1" (from the top of the footer to bottom of page); left margin = ¾"; right margin = ¾".
2. **Paper Title:** Centered at the top of the first page with a 22-point Times New Roman (Bold), small-caps font.
3. **Page Breaks:** Do not use page breaks.
4. **Figures, Tables, and Equations:** All figures, tables, and equations must be placed immediately after the first paragraph in which they are introduced. And, each must be introduced. For example: "Figure 1 shows the operation of supercapacitors." "The speed of light can be determined using Equation 4:"

5. **More on Tables and Figures:** Center table captions above each table; center figure captions below each figure. Use 9-point Times New Roman (TNR) font. Italicize the words for table and figure, as well as their respective numbers; the remaining information in the caption is not italicized and followed by a period—e.g., "*Table 1*. Number of research universities in the state." or "*Figure 5*. Cross-sectional aerial map of the forested area."
6. **Figures with Multiple Images:** If any given figure includes multiple images, do NOT group them; they must be placed individually and have individual minor captions using, "(a)" "(b)" etc. Again, use 9-point TNR.
7. **Equations:** Each equation must be numbered, placed in numerical order within the document, and introduced—as noted in item #4.
8. **Tables, Graphs, and Flowcharts:** All tables, graphs, and flowcharts must be created directly in Word; tables must be enclosed on all sides. The use of color and/or highlighting is acceptable and encouraged, if it provides clarity for the reader.
9. **Textboxes:** Do not use text boxes anywhere in the document. For example, table/figure captions must be regular text and not attached in any way to their tables or images.
10. **Body Fonts:** Use 10-point TNR for body text throughout (1/8" paragraph indentation); indent all new paragraphs as per the images shown below; do not use tabs anywhere in the document; 9-point TNR for author names/affiliations under the paper title; 16-point TNR for major section titles; 14-point TNR for minor section titles.



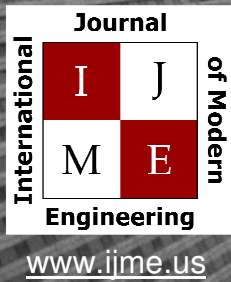
11. **Personal Pronouns:** Do not use personal pronouns (e.g., "we" "our" etc.).
12. **Section Numbering:** Do not use section numbering of any kind.
13. **Headers and Footers:** Do not use either.

14. **References in the Abstract:** Do NOT include any references in the Abstract.
  15. **In-Text Referencing:** For the first occurrence of a given reference, list all authors—last names only—up to seven (7); if more than seven, use “et al.” after the seventh author. For a second citation of the same reference—assuming that it has three or more authors—add “et al.” after the third author. Again, see the *sample Word document* and the *formatting guide for references* for specifics.
  16. **More on In-Text References:** If you include a reference on any table, figure, or equation that was not created or originally published by one or more authors on your manuscript, you may not republish it without the expressed, written consent of the publishing author(s). The same holds true for name-brand products.
  17. **End-of-Document References Section:** List all references in alphabetical order using the last name of the first author—last name first, followed by a comma and the author’s initials. Do not use retrieval dates for websites.
  18. **Author Biographies:** Include biographies and current email addresses for each author at the end of the document.
  19. **Page Limit:** Manuscripts should not be more than 15 pages (single-spaced, 2-column format, 10-point TNR font).
  20. **Page Numbering:** Do not use page numbers.
  21. **Publication Charges:** Manuscripts accepted for publication are subject to mandatory publication charges.
  22. **Copyright Agreement:** A copyright transfer agreement form must be signed by all authors on a given manuscript and submitted by the corresponding author before that manuscript will be published. Two versions of the form will be sent with your manuscript’s acceptance email.
23. **Submissions:** All manuscripts and required files and forms must be submitted electronically to Dr. Philip D. Weinsier, manuscript editor, at [philipw@bgsu.edu](mailto:philipw@bgsu.edu).
  24. **Published Deadlines:** Manuscripts may be submitted at any time during the year, irrespective of published deadlines, and the editor will automatically have your manuscript reviewed for the next-available issue of the journal. Published deadlines are intended as “target” dates for submitting new manuscripts as well as revised documents. Assuming that all other submission conditions have been met, and that there is space available in the associated issue, your manuscript will be published in that issue if the submission process—including payment of publication fees—has been completed by the posted deadline for that issue.

Missing a deadline generally only means that your manuscript may be held for a subsequent issue of the journal. However, conditions exist under which a given manuscript may be rejected. Always check with the editor to be sure. Also, if you do not complete the submission process (including all required revisions) within 12 months of the original submission of your manuscript, your manuscript may be rejected or it may have to begin the entire review process anew.

Only one form is required. Do not submit both forms!

The form named “paper” must be hand-signed by each author. The other form, “electronic,” does not require hand signatures and may be filled out by the corresponding author, as long as he/she receives written permission from all authors to have him/her sign on their behalf.



Print ISSN: 2157-8052  
Online ISSN: 1930-6628



## INTERNATIONAL JOURNAL OF MODERN ENGINEERING

### ABOUT IJME:

- IJME was established in 2000 and is the first and official flagship journal of the International Association of Journal and Conferences (IAJC).
- IJME is a high-quality, independent journal steered by a distinguished board of directors and supported by an international review board representing many well-known universities, colleges and corporations in the U.S. and abroad.
- IJME has an impact factor of **3.00**, placing it among the top 100 engineering journals worldwide, and is the #1 visited engineering journal website (according to the National Science Digital Library).

### OTHER IAJC JOURNALS:

- The International Journal of Engineering Research and Innovation (IJERI)  
For more information visit [www.ijeri.org](http://www.ijeri.org)
- The Technology Interface International Journal (TIIJ).  
For more information visit [www.tiij.org](http://www.tiij.org)

### IJME SUBMISSIONS:

- Manuscripts should be sent electronically to the manuscript editor, Dr. Philip Weinsier, at [philipw@bgsu.edu](mailto:philipw@bgsu.edu).

For submission guidelines visit  
[www.ijme.us/submissions](http://www.ijme.us/submissions)

### TO JOIN THE REVIEW BOARD:

- Contact the chair of the International Review Board, Dr. Philip Weinsier, at [philipw@bgsu.edu](mailto:philipw@bgsu.edu).

For more information visit  
[www.ijme.us/ijme\\_editorial.htm](http://www.ijme.us/ijme_editorial.htm)

### INDEXING ORGANIZATIONS:

- IJME is indexed by numerous agencies.  
For a complete listing, please visit us at [www.ijme.us](http://www.ijme.us).

### Contact us:

**Mark Rajai, Ph.D.**

Editor-in-Chief  
California State University-Northridge  
College of Engineering and Computer Science  
Room: JD 4510  
Northridge, CA 91330  
Office: (818) 677-5003  
Email: [mrajai@csun.edu](mailto:mrajai@csun.edu)



[www.tiij.org](http://www.tiij.org)



[www.ijeri.org](http://www.ijeri.org)

The International Journal of Engineering Research & Innovation (IJERI) is the second official journal of the International Association of Journals and Conferences (IAJC). IJERI is a highly-selective, peer-reviewed print journal which publishes top-level work from all areas of engineering research, innovation and entrepreneurship.



## **IJERI Contact Information**

General questions or inquiries about sponsorship of the journal should be directed to:

Mark Rajai, Ph.D.

Founder and Editor-In-Chief

Office: (818) 677-5003

Email: [editor@ijeri.org](mailto:editor@ijeri.org)

Department of Manufacturing Systems Engineering & Management

California State University-Northridge

18111 Nordhoff St.

Room: JD3317

Northridge, CA 91330